POLITECNICO DI MILANO

Master of Science in Telecommunication Engineering
Department of Electronics, Information and Bioengineering

Controlled Source Electromagnetic (CSEM) & EM Migration

Supervisor
Associate Professor Giancarlo Bernasconi

Dissertation by
Oktay Burak Ertaş, 815696

Academic Year 2015-2016

Abstract

Geophysical exploration methods focus on different physical aspects of medium, and as one of them, controlled source electromagnetic (CSEM) exploits resistivity variations. Besides being a future-promising technique, CSEM is still regarded as immature in terms of interpretation of data and imaging. On the other hand, in literature, many CSEM alternative concepts have been proposed, which intrinsically indicates that there is no strict standards for this method yet.

This dissertation concentrates on several marine exploration environment scenarios, which differ in fundamental physical properties as sea depth, target depth, target resistivity for classical CSEM applications and alternative CSEM concepts, for instance, where receivers are towed by the vessel as well. Relatedly, qualitative and quantitative references and findings have been given for a comprehensive approach of sensing performance. Moreover, suggestions are made if necessary.

Furthermore, thesis also concerns imaging the prospect. It is well known that as a standard imaging technique, "*inversion*" is widely adopted in literature. However, in this work, "*Em migration*", which is simply converted from seismic into electromagnetics, has been under study. Em migration is relatively a more recent imaging method and draws attention since it requires several order of magnitude less time than inversion does.

In this dissertation, both sensitivity performance regarding varying physical parameters and correspondingly imaging via electromagnetic migration, are concerned for artificial and real datasets. Cases are studied under spoiling effects and finally a new imaging condition for electromagnetic migration is suggested and compared to the conventional one.

List of Tables

List of Figures

Introduction

Geophysical prospecting methods exhibit large variety with respect to physical aspects they are assigned to exploit. Seismic techniques, which have been regarded as the most common, takes the advantege of acoustic wave propagation through material and provide the greatest resolution of crust. However, as far as HC exploration is concerned, seismic is far from ensuring direct evidence. On the other hand, in this case, other methods like gravity and geochemical may provide more direct evidence of hydrocarbon presence, however with great localization uncertainty. This fact, obviously, suggests a multi-disciplinary approach between methods for maximum efficiency. Indeed, as another geophysical prospecting concept, electrical probing methods, when imaging techniques are considered, promise less structural resolution, however provide direct evidence of resistivity anomalies, which have intrinsically been given as one of the profound indicators of hydrocarbon filled structures, thus regarded as a complementary.

This study mainly concerns controlled source electromagnetic, which is an electrical method. It is aimed to define the technique and reveal its relations with others and give basic insights of imaging as far as a relativly new method "EM migration" is implemented.

Formation of thesis, thus planned as followingly:

- **Chapter 1** concerns various prospecting methods, their relationships with each other, strengths and weaknesses and defines CSEM method.

- **Chapter 2** provides theoretical background which is necessary for comprehending whole electromagnetic prospecting process,

- **Chapter 3** gives insights on CSEM in terms of physical parameters that define the system and provides related sensing limits. Data used in this chapter is gathered by using a 1 D simulator.

- **Chapter 4** introduces migration concept as an imaging concept and applies it into CSEM concept. This chapter also suggests a new imaging condition and provide comparisonal results for artificial data.

- **Chapter 5** represents a combination and implementation of concepts given in chapter 3 and chapter 4 into a model defined by a real dataset.

Chapter 1

Geophysical Surveying Techniques

Although the main focus of this work will be related to controlled source electromagnetic method, other main geophysical surveying techniques are brielfy given, since CSEM interpretations in some cases is inspired from a fraction of them [26]. In addition, CSEM is commonly stated [7], [17] as a complementary method to other techniques, rather than being unique self-sustained concept.

1.1 Non electrical surveying techniques

1.1.1 Seismic

In principle, seismic methods benefit propagation of vibration through matter. To get an image representation of subterranean structures, soundwaves generated by a source should propagate into the earth, and reflect off the edges of layers that it consists of. The source of vibration depends on where the survey is conducted. For terrestrial work, explosives that ensure a minimum phase signal [29] are widely used. Beside, as seen in figure 1.1

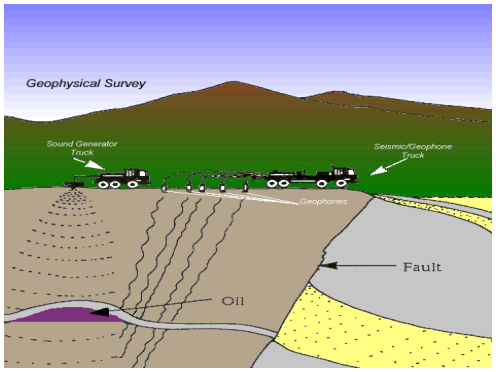

FIGURE 1.1: *A typical seismic survey where vibrating trucks are used as sources*

(taken from http://dnr.louisiana.gov/)

vibrator trucks are also used whose chirp fashioned continuous signal which needs to get deconvoluted [22] in the processing. These seismic signals are then collected by geophones.

In an off shore environment, however, hydrophones as receivers, are dedicated to collect propagated vibrational energy released by dynamites or usually giant bubbles of compressed air as depicted in figure 1.2.

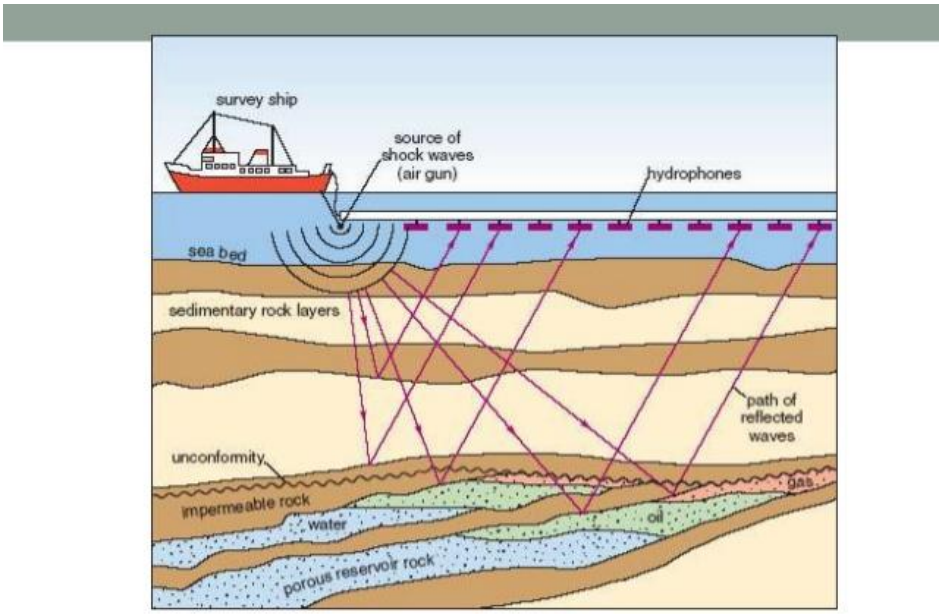

FIGURE 1.2: *Marine seismic survey with airgun source concept employed*

(taken from capefarewell.com)

For instance, as a seismic survey, basic idea of reflection seismic method is solving an inverse problem: by knowing the travel time of transmitted aqoustic signal and wave velocity, estimating the path it followed is achievable. Eventually, seismic surveys give information about layers' structure map in vertical section of crust as shown in figure 1.3. Here, by interpretation possible hydrocarbon traps can be detected. However, to be bolder to state that a valuable hydrocarbon reservoir is encountered, further inspections should be done, as resistivity investigation for example, which is the main focus and motivation of CSEM.

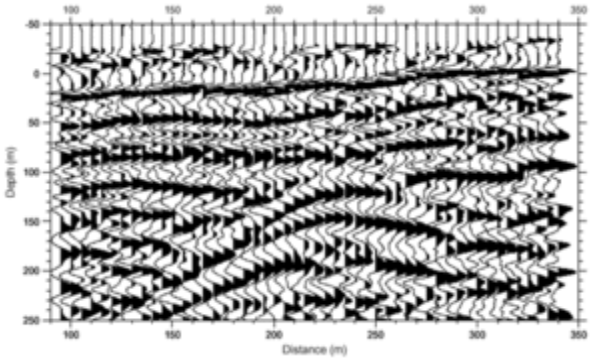

FIGURE 1.3: *A typical cross section of earth given by a seismic survey* [22]

Another commonly adopted seismic technique is known as *"migration"*, which directly inspires the evaluation of electromagnetic data in chapter 4. Detail and principles will be recovered in related chapter.

1.1.2 Geochemical

Geochemical prospecting aims to locate geochemical anomalies occur in the vicinity of an ore. In the case of subterraneal hydrocarbon presence, it is commonly probable that gases seep through stratas upward as indicated in figure 1.4. This causes a halo shape hydrocarbon gas concentration like methane, ethane, above the reservoir, in contrast with surrounding environment. Moreover, pyrite and carbonate precipitation have also been reported [30].

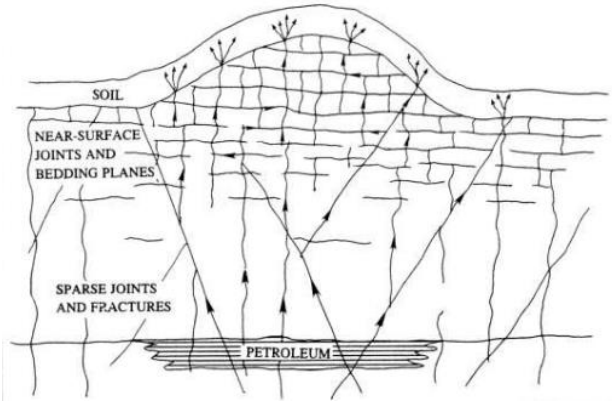

FIGURE 1.4: *A cross section of earth for geochemical surveying* [30]

A geochemical anomaly detection potentially presents a very convenient CSEM surveying site.

1.1.3 Gravity

Gravitometer is a device measuring gravitational fields. To be more specific this kind of instruments are basicly accelerometers that can detect changes in gravitational acceleration up to 10^{-6} m/s^2, which is 9.81 m/s^2 in average for our planet earth. A typical working principle is given in figure 1.5.

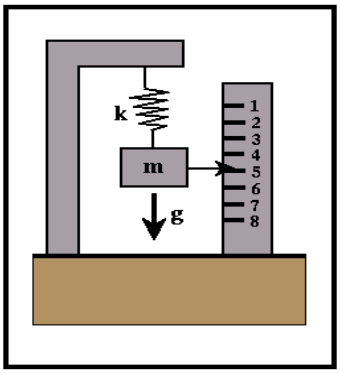

FIGURE 1.5: *An accelerometer design*

(taken from http://dnr.louisiana.gov/)

Basic idea here is to determine gravitational anomalies through earth's surface to utilize the fact that oil and gas bearing rocks have lower density compared to water bearing ones. In this case, accelerometers actually deviate when they are dragged above gravity anomalies as shown in figure 1.6.

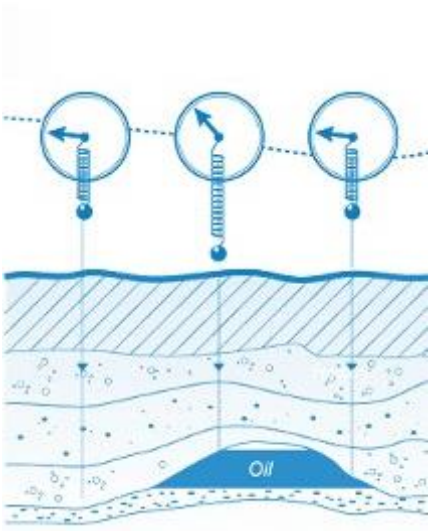

FIGURE 1.6: *Detection pinciple of an underground anomaly by gravity surveying method*

(taken from http://www.gazprominfo.com/)

However, that method has a crucial drawback. Considering the fact that since the gravitometer measures accelerational anomalies caused by masses technically, the same gravitational behaviour can be exhibited by various underlying structures that may differ in volume, density and even in shape as indicated in figure 1.7. This fact makes the technique vulnerable and creates nonuniqueness. However, gravity surveys are useful confirming results given by seismic and electrical methods. To clarify a region in terms of distributedness of target, where gravity anomalies are reported to exist, CSEM surveys would finely be complementary.

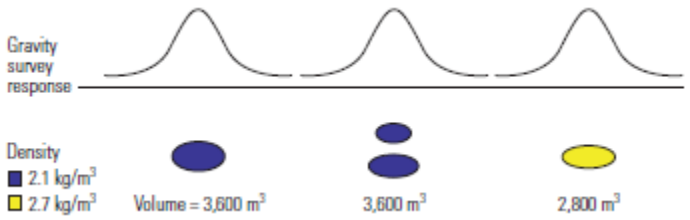

FIGURE 1.7: *Detection uncertainty by gravitometer* [30]

1.2 Electrical surveying techniques

Surveys which prinicpally utilize electrical and electromagnetic concepts, fundemantelly intend to get resistivity values of underground structure, inwich the prospect has been tought to be present. For that purpose, a general scheme should be comprised of transmitter and receiver instruments and signals to be conveyed. These can be seen as either time-domain systems which analyse the signal in time domain, or frequency-domain systems which might basicaly exploit one or more frequencies [31]. Moreover, electrical or electromagnetic surveys may be called active, that requires human intervention to nature by power consumption, or passive which uses natural signals created by the earth itself. An active electromagnetic survey can be exemplified by CSEM, while, magnetotelluric method is a good example to passive surveys.

1.2.1 DC Resistivity

In this method, electric current close to zero frequency is given through the earth via array of electrodes in conventional terrestrial environment. Given the spherical half space of diffusional nature of penetrated current, resultant voltages are measured the same way, using an array of receiver electrodes initially introduced by Schlumberger brothers. Since the current flows through paths under the crust, given current and voltage values directly lead the surveyor to resistivity behavior of structure underground.

The reach of survey is definitely subject to the power applied and the dimensions of the geometry of the whole transmission system. Besides, a general assumption for the efficient

depth, which could be reached using this method, is roughly given as 50% of transmitter-receiver distance. For terrestrial applications, best practical range is given as 1-50m [32]. This method is given place here, because CSEM is conceptually derived from it, in principle.

As far as off shore adaptation of this surveying technique is concerned, several works are present in the literature that issue investigations of small or large scale variations of sub-seabed resistivity. For further interest, systems developed, Francis (1977) and Becker (1985) can be reviewed.

1.2.2 Magnetometric Resistivity

Magnetometric resistivity method aims to interpret the subterranean structure by using the low frequency magnetic fields horizontally measured in two orthogonal directions close to a long electrode which is grounded [33]. Magnetometric resistivity is developed for terrestrial applications. However, it has been shown to be adapted to off shore as well. In such a scheme, the method is called The Magnetometric Off-Shore Electric Sounding (MOSES) [34]. In this scenario, the electrode which rises from the seabed upward is run by a commutated current. This creates a simple circuit that closes through seawater and sub-seabed structures. As a result, horizontal magnetic field gathered on seabed in the vicinity of the electrode, depends of the crust of earth [17]. Since the current strictly depends on the resistivity, that scheme allows sub-seabed resistivities to be revealed. However, the one who conducts such a survey must remind that it is shown that a horizontally layered crust does not create magnetometric resistivity anomalies [33].

1.2.3 Magnetotelluric (MT)

Since it is first noticed in 1862, telluric currents, which means “earth current” and etymologically comes from Latin word for earth “tellus”, has been known [22]. The idea using telluric currents in prospecting, is proposed in 1950 by Tikhonov and Cagniard [7].

Telluric currents are basically electromagnetic distortions in earth’s crust mainly caused by exterior stimulus like solar wind and thunderstorms.

In extraterrestrial source case, knowing that it is nothing more than high-speed moving ions, as solar wind come across earth’s magnetic field as shown in figure 1.8, it causes distortions that produces electromagnetic energy. A certain amount of that energy propagates through earth, and a proportion of that penetrates the crust. Given that in principle the earth behaves like a conductor, this penetrated energy causes so called telluric currents which have relatively low frequencies [35].

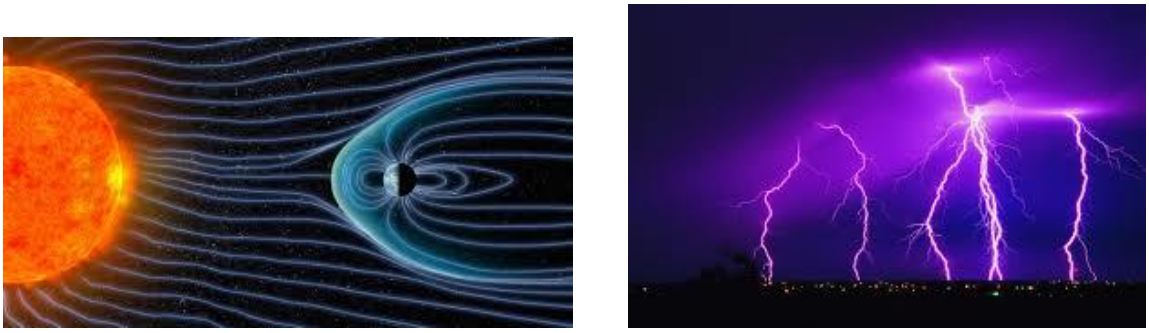

FIGURE 1.8: *MT current sources*

Thunderstorms can also be a factor for telluric current occurrences on higher frequencies with respect to previous scheme. In this scenario, spatial extent lays between surface and ionosphere acts like a waveguide to the energy being transported during a thunderstorm and a portion of this energy penetrates the earth [35].

Telluric currents are horizontally occurred eddy currents that generates magnetic fields [7]. Since telluric currents can create a second magnetic field, as a passive surveying technique, MT method requires instantaneous measurements of both magnetic and electric fields, magnetic in all three dimensions and electric in horizontal plane only. With the interpretation of the relationship between measured magnetic and electric fields, resistivity behavior of underlying structures can be estimated.

In magnetotellurics, incoming electromagnetic energy can be considered as plane waves, due to the great distance of their creation position to the surface and all electromagnetic phenomena obeys Maxwell's Equations (2.1-2.4) with displacement currents are ignored. Moreover, earth is assumed to obey Ohm's law (2.54) and magnetic permeability of the materials that form the crust are assumed to be equal to the magnetic permeability of free space.

Telluric currents and phenoma they cause are measured in low frequencies. Since their period can reach from milliseconds to millions of seconds, required observation time is relatively long. In figure 1.9 a typical MT spectrum is provided.

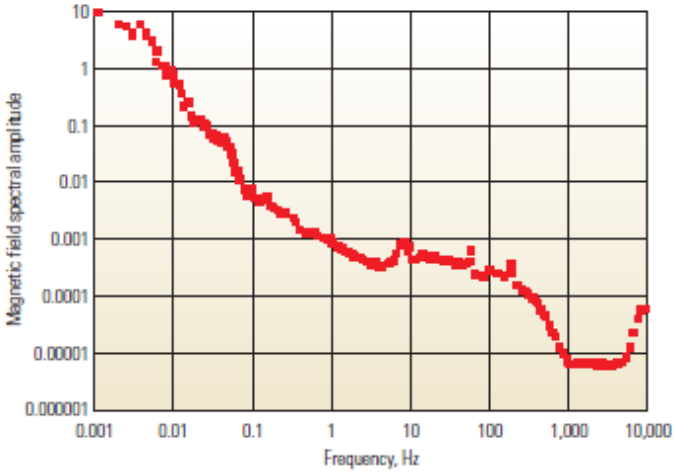

FIGURE 1.9: *MT spectrum* [7]

By using MT method, tens of kilometers of depth can be achieved for resistivity mapping. Even mantle can be reached as frequency goes smaller [7]. As prospecting method, MT plays a complementary role to seismic and even surpass it in certain conditions like volcanic cover and unconsolidated elements. Besides, MT is easier to implement and costs 75% less than seismic. However, it definitely provides worse spatial resolution due to relatively very low frequencies than those are used for seismic. MT method is briefly given here, because imaging techniques that are valid for CSEM are also available for MT imaging, as well. Moreover, MT represents a comparisonal reference for CSEM in most cases, which will occasionally be mentioned in subsequent sections.

1.2.4 Controlled source electromagnetic (CSEM)

During cold war, consideration of high-resistivity sub-seabed strata as a possible communication media in case of a probable nuclear war, had steered researches towards controlled source electromagnetic concept. After the work conducted by Charles Cox, who showed that at as low frequencies as 1 Hz and even lower, the electric field noise level was in the order of pV/m. Followingly in 70s, it is understood that a horizontally polarized electromagnetic waves that is sent downward to the sub-sea, can be detected from many kilometers away [7].

Pioneering surveys were done and data were yielded by Cox in 1979, just before Young and Chave, in 1980, first realized that CSEM surveys could have been used for hydrocarbon exploration. Unlike MT, it is spotted that CSEM was sensitive to high-resistivity regions which made it the focus of interest. At this point, the sector concentrated on some other problems, which were thought to be more important, like drilling. Also, air wave problem [5] of CSEM presented as an important problem to be solved. Thus, a break of a decade intervened. Along late 1980s and 1990s, departments for CSEM appeared in several universities and method developed for probing mid-ocean ridges and magmatic systems [3]. Correspondingly, industry

interest rose for CSEM, however, technological and economic restrictions did not let the method to become widespread.

As far as marine environment is concerned, CSEM won its first victory in 2000 in Angola. Therefore, an exaggerated interest appeared and soon after, several companies that offer CSEM surveys were founded. Unfortunately, in second half of the first decade of millennium, strong claims, misevaluation, excessive optimism and disintegration with other surveying techniques caused CSEM methods become debatable.

At the present time, in the light of progress made on processing the data, both in theory and computing capacity, CSEM is a respected method which can be seen as a perfect supplementary technique to the others.

Principally, as an active surveying technique, CSEM exploits the fact that a propagating wave in a diffusive media, which is sub-sea in this case, suffers distortion and mentioned distortion is a function of electromagnetic properties of the media and frequency of the signal used. This kind of remote sensing technique obviously requires a set of electromagnetic transmission and reception systems that will be discussed soon.

Off-shore CSEM is usually called marine CSEM (mCSEM) or towed CSEM since in practise, whole transmission system (in conventional CSEM) is towed by a multi purpose vessel as depicted in the figure 1.10. However, during the dissertation, by CSEM, CSEM conducted in marine environment will be mentioned.

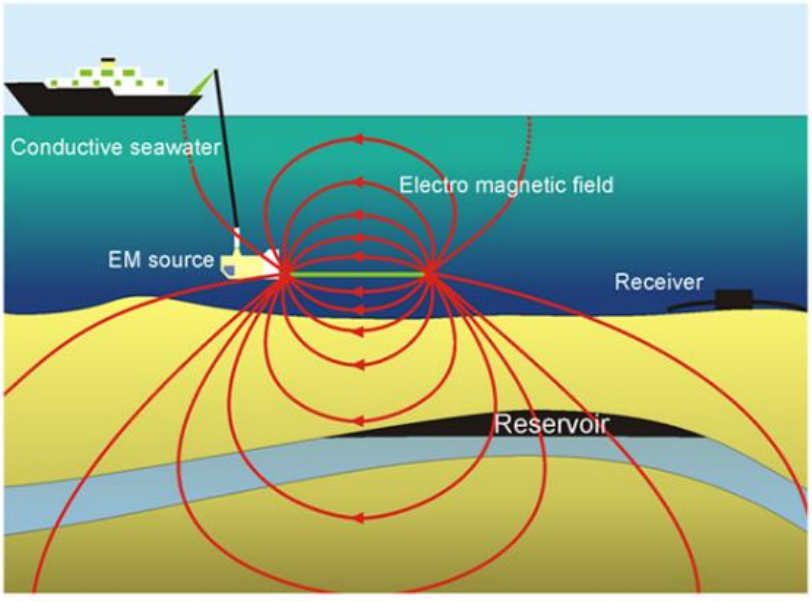

FIGURE 1.10: *A typical CSEM survey 1D section*

(taken from http://noc.ac.uk/)

In a conventional marine CSEM scheme, a transmission and processing section that basically consists of tow fish and the antenna may be shown as in figure 1.11. Here the antenna is expected to be high-powered horizontal electric dipole (HED) which typically have dipole moments in the order of 250000 Am and creates immense electric field vectors horizontally propagate towards sub-seabed. This is achieved by feeding two electrodes with high currents in between 0.01-10 Hz [3], typical frequencies for CSEM. Considering the dipole length can be set from 100 up to 300m, feeding current is reported to be generally in the order of few thousand Amperes (max 7500) in [3].

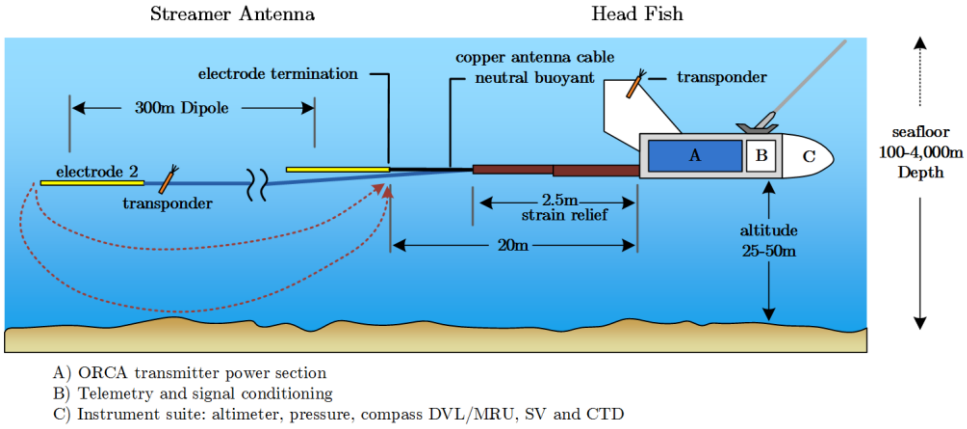

FIGURE 1.11: *CSEM transmission system* [23]

Tow fish, which generally consists of several inner comonents (A, B and C), is responsible for supplying power for the antenna, communication with surface terminals and environmental perception that is important for compensation of the received signal for the purpose of conducting a more realistic survey. In this scheme shown in figure 1.11, module A contains hardware that provides the required power, module B conducts signal conditioning and communications for controls which allows surveyor to work signal's quality control in real time. On the other hand, module C is responsible for sensing the environment in terms of altitude, pressure, direction etc.

In design, a copper cable lies through the horizontal plane from a few meter-long strain relief to electrodes to feed them. Obviously, end section must be buoyant in order to conduct better acquisition.

In conventional approach, towfish, hence all transmission system, is towed about 20-50m above seabed, in the direction called inline. The experiment is to be repeated for multiple times, in parallel lines. Similarly, perpendicular axis is denoted as crossline.

Receivers, moslty placed grid fashion on the sea-bed, are responsible for the collection of fields created by transmitter. Then they are recovered for analysis. A typical CSEM receiver is given in figure 1.12.

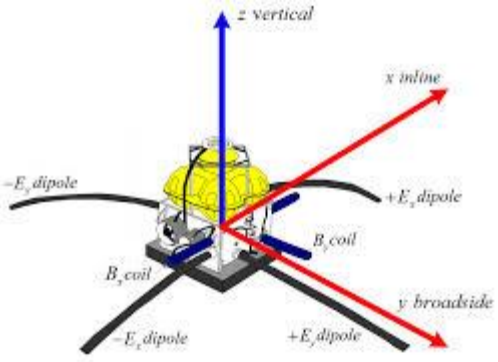

FIGURE 1.12: *CSEM ground receiver* [23]

Conventional receivers are desiged to measure horizontal fields mostly. However, it is not uncommon to gather also vertical components of electric and magnetic fields.

Up to now, CSEM concept with fixed ground receivers and deeply towed transmitter is mentioned. However, other CSEM approaches are introduced in literature as well. [9] introduced a compact scheme where receivers are located at the same streamer line, instead of seabed. In this approach transmission-reception system is towed just above seabed as shown in figure 1.13. This CSEM strategy is designed to map resistivity anomalies on very shallow depths upt to 250m, caused by gas hydrates.

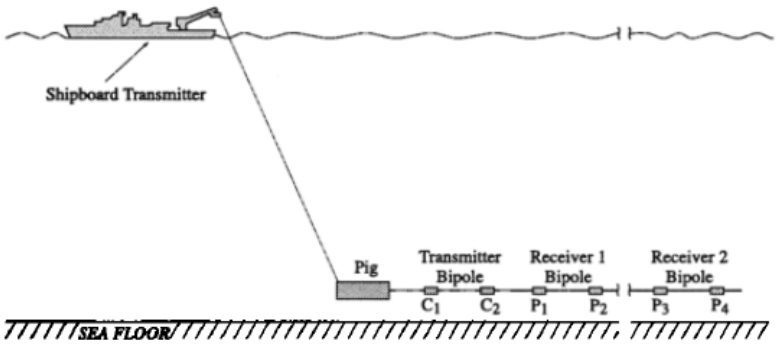

FIGURE 1.13: *A deep towed CSEM concept example where one directional receivers and transmitter are together positioned in the same line* [9]

Here, receivers are designed as horizontal dipoles as transmitter, hence, are capable of sensing only one component of electric field. Contrarily, the alternative system that [2] suggests uses very similar scheme. In this case receivers given in figure 1.14.a, which are capable of measuring electric field in 3 directions are towed behind transmitter antenna. Whole line is towed above 100m of seabed.

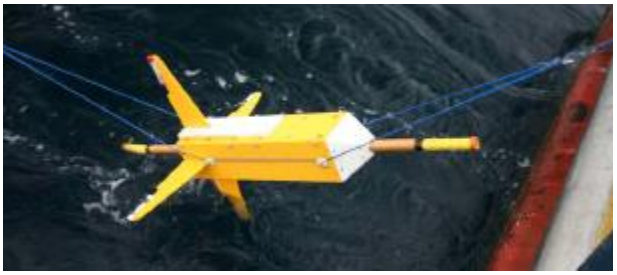

(a)

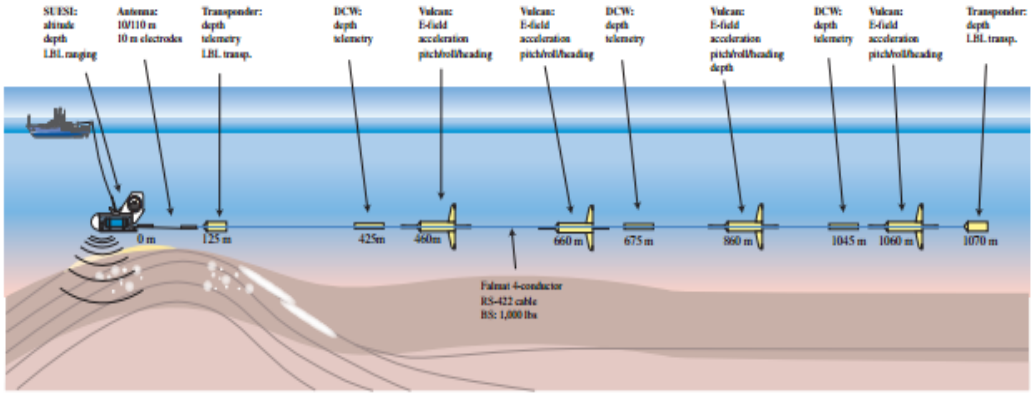

(b)

FIGURE 1.14: *A deep towed CSEM concept example where three directional receivers and transmitter are together positioned in the same line; (a) a typical receiver, (b) model and system layout* [1]

System is described in figure 1.14.b. states that, even though a much stronger noise is present with respect to conventional seabed placed receiver scheme, ability to arrange receivers' seperation is a powerful advantage in contrast to conventional CSEM. Because, conventional CSEM suggests receiver spacing between 500-2000m which causes to undersample shallower resistivity structures. In this method, transmitter-receiver offset up to 1 km is supported. Thus relatively shallower resistive structures are more likely possible for imaging. Chapter 3 will be subject to investigation of advantages, drawbacks and limitations of this kind of CSEM concepts.

Another approach, shown in figure 1.15, includes the concept that transmitter and receivers are towed together as in two cases previously introduced, however, satisfying very long transmitter-receiver offsets this time [27]. In this scheme, shallower towing depths are presented as 10-100 meters below the surface. However, system will be under investigation in chapter 3 for a wide range of towing depth for various sea depths.

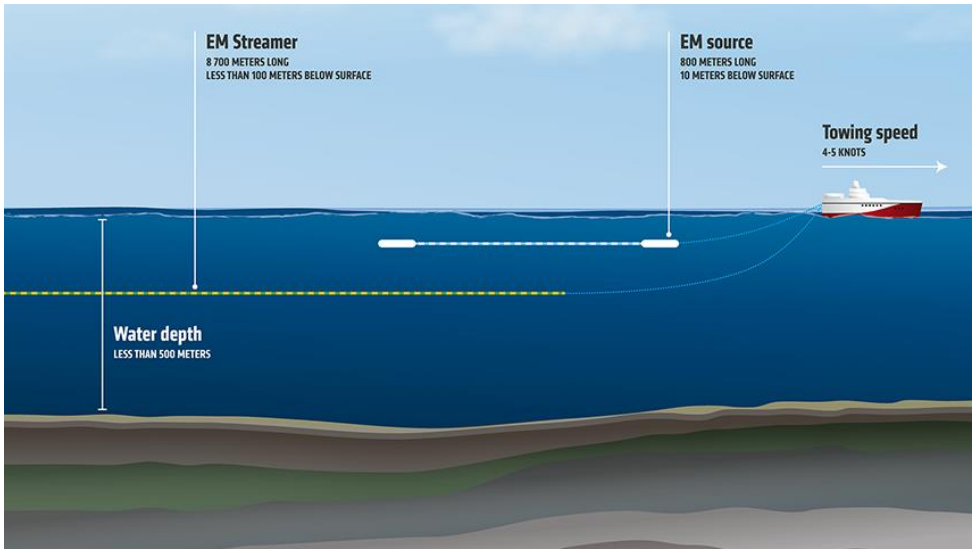

FIGURE 1.15: *A surface towed CSEM concept example where receivers and transmitter are together positioned in the same altitude* [8]

Also in this scheme, inline horizontal electric dipole receivers are implemented. System principally aims waters as shallow as 500m.

The last CSEM surveying technique wil be discussed in this thesis is the one suggested by [28]. In this variant, shown in figure 1.16., transmitter and receiver antennas placed vertically with respect to seabed.

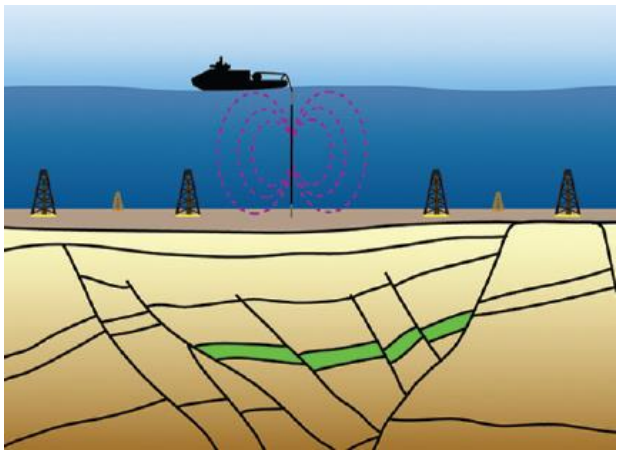

FIGURE 1.16: *A conventional mannered fixed CSEM approach, but transmitter and receivers are positioned vertically this time* [3]

The drawback of this kind of CSEM configuration is that, vertical electric field responses are significantly smaller than conventional CSEM case. Thus, in order it not to be dominated by horizontal fields, only small tilt angles are said to be tolerated [3]. Nevertheless, resistive structures can be sensed in much shorter offsets than conventional CSEM.

Chapter 2

Theory

In this chapter, basic physical concepts, which will be referred often afterwards, is presented briefly. Among them, Maxwell's equations, plane wave solution, polarization, reflection and refraction phenomena, and skin depth are present. Moreover, meaning of skin depth and resistivity of underground structures will be covered, which is one of the most important key points understading the limits of CSEM.

2.1 Maxwell's equations

In order to have a comprehensive competence on the principles of CSEM method, it is crucial to start with the nature of electromagnetism. In the light of the fact that the behaviour of all electric and magnetic fields that existed in the past or will exist in the future, in a material or in free space can be explained by 4 fundamental laws depicted by Maxwell.

The first one is Gauss's law. Gauss's law means that the net electric field (or can be thought as the density or number of electric field lines) which leaves a closed surface in three dimensional space, regardless of the shape of the surface, depends only on the total (net) charges within that surface where E is the magnitude of electric field vector in Volts per meter (Vm^{-1}).

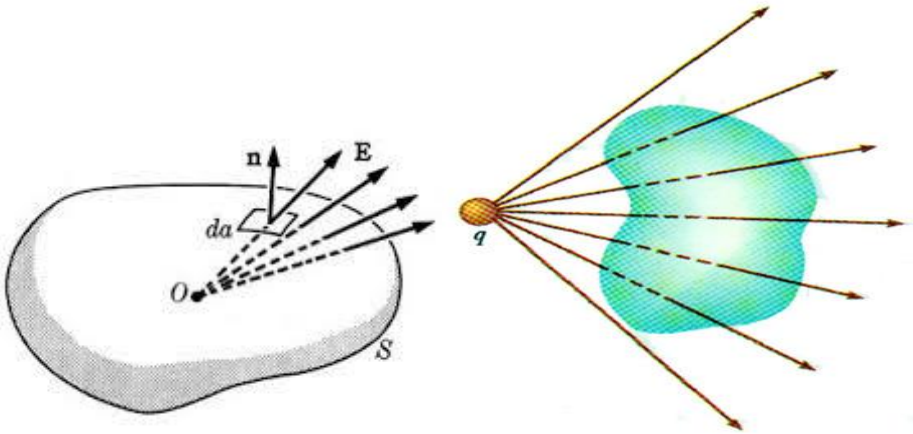

(a) (b)

FIGURE 2.1: *Gauss' law; (a) interior charges, (b) exterior charges*

Here in integral form, **Ω** is volume (m^3) determined by that surface and ρ is volume charge density (C/m^3).

As can be seen in figure 2.1, outer charges does not contribute the net electric field flow throughout the surface, because in outer charge case, entering and exiting electric field components are exactly the same and they cancel each other.

Second one, which is called again Gauss's law for magnetism states that, since no magnetic monopole is thought to exist, net magnetic flux (Volts*seconds) that leaves off or penetrates a closed surface regardless of its shape is zero.

Third one is called Ampere's Law with an extension made by Maxwell himself. While traditional understanding of how magnetic field loops ingenerates around a current flow direction, relates the phenomena only by the amount of that current, Maxwell added a second term, displacement current $\overrightarrow{J_d} = \varepsilon \frac{d\vec{E}}{dt}$ showing the magnetic field generation is also connected with the electric field rate of change by time that goes through the loop. Besides this term explains how current flows through a capacitor's conducting plates without a conductor,

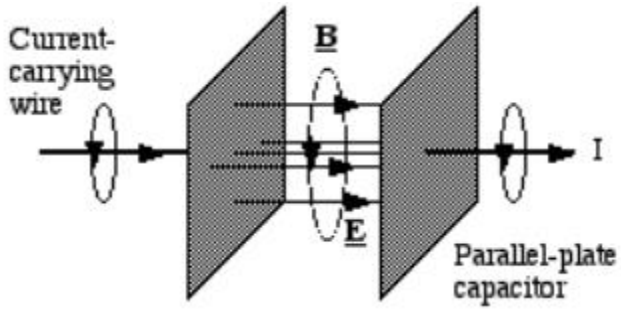

FIGURE 2.2: *Displacement currents*

(taken from http://www3.imperial.ac.uk/)

which basicly paved the way for comprehending how electromagnetic energy propagates. Here ∑ respresents the surface that current flows through and δ∑ is the closed boundary of that surface (2.3).

The last one is Faraday's Induction Law which simply states a magnetğc flux change throughout a surface, creates an electric field along the closed boundary of that surface.

Differential Form	Integral Form	
$\nabla \cdot \mathbf{E} = \frac{\rho}{\varepsilon_0}$	$\oiint \mathbf{E} \cdot \mathrm{d}\mathbf{S} = \frac{1}{\varepsilon_0} \iiint_\Omega \rho \, \mathrm{d}V$	(2.1)
$\nabla \cdot \mathbf{B} = 0$	$\oiint \mathbf{B} \cdot \mathrm{d}\mathbf{S} = 0$	(2.2)
$\nabla \times \mathbf{B} = \mu_0 \left(\mathbf{J} + \varepsilon_0 \frac{\partial \mathbf{E}}{\partial t} \right)$	$\oint_{\partial \Sigma} \mathbf{B} \cdot \mathrm{d}\boldsymbol{\ell} = \mu_0 \iint_\Sigma \mathbf{J} \cdot \mathrm{d}\mathbf{S} + \mu_0 \varepsilon_0 \frac{\mathrm{d}}{\mathrm{d}t} \iint_\Sigma \mathbf{E} \cdot \mathrm{d}\mathbf{S}$	(2.3)
$\nabla \times \mathbf{E} = -\frac{\partial \mathbf{B}}{\partial t}$	$\oint_{\partial \Sigma} \mathbf{E} \cdot \mathrm{d}\boldsymbol{\ell} = -\frac{\mathrm{d}}{\mathrm{d}t} \iint_\Sigma \mathbf{B} \cdot \mathrm{d}\mathbf{S}$	(2.4)

B is magnetic flux density in Tesla (kg s^{-2} A^{-1}). For the sake of a better understanding how electric and magnetic fields effect each other, assume a source free configuration. In this case, setting J = 0 and $\rho = 0$, equations become,

$$\vec{\nabla} \cdot \vec{E} = 0 \tag{2.5}$$

$$\vec{\nabla} \cdot \vec{B} = 0 \tag{2.6}$$

$$\vec{\nabla} \times \vec{B} = \frac{1}{C}\frac{d\vec{E}}{dt} \tag{2.7}$$

$$\vec{\nabla} \times \vec{E} = -\frac{1}{C}\frac{\vec{B}}{dt} \tag{2.8}$$

If the curl of (2.8) is taken, we have

$$\vec{\nabla} \times \vec{\nabla} \times \vec{E} = \vec{\nabla} \times \left(-\frac{1}{C}\frac{d\vec{B}}{dt}\right) = -\frac{1}{c^2}\frac{d^2\vec{E}}{dt^2} \tag{2.9}$$

and in the light of the vector equation

$$\vec{\nabla} \times \vec{\nabla} \times \vec{A} = \vec{\nabla}(\vec{\nabla} \cdot A) - \nabla^2 \vec{A} \tag{2.10}$$

and reminding the divergence of electric field is zero

$$\vec{\nabla} \cdot \vec{E} = 0 \tag{2.11}$$

we finally have

$$\frac{d^2\vec{E}}{dt^2} - c^2 \nabla^2 \vec{E} = 0 \tag{2.12}$$

which is immediately recognized to be a wave equation with propagating speed of “c”given that “∇^2 “ is Laplacian operator:

$$\nabla^2 = \frac{d^2}{dx^2} + \frac{d^2}{dy^2} + \frac{d^2}{dz^2} \tag{2.13}$$

An arbitrary function of “f” as in one dimensional space:

$$f = (x \mp ct) \tag{2.14}$$

seems to satisfy the equation (2.12) as long as it propagates with the speed of light. However, for a proper investigation of CSEM case, further study should be done in electromagnetics.

2.2 Plane Wave Solution

In most general case, the electric field of propagating wave can be expressed as

$$\vec{E}(x, y, z, t) = \mathrm{Re}\left[\vec{E}(x, y, z)\ \exp(j\omega t)\right] \tag{2.15}$$

for the purpose of seperated representation of spatial and time dependence of the wave.

Derivating (2.15) w.r.t time, we reach (electric field changes only in z direction)

$$\frac{d^2\vec{E}}{dt^2} = - \omega^2 \vec{E} \tag{2.16}$$

and finally a time-independent expression of the field:

$$\nabla^2 \vec{E} = - \omega^2 \mu_0 \varepsilon_0 \vec{E} = \frac{d^2\vec{E}}{dz^2} = - \omega^2 \mu_0 \varepsilon_0 \vec{E} \tag{2.17}$$

is yielded. Expression (2.17) depicts uniform wavefronts propagating through z direction with a seperation of wavelength

$$\lambda = \frac{2\pi c}{\omega} \tag{2.18}$$

where we have angular frequency ω and wave number

$$k = \omega \sqrt{\mu_0 \varepsilon_0} \tag{2.19}$$

with an electric field component that can be assumed to be pointing x direction only as

$$\vec{E} = \vec{E}_x \, e^{-jkz} \tag{2.20}$$

with magnetic field pointing y direction and also changes only in z direction as depicted in figure 2.3.

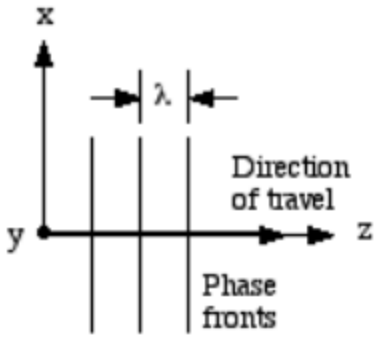

FIGURE 2.3: *Plane waves* [18]

When time dependence is also included, a general electric field illustration in 3 dimensional space is obtained as

$$\vec{E} = \mathrm{Re}\left[e^{-j(kz - wt)} \right] \hat{\imath} \tag{2.21}$$

Every propagating wave can be thought as a plane wave if far enough from the source.

2.3 Polarization

Polarization is the orientation of electric field lines related to an electromagnetic wave. In a general expression, the modulus of electric field can be defined as composed of two perpendicular components belong to the same plane as $E = E_x\ e^{-j(kz-\omega t+\theta x)} + E_y\ e^{-j(kz-\omega t+\theta y)}$.

Since k and ω values are the same for two components, regardless of E_x and E_y magnitudes, orientation of resulting electric field would be directional. This is known as linearly polarized wave as given in figure 2.4.

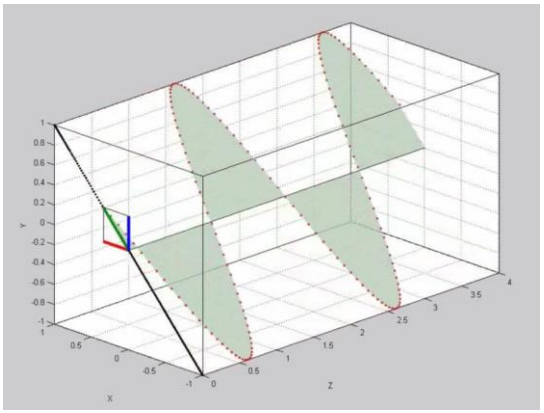

FIGURE 2.4: *Linear polarization*

In case perpendicular electric field magnitudes E_x and E_y are equal and a phase shift $\theta_x - \theta_y = \pi/2$ radians is present, orientation of total electric field is said to be circular as shown in figure 2.5.

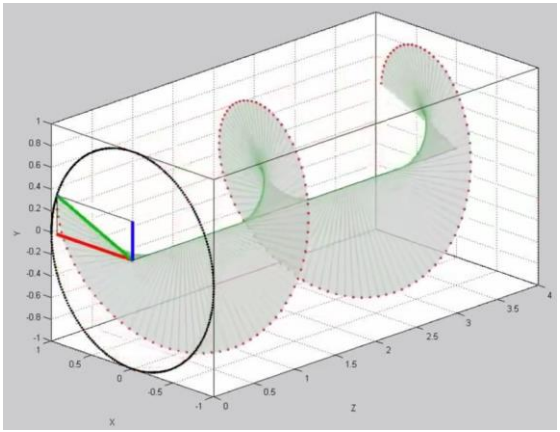

FIGURE 2.5: *Circular polarization*

Finally, wave is said to be elliptically polarized if E_x and E_y are not equal (when there is a phase difference apart from 0, $\pi/2$ radians), because lotus traced of the electric field vector is and ellipse, as a function of time.

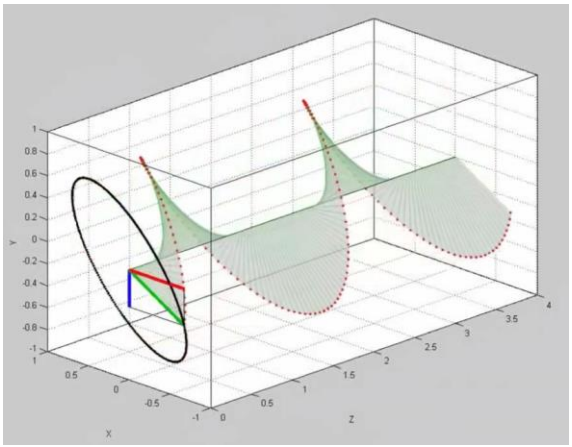

FIGURE 2.6: *Elliptic polarization*

In CSEM applications, received waves have been elliptically polarized, even though transmitted ones are linearly polarized.

2.4 Reflection and Refraction of Electromagnetic Waves

A realistic study on CSEM applications requires the investigation on propagation of electromagnetic waves aslo in the presence of discontinuities beside different media, as well as in homogeneous medium and free space. For that purpose, configuration given in figure 2.7 can be considered.

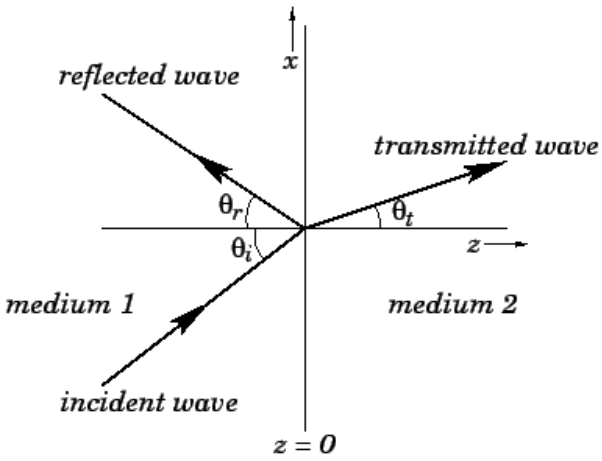

FIGURE 2.7: *Reflection and refraction*

(taken from http://farside.ph.utexas.edu/)

Here, an incident wave is coming towards a uniform boundary between two different medium with an incident angle θ_i different from zero or $\pi/2$ radians is depicted alongside a transmitted wave with the angle of θ_t and a reflected wave that is subject to θ_r. Wave vectors should be defined as

$$\hat{k}_i = \sin(\theta_i)\,\hat{x} + \cos(\theta_i)\,\hat{z} \tag{2.22}$$

$$\hat{k}_r = \sin(\theta_r)\,\hat{x} - \cos(\theta_r)\,\hat{z} \tag{2.23}$$

$$\hat{k}_t = \sin(\theta_t)\,\hat{x} + \cos(\theta_t)\,\hat{z} \tag{2.24}$$

In most general case, incoming electric field must be considered to be polarized in an arbitrary plane which includes $\hat{k}_i$, thus, electric field is said to be comprised of components in $\hat{y}$

$$\vec{E}_i = E_i\,\hat{y}\,e^{-j\hat{k}_i\vec{r}} \tag{2.25}$$

and in perpendicular to incidence wave vector $\hat{k}_i$ as

$$\vec{E}_i = E_i\,(\cos(\theta_i)\,\hat{x} - \sin(\theta_i)\,\hat{z}\,)\,e^{-j\hat{k}_i\vec{r}} \tag{2.26}$$

with corresponding magnetic field vectors

$$\vec{B}_i = B_i\,(-\cos(\theta_i)\,\hat{x} + \sin(\theta_i)\,\hat{z}\,)\,e^{-j\hat{k}_i\vec{r}} \tag{2.27}$$

and

$$\vec{B}_i = B_i\,\hat{y}\,e^{-j\hat{k}_i\vec{r}} \tag{2.28}$$

respectively. Similarly, reflected electric $\vec{E}_r$ and magnetic $\vec{B}_r$, and transmitted electric $\vec{E}_t$ and magnetic $\vec{B}_t$ field components can be given as following

$$\vec{E}_r = E_r\,\hat{y}\,e^{-j\hat{k}_r\vec{r}} \tag{2.29}$$

$$\vec{E}_r = E_r (\cos(\theta_i)\, \hat{x} + \sin(\theta_i)\, \hat{z})\, e^{-j\hat{k}_r \vec{r}} \quad (2.30)$$

$$\vec{B}_r = B_r (\cos(\theta_r)\, \hat{x} + \sin(\theta_r)\, \hat{z})\, e^{-j\hat{k}_i \vec{r}} \quad (2.31)$$

$$\vec{B}_r = -B_r\, \hat{y}\, e^{-j\hat{k}_i \vec{r}} \quad (2.32)$$

$$\vec{E}_t = E_t\, \hat{y}\, e^{-j\hat{k}_t \vec{r}} \quad (2.33)$$

$$\vec{E}_t = E_t (\cos(\theta_t)\, \hat{x} - \sin(\theta_t)\, \hat{z})\, e^{-j\hat{k}_i \vec{r}} \quad (2.34)$$

$$\vec{B}_t = B_t (-\cos(\theta_t)\, \hat{x} + \sin(\theta_t)\, \hat{z})\, e^{-j\hat{k}_i \vec{r}} \quad (2.35)$$

$$\vec{B}_t = B_t\, \hat{y}\, e^{-j\hat{k}_i \vec{r}} \quad (2.36)$$

where r is position vector.

For the sake of satisfaction of basic laws along all over the space, in medium 1, medium 2 and along the boundary within our scheme, a set of boundary conditions are definable. Accordingly, additive net electric and magnetic fields measured just left hand side and right hand side of the boundary must be equal to each other. Therefore, equations

$$\overrightarrow{|D_i|}\, e^{-j\hat{k}_i \vec{r}} + \overrightarrow{|D_r|}\, e^{-j\hat{k}_r \vec{r}} = \overrightarrow{|D_t|}\, e^{-j\hat{k}_t \vec{r}} \quad (2.37)$$

$$\overrightarrow{|B_i|}\, e^{-j\hat{k}_i \vec{r}} + \overrightarrow{|B_r|}\, e^{-j\hat{k}_r \vec{r}} = \overrightarrow{|B_t|}\, e^{-j\hat{k}_t \vec{r}} \quad (2.38)$$

must be satisfied. Through boundary where z=0, 1 and 2 is satisfied when equation

$$\hat{k}_i \vec{r} = \hat{k}_t \vec{r} = \hat{k}_r \vec{r} \quad (2.39)$$

is valid. As stated previously, incident wave vector does not have component in y direction. Hence, according to (2.39), reflected and transmitted wave vectors do not have y components as well, which means they lie on x-z plane, as incoming wave does.

Benefiting Snell's law

$$\frac{\sin\theta_1}{\sin\theta_2} = \frac{v_1}{v_2} = \frac{\lambda_1}{\lambda_2} = \frac{n_1}{n_2} \quad (2.40)$$

where v, λ, n are velocity and wavelength of propagating wave and refractive index of media respectively, and magnitude relationship between electric and magnetic fields

$$\left|\vec{B}\right| = \frac{|\vec{E}|}{v} \quad (2.41)$$

equation set (2.25)-(2.36) can be rearranged by taking into consideration (2.37), (2.38) given

$$\sin(\theta_i) = \sin(\theta_r) \quad (2.42)$$

Consequently, defining parameters

$$a = \frac{\cos\theta_t}{\cos\theta_i} \quad (2.43)$$

and

$$b = \frac{v_1}{v_2} \tag{2.44}$$

leads us to amplitudes of reflected and transmitted electric fields as

$$E_r = \left(\frac{1-a\,b}{1+a\,b}\right) E_i \tag{2.45}$$

$$E_t = \left(\frac{2}{1+a\,b}\right) E_i \tag{2.46}$$

which are polarized in y direction only.

Associated to the case that (2.45) identifies, reflection and transmission coefficient pair can be defined as

$$\Gamma = \left(\frac{E_r}{E_i}\right)^2 = \left(\frac{1-a\,b}{1+a\,b}\right)^2 \tag{2.47}$$

$$T = a\,b\left(\frac{2}{1+a\,b}\right)^2 \tag{2.48}$$

which tell how much of the energy reflects off or transfers throughout the other medium. Remembering, the incident wave was thought to be comprised of two waves, electric field of one of them purely polarized in y direction (case leads to 2.45) and electric field of one of them polarized in direction perpendicular to $\hat{k}_i$ and y direction. Reflected and transmitted electric field amplitudes with reflection and transmission coefficients related to second component of incident wave is found as

$$E_r = \left(\frac{a-b}{a+b}\right) E_i \tag{2.49}$$

$$E_t = \left(\frac{2}{a+b}\right) E_i \tag{2.50}$$

$$\Gamma = \left(\frac{E_r}{E_i}\right)^2 = \left(\frac{a-b}{a+b}\right)^2 \tag{2.51}$$

$$T = a\,b\left(\frac{2}{1+a\,b}\right)^2 \tag{2.52}$$

Reflective nature of electromagnetic waves and understanding physics behind, have been crucial for understanding whole CSEM concept.

Moreover, as immediately noticed, in case of a goes to b, (2.49) and (2.51) goes to zero which corresponds there is no reflected electric field in direction perpendicular to $\hat{k}_i$ and y direction. Resulting angle satisfies the equation

$$\sin(\theta_i) = \frac{b}{\sqrt{1+b^2}} \tag{2.53}$$

where θ_i is called Brewster angle. When incident angle takes this specific value, no matter how it was polarized before coming across the surface, after interaction, electric field of reflecting wave is purely plane polarized, polarized in y direction in our case.

2.5 Skin Depth

Up no now, propagation in free space has been wieved. Since CSEM deals with electromagnetic propagation in matter, to consolidate our study in a more realistic background we should investigate electromagnetic propagation also in materials. To do so, the simplest version of Ohm law

$$\vec{J} = \sigma\vec{E} \tag{2.54}$$

which was ignored before must be considered now. Also, a specific permittivity defined for particular material

$$\varepsilon = \varepsilon_0 \, \varepsilon_r \tag{2.55}$$

must be taken into account.

Relative permittivities of some important materials are given in table 1

Table 1: *Relative electrical permittivities of various materials some of which govern CSEM*

Material	ε_r (Davis and Annan, 1989)	ε_r (Daniels , 1996)
Air	1	1
Distilled water	80	
Fresh water	80	81
Sea water	80	
Fresh water ice	3–4	4
Sea water ice		4–8
Snow		8–12
Permafrost		4–8
Sand, dry	3–5	4–6
Sand, wet	20–30	10–30
Sandstone, dry		2–3
Sandstone, wet		5–10
Limestone	4–8	
Limestone, dry		7
Limestone wet		8
Shales	5–15	
Shale, wet		6–9
Silts	5–30	
Clays	5–40	
Clay, dry		2–6
Clay, wet		15–40
Soil, sandy dry		4–6
Soil, sandy wet		15–30
Soil, loamy dry		4–6
Soil, loamy wet		10–20
Soil, clayey dry		4–6
Soil, clayey wet		10–15
Coal, dry		3.5
Coal, wet		8
Granite	4–6	
Granite, dry		5
Granite, wet		7
Salt, dry	5–6	4–7

To have a more general idea on permittivity, in the light of fourier transform

$$F(\omega) = \int_{-\infty}^{\infty} dt\, f(t) e^{-j\omega t} \tag{2.56}$$

and Maxwell's equations obtained by execution of Fourier transform into them

$$\nabla.\vec{E} = \frac{\rho}{\varepsilon} \tag{2.57}$$

$$\nabla.\vec{B} = 0 \tag{2.58}$$

$$\nabla \times \vec{H} = (\vec{J} + j\omega\varepsilon)\,\vec{E} \tag{2.59}$$

$$\nabla \times \vec{E} = -j\omega\mu\vec{H} \tag{2.60}$$

and implementing (2.54), a complex permittivity

$$\varepsilon_c = \varepsilon' \left(1 - j\,\frac{\sigma}{\omega\varepsilon'}\right) \tag{2.61}$$

where

$$\varepsilon' = \varepsilon_0 \, \varepsilon_r \tag{2.62}$$

can be reached. Here, a complex wavenumber related to a complex permittivity arises as

$$k_c = \omega \sqrt{\mu \varepsilon_c} \tag{2.63}$$

On the other hand in time domain, (2.54) states that, in the presence of an electric field of amplitude E, a current density $\vec{J}$ arises inside a material with conductivity σ. We immediately see that, the current density an electromagnetic wave with electric field component (2.21) causes, flows in material with resistivity

$$\rho = \frac{1}{\sigma} \tag{2.64}$$

and results in a power dissipation that is revealed as heat. This is called Joule heating [22]. In microscopic scale,

$$\frac{dP}{dV} = J \, E \tag{2.65}$$

is valid where $\frac{dP}{dV}$ represents power per unit volume similar to macroscopic well known equation

$$P = I \, V \tag{2.66}$$

Now, due to the presence of J, we must consider the equation (2.3) instead of (2.7). Following the same steps done before, taking rotational of (2.4) and substituting in (2.3) and using vector relationship (2.10), with addition of (2.54), equation

$$\nabla^2 \vec{E} + (\omega^2 \mu_0 \varepsilon - j\omega \mu_0 \sigma) \vec{E} = 0 \tag{2.67}$$

is reached. Notice that, source current is not included here. It is clear that the new wave number is

$$k = \sqrt{\omega^2 \mu_0 \varepsilon - j\omega \mu_0 \sigma} \tag{2.68}$$

assuming like most of the materials, medium subject to propagation now, has magnetic permeability very close to the permeability of free space as $\mu \approx \mu_0$.

(2.68) is very important for CSEM analysis, which will be covered in subsequent chapters.

Instead real wavenumber appears in time independent electric field expression (2.20) now we have complex wave number like

$$k = \alpha + j \, \beta \tag{2.69}$$

with real and imaginary parts shown as α and β, respectively. From (2.60), (2.63) and (2.68), real and imaginary parts of complex wavenumber k can be obtained as

$$\alpha = \omega \sqrt{\frac{\mu \varepsilon'}{2} \left[\sqrt{1 + \left(\frac{\sigma}{\omega \varepsilon'} \right)^2} - 1 \right]} \tag{2.70}$$

$$\beta = \omega \sqrt{\frac{\mu\varepsilon'}{2}\left[\sqrt{1+\left(\frac{\sigma}{\omega\varepsilon'}\right)^2}+1\right]} \tag{2.71}$$

respectively

In this new representation, equation

$$\vec{E} = |\vec{E}|\, e^{-j\,\alpha\, z}\, e^{-\beta z} \tag{2.72}$$

indicates time independent behaviour of the field. Here the real term of wavenumber, "α" explains spatial propagation as in (2.20), however a new term β is introduced, which is responsible for generation a real negative exponential quantity. It is clear that quantitiy, in the multiplication situation with field amplitude, will decrease by increasing z, which results in a decrease in a field amplitude. Skin depth, is basically position z, where exponential decay causes the field amplitude e^{-1} times the field amplitude in position z=0 as given in figure 2.8, for a plane wave propagates in direction of z. It is shown as δ and given by

$$\delta = \frac{1}{\beta} = \sqrt{\frac{2\rho}{\omega\mu}}\sqrt{\sqrt{(\rho\omega\varepsilon)^2}+\rho\omega\varepsilon} \tag{2.73}$$

As far as frequencies much smaller than 1/ρε, just like the CSEM case, skin depth is given as

$$\delta = \sqrt{\frac{2\rho}{\omega\mu}} \tag{2.74}$$

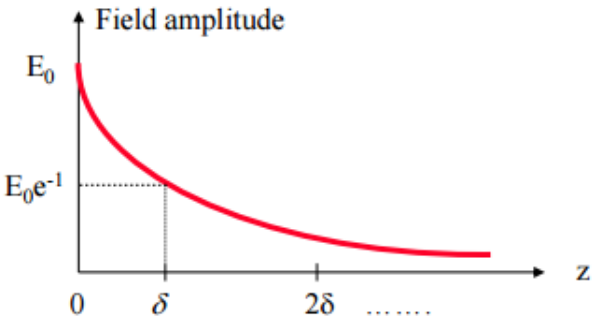

FIGURE 2.8: *Skin depth*

For resistivities and used frequencies related to CSEM surveys, a skin depth table is given by [17] as following:

Table 2: *Skin depths for various frequency and resistiviy*

Frequency (Hz)	Resistivity (Ω m)						
	0.3	1	10	50	75	100	300
0.1	866	1581	5000	11180	13693	15811	27386
0.3	500	913	2887	6455	7906	9129	15811
0.5	387	707	2236	5000	6124	7071	12247
1	274	500	1581	3536	4330	5000	8660
1.5	224	408	1291	2887	3536	4082	7071
5	122	224	707	1581	1936	2236	3873

Skin depth behaviour of diffusing wave, totally governs CSEM concept, because it clearly determines the limits of range. In other words, skin depth property, as a function of conductivity and frequency only, tells how quick an electromagnetic wave decays in a medium. Next section is studied for the purpose of a deeper look into resistivity behaviours of structures that are subject to CSEM surveys.

2.6 Resistivity behaviour of underlying structues

Previous section discussed how much further electromagnetic energy can propagate in lossy media. Since all resistivity surveys including CSEM, principally benefit resistivity differences, it is convenient to conduct a deeper study on resistivity behaviours of underlying materials that host propagating energy.

Different from resistance, which is a simple ratio between voltage and current given by ohm law (2.54), resistivity is the resistance per unit volume. In other words, voltage difference in unit distance present through a medium (Vm^{-1}) divided by the current that penetrates unit square (Am^{-2}) as

$$\rho = \frac{\Delta V}{J} \tag{2.75}$$

related the same portion of medium is basically, resistivity. Notice that resistivity is defined for a specific direction, thus it is a tensor in most general case.

Apart from conductive exceptions as carbon, graphite, pyrite, pyrrhotite, magnetite, rocks and soil that constitue underground structures are comprised mostly of minerals and silicate, which are non-conducting materials, indeed. Hence, occurances of less-resistive regions strictly depends on porosity and groundwater contained in pores, hydraulic permeability, dissolved electrolytes, clay amount and temperature [36].

As far as the effects of porosity on conductivity is concerned, Archie's empirical expression is a handy tool for relating porosity and conductivity of lyquid contained, with material's overall conductivity, or as referred in literature, bulk conductivity. This formula states that there is a strict exponential relation between relative resistivity and porosity, as

$$\frac{R_0}{R_\omega} = \Phi^{-m} \tag{2.76}$$

that is defined by coefficient m which is typically between 1.2 and 1.8. Here R_0 is the resistivity of pored structure in case it is fully filled with brine, and R_ω is the resistivity of brine itself.

When the pore filling lyquid is hydrocarbons, then overall resistivity behaviour of the structure is as given in figure 2.9.

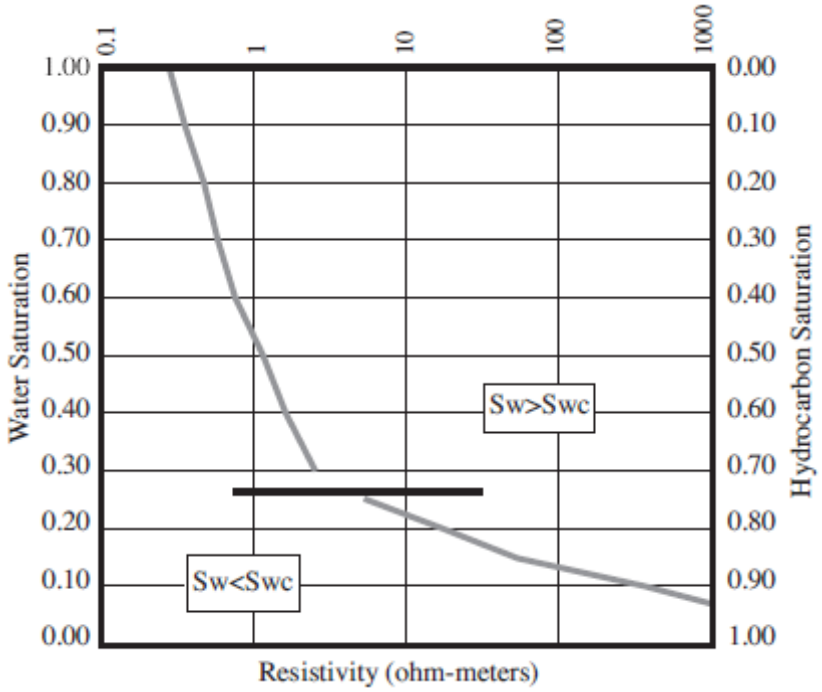

FIGURE 2.9: *Resistivity versus hydrocarbon saturation* [11]

On the other hand, dissolved electrolytes are important, because free ions exist in water moves in presence of electric field, which is the definiton of current itself. Dissolved ions are mostly due to NaCl content of ocean water. As far as conductivity as a function of salinity is concerned, as given in figure 2.10, a nearly linear relationship like

$$\sigma \approx \frac{C}{10} \tag{2.77}$$

is present for moderate temperatures (0 – 200 'C) where C $[g/l]$ is salinity.

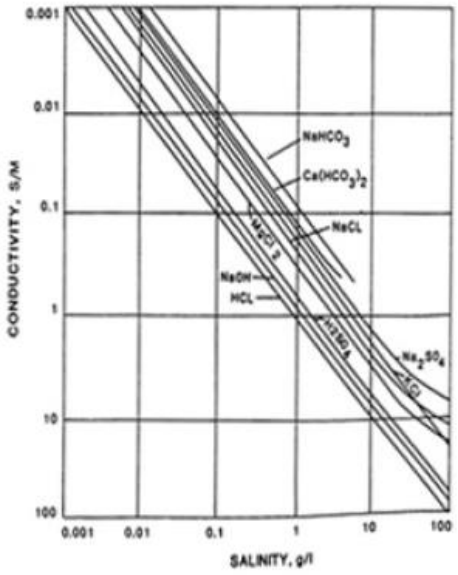

FIGURE 2.10: *Salinity versus conductivity* [12]

In addition, when temperature dependence is concerned in moderate intervals, it is found that conductivity increases with increasing temperature for various pressure values as shown in figure 2.11.

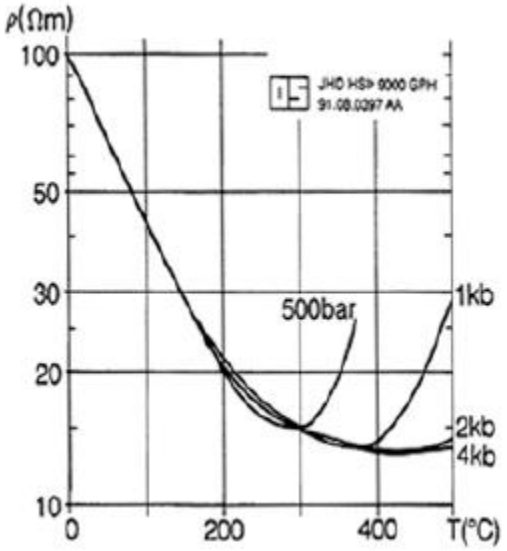

FIGURE 2.11: *Temperature versus conductivity* [12]

Dakhnov (1962) gives the relationship as

$$\rho_w = \frac{\rho_{w0}}{1+ \alpha(T-T_0)} \qquad (2.78)$$

where ρ_{w0} is resistivity of the fluid at temperature T_0 and α is the temperature coefficient of resistivity which is, for instance, equal to 0.023 ‘C^{-1} for T_0=0 ‘C and 0.023 ‘C^{-1} for T_0=23 ‘C.

The reason for tendency of increasing resistivity roughly after 300 ‘C is a decrease in electrical permittivity of the water because in this case number of ions in water also decreases.

2.7 HED Radiation

CSEM applications include linear antennas as electromagnetic transmitters horizontally placed above seabed and the Poynting vectors related to waves radiated, behaves as depicted in figure 2.12.

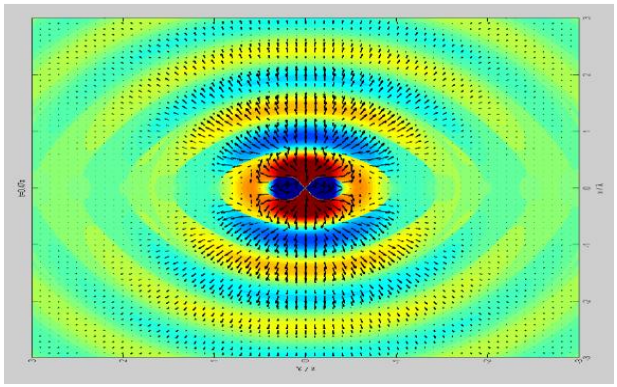

FIGURE 2.12: *HED radiation; Poynting vectors behaviour* [22]

As expected, radiation is concentrated in downward (toward subseabed) and upwards (toward air) for conventional CSEM. Downward propagating wave is the tool for entire operation, whereas, upward one causes airwave, which is a spoiling effect that will be mentioned later.

Hertzian dipole, which is the simplest linear antenna configuration that exists, is also a perfect starting tool to study real fields that are created by a physical dipole at distances very greater than antenna length. Because it turns out to be sources used in CSEM applications are very well approximated by Hertzian dipoles, whose radiation pattern is given in figure 2.13.

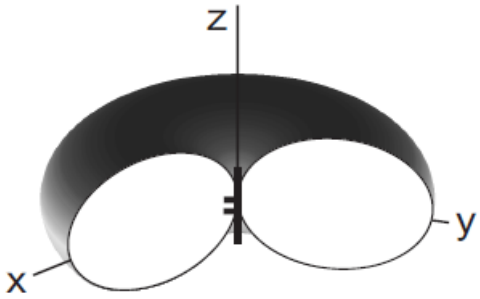

FIGURE 2.13: *Typical dipole 3D radiation pattern*

With the help of Green's functions, fields that are emitted by an infinitesimal antenna (length of antenna $l \ll \lambda$, the wavelength of the transmitted wave) with current density $I(\omega)l\delta(r)\hat{z}$ placed in origin, in spherical coordinates is given by [16]

$$E(r,\omega) = \frac{ik\eta Il}{4\pi r} e^{ikr} \left[- \left(1 - \frac{1}{ikr} + \frac{1}{(ikr)^2} \right) \hat{\theta} \sin\theta + \left(\frac{1}{ikr} - \frac{1}{(ikr)^2} \right) 2\hat{r} \cos\theta \right] \quad (2.79)$$

$$H(r,\omega) = \frac{ikIl}{4\pi r} e^{ikr} \left(1 - \frac{1}{ikr} \right) \left(- \hat{\Phi} \sin\theta \right) \quad (2.80)$$

where $I(\omega)$ is current amplitude. (2.79) and (2.80) describes fields propagations in CSEM environment.

Chapter 3

Sensitivity and Limitations For Various CSEM Models

3.1 Model Introduction

A classical view concerning CSEM experiments is depicted in figure 3.1. Here, resistive anomaly to be detected is present within a much less resistive background media wihch simply is sub-seabed. Although, receivers, which are located on sea-bed, will measure one specific trend of signal, a referance signal that simulates what would happen in case of no anomaly should artificially be constructed using background properties.

Apparently, in the presence of an electromagnetic transmission, two different media would respond the incoming wave differently according to their electromagnetic properties. Now assume an electromagnetic transmission experiment through two media differ only by their conductivities. It is clear that assuming the same system model and equipments are used (only media changes), the media with higher conductivity, would absorb more energy. This corresponds a smaller skin depth (2.74). In this case, the power that receivers, which are deployed on seabed in several hundreds of meters of seperations in conventional CSEM schemes, would register should be less than those would be registered in case of low conductive, high-resistive media. When more conductive media is considered as background matrix of resistivity 1 Ohm.m and resistive media is considered as hydrocarbon reservoir with 100m thickness and 100 Ohm.m resistivity placed 1000m below the sea floor as shown in figure 3.1,

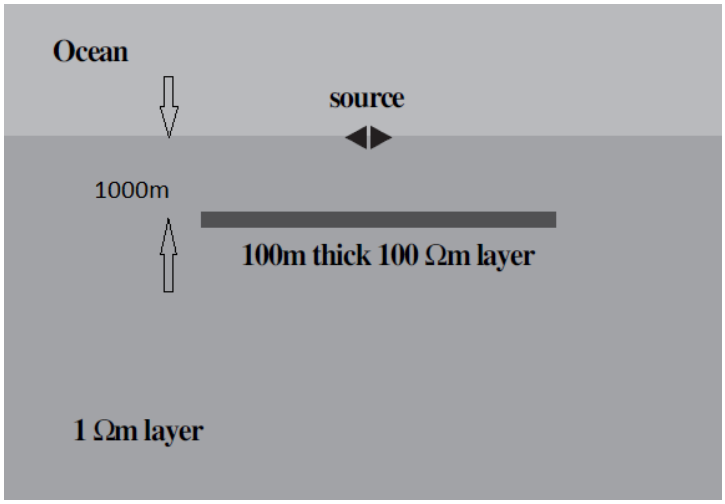

FIGURE 3.1*: A typical CSEM representation*

two different electric field behaviours that receivers (spaced 400m, 25 receivers) would measure, would be as given in figure 3.2:

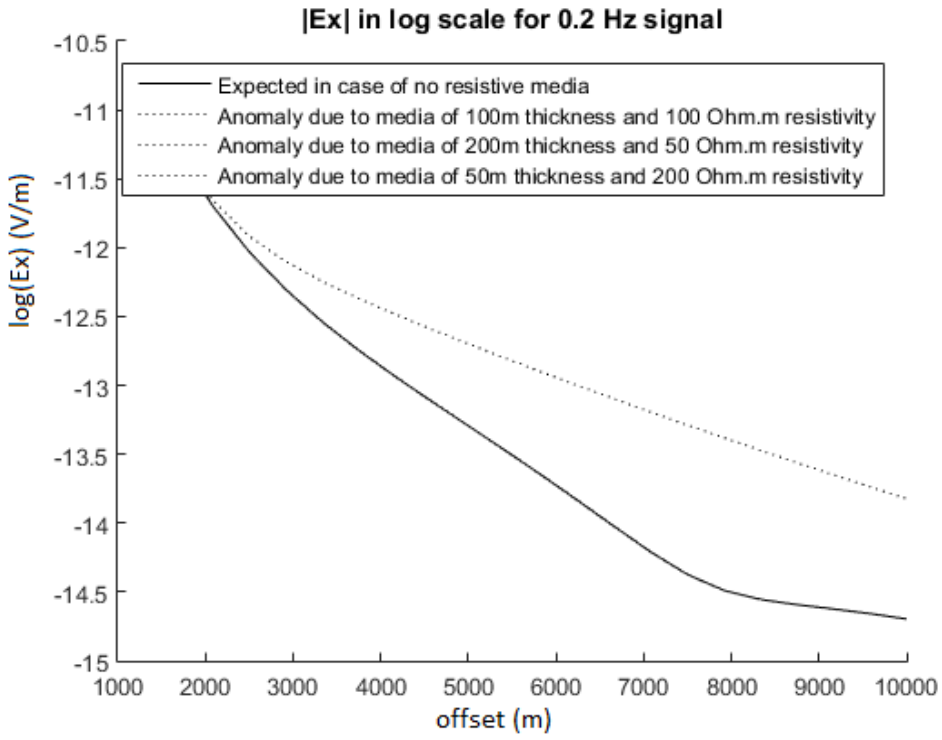

FIGURE 3.2: *Received field versus offsets in case of anomaly (dashed lines) and no anomaly (solid line)*

Although dashed one is received data, in real world, black curve that is related to background response in case of no reservoir is needed to be estimated, namely, it is needed to be created

artificially. It is clear that, once bakground model is given, comparison to real data reveals an enormous deviation which will make the surveyor conclude a significant reistive media is present below. Imaging methods and conditions will be discussed in latter sections. In this work, receiver noise level is considered as 10^{-15} [17] as in literature widely accepted.

In 1D demonstrations, usually, lateral extent of reservoir can be considered infinite. In our example, also inline component (length) of prospect tends to infinity for simplicity.

In figure 3.2, usual conditions for a typical mCSEM survey is set. As transmission frequency, 0.2 Hz, which is a good trade off between attenuation and SNR, is chosen. Moreover, water has conductivity is chosen to be 4 Sm^{-1} which is generally acceptable. Finally, transmitter is towed 30m above sea floor. Receivers are located 0.3m above seafloor and sea depth is chosen to be 1000m.

Property of attenuation difference just discussed, gives surveyor a powerful tool to distinguish different medium with different conductivities, and to map resistivity behaviours of underlying structures. Via this method, conventionally and roughly target depths to few thousand meters lie under from 500 to 3000 meters of water is said to be subject to detection under good conditions. Constraints and sensitivity parameters wil be discussed in subsequent section. However, care must be taken, because resistivity is not the only indicator of resistive fluid repletion of a certain pored structure, but also porosity and lithology variations can create a wide spectrum of resistivity.

3.2 Physical Properties

As will be discussed later, very low frequencies (like 0.01 Hz) provides poor resolvability of thin layer and very high frequencies (like 10 hz) simply decays too fast and provides nothing. Hence, a useful interval of frequencies to be used is present, however, all can not be used due to power budget reasons, transmitted signal is usually designed to look like the one in figure 3.3. Number of used harmonics for a typical CSEM survey is around 6.

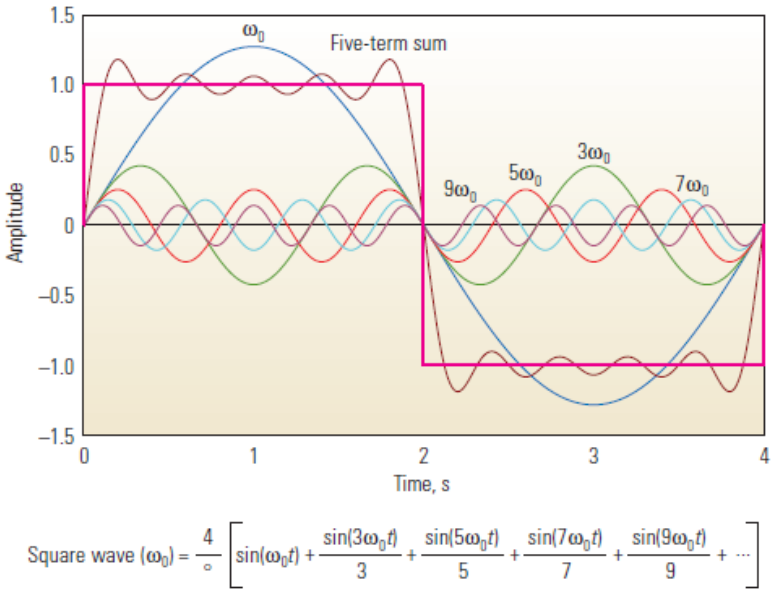

FIGURE 3.3: *Typical formation of CSEM transmitted signal* [7]

Attenuation behaviour of few chosen frequencies as harmonics, would be look like in figure 3.4.

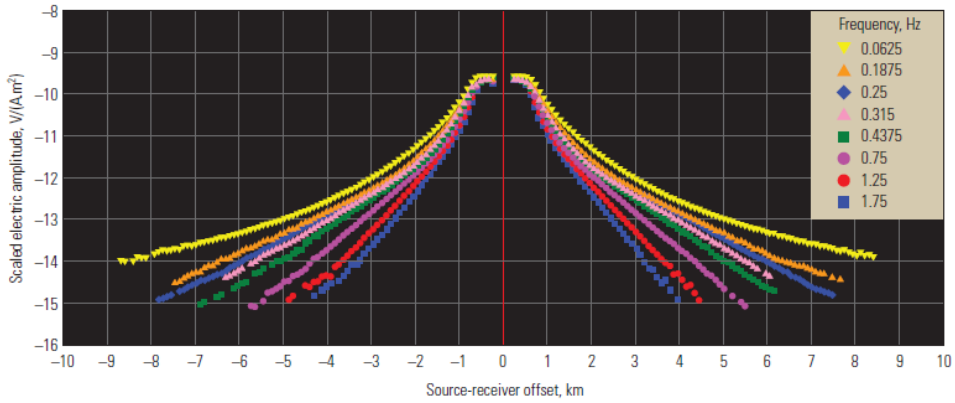

FIGURE 3.4: *Fading behaviour of different harmonics with respect to offset* [7]

It is clear the more frequency increases, the more likely for it to remain below sensitivity of receiver even in early offsets.

As far as the response of sub-seabed structures to these transmitted fields are concerned, [4] states that perturbations that can be sensible from kilometers away can happen in different ways. First one can be stated as *attenuation*, which is just discussed. Attenuation of a signal in diffusive media is governed by (2.74) and wavelength related to this signal is given as

$$\lambda = 2\pi\sigma \tag{3.1}$$

Notice that frequency dependent nature of skin depth provides consistency with figure 3.3.

Another perturbation is known as *galvanic effect*. Similar to boundary condition (2.37), boundaries must also satisfy the condition,

$$J^N = J_1^N = J_2^N \tag{3.2}$$

where J^N is the current density normal to the boundary surface and $_{1,2}$ represents the medium. Since (2.1) must be satisfied through boundaries as well, when included in the condition, a surface charged density as

$$\rho_s = J^N \left[\frac{\varepsilon_1}{\sigma_1} - \frac{\varepsilon_2}{\sigma_2}\right] \tag{3.3}$$

is reached. This surface charge accumulations creates observable pertubations in even in distant receivers.

Lastly, considering (2.37), (2.54) and (2.3) together, it is obvious that horizontal boundaries that are subject to great resistivity changes would cause great horizontal current densities. Vertical magnetic fields, as a consequence, are present on the surface. Perturbation is called *induction*, however, induction alone is not enough to be sensible on the surface. It must be considered as a powerful perturbation reason when metallic ores are present.

Since current density and electric field behaviours have deep impact in perturbation processes in the presence of thin resistive layers, for the sake of discussion it is important to study their distributional sights all over the diffusion medium. In figure 3.5a and b, current density vectors, which caused by a HED of 50000 A.m. of dipole moment lying on x direction, are shown in black arrows in case of DC signal. [4] have choosen zero frequency in figure 3.5 for comparisonal purposes, becasuse it represents a limit for frequency dependent behaviour of model.

Here z is the extent of depth. HED is placed 50m above the seabed, resistivity of water is chosen to be 3.33 Sm^{-1} and resistivity of uniform sub-seabed are set to 1 Ohm.m. Sea depth is 1 km. Besides, thin resistive layer is placed 1 km below sea-bed.

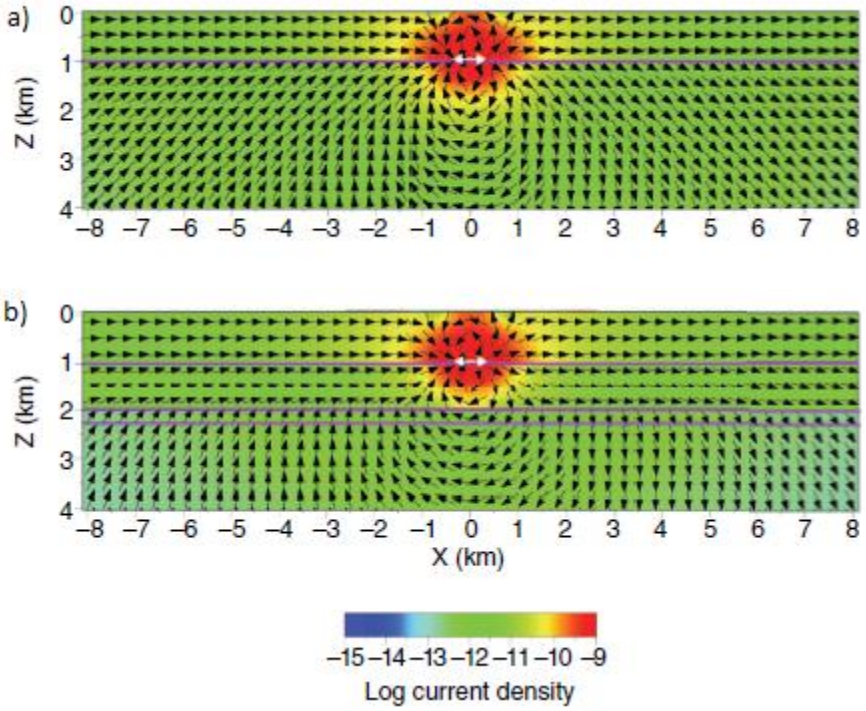

FIGURE 3.5.: *Electric field distribution for DC source; (a) for no anomaly, (b) for anomalous case* [4]

Without a disturbing thin resistive layer, which represents hydrocarbon reservoir here, current density distribution exhibits good order in lower half space. Both in cases given in figure 3.5a and b, current density suffers only from geometric dissipation inversely proportional to distance's third power. Note that since vertical currents are not supported by air, which is not conductive at all, through and just below the air-sea interface only parallel currents are observed. Similarly in b, [4] states that thin resistive layer prevents vertical currents. This causes tangential currents occur through upper and lower interfaces. As can be noticed visually as well, these are stong pertubations in deeper levels, however, in DC case galvanic and inductive perurbations are not sensible in surface. This is just because of masking effect of strong current components faded only in geometrical sense, but not faded in terms of dissipation. Reader can refer to figure 3.12 which will be given later, to clearly see frequency effect as far as sensing ability is concerned. [4] indicates a second reason for DC surveying being less sensitive is that most of the fields exist around resistive layer surface are subject to expression

$$E_1^T = E_2^T \tag{3.4}$$

which is not sensitive to the layer, where $_T$ stands for tangential.

As depicted in figure 3.6, when frequency increased, in background model, vertical currents around burial depth are remarkably more often comparing figure 3.5. Thus, addition of the thin resistive model into the case provides stronger galvanic effects, that are clearly observable on sea-bed surface.

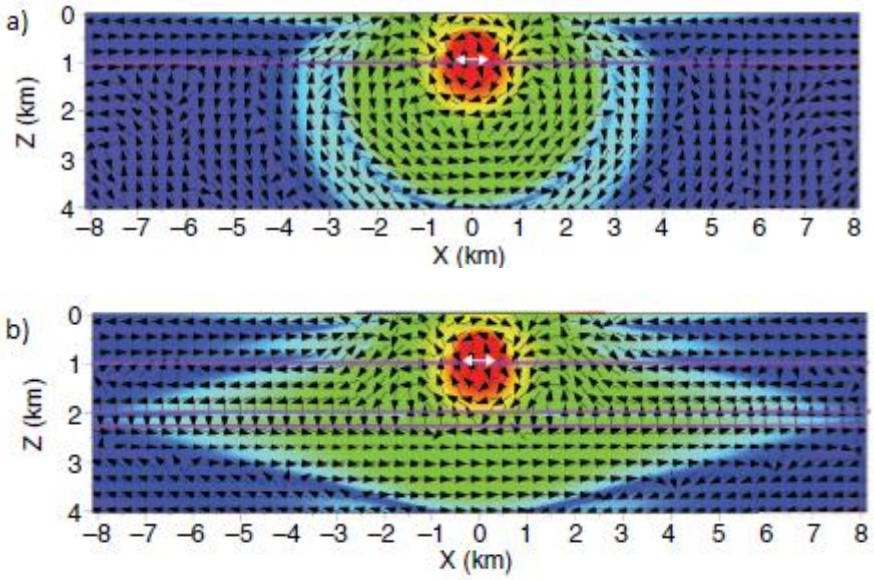

FIGURE 3.6.: *Electric field distribution for 1 Hz source; (a) for no anomaly, (b)for anomalous case* [4]

Further sensitivity analysis will be held in related section.

3.3 Propagation modes and parameters

Unlike seismic and well logging techniques, CSEM methods obey diffusion equations [16] and diffusion phenomena is subject to a wide portion of subsurface (as wide as skin depth) with all layers included. This makes CSEM senisitive to a vertical overall resistivity which causes the anomaly. As can be interpreted, a certain vertical resistivity can be the outcome of many combinations of varying thicknesses and differenial resistivities related to a buried hydrocarbon reservoir, hence, results in a certain anomaly. Therefore, considering the fact that the anomaly is not a function of resistivity only, but a function of resistivity and thickness of the target together, a new parameter; transverse resistance [5], which is simply a multiplication of resistivity and thickness, must be introduced. In figure 3.2 it is shown that different combinations of resisitivity and thickness values causes the same anomaly. This is a well known uncertainty.

Notice that, a certain vertical resistance can appear in case of vertically distributed target as well. Just because of very same reason, CSEM surveys conducted in the environments ,where the resistive body is relatively close to highly conductive basalt floor, has been difficult.

Once transmitted, electromagnetic waves follow several paths reaching receiver. Obviously, these paths determine how the measured signal would look like. Figure 3.7 depicts a general consideration of what kind of components received signal is comprised of. Assuming the antenna is located just above (h_s) the seabed, that is an half space with conductivity σ_1 apart

from a d_2 width layer buried under a depth of d_1, paths followed through different media are represented by Roman numerals. As a concept previously given, the thin layer just mentioned represents hydrocarbon reservoir with conductivity σ_2 very smaller than σ_1, causes perturbation to be detected.

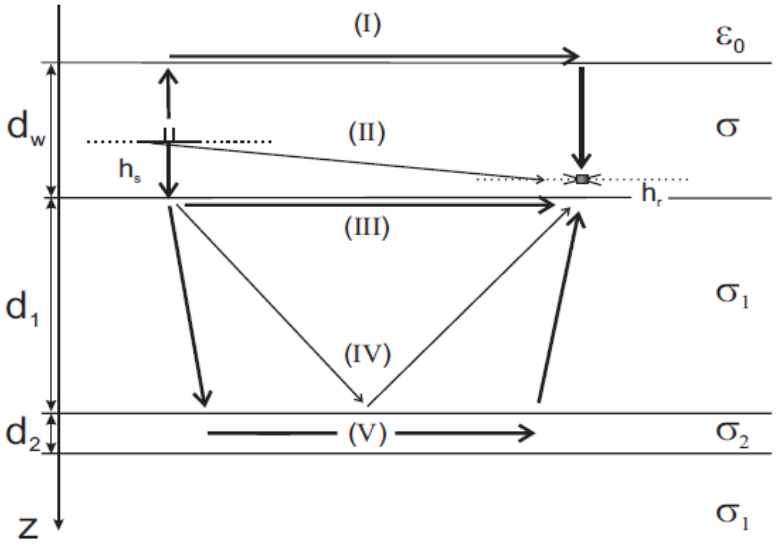

FIGURE 3.7.: *Propagation paths* [16]

As far as received signal strength versus transmitter-receiver offset (MVO) is concerned, figure 3.2 is able to represent the situation explained above, perfectly in one dimensional space. Since direct arrival (II) is still powerful, it clearly dominates the others in small distances both in anomalous and normal case. This means that perturbation due to anomaly is not observed in first few thousands of meters of offsets depending the skin depth in water, which is a function of frequency (2.74).

After a while, bearing in mind that brine is a more conductive medium than sub-seabed, signals originate from lateral wave on the floor-sea surface (III), reflected wave from reservoir (IV) and guided wave through the anomaly (V) will begin to reveal since they are attenuated less. That take over is cearly seen in figure 3.2 around offsets 2500m where a slight slope change is apparent for background model. From there on, received signal is represented by a combination of these three. Notice that in the absence of resistive anomaly, signal received in longer offsets is dominated by (III) only.

Yet, one should notice that the maximum difference of modulus of measured fields occur where well known airwave phenomena (I) becomes dominant in background model (7500m) with a visibility of slope changes again. Position of the offset that airwave would begin to dominate, is clearly a function of brine and background conductivities, frequency used and mostly sea depth. Airwave domination offset mostly depends on sea depth, because airwave is defined as a field suffers attenation as diffuses upward (vertically) , then propagates along air-sea surface interface suffering only geometric loss, finally diffuses vertically downward. Relatedly, in greater seperations, airwave is dominant, due to smaller attenuation caused mainly

by 2 d_w of water medium. This immediately leads that in shallower waters attenuation related to airwave would be smaller which results in disruptive effects. Idea is easily testable.

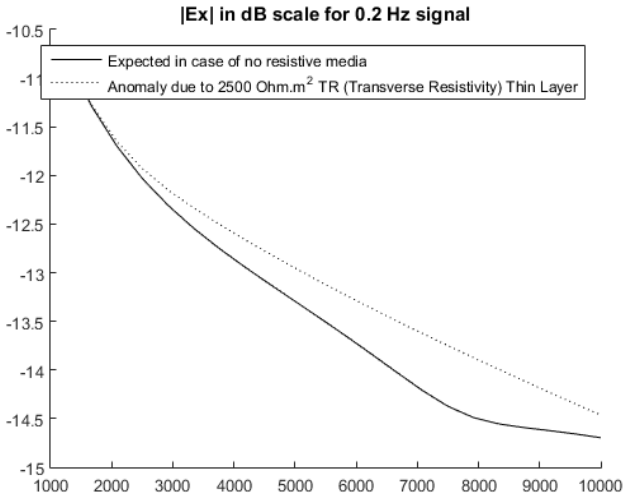

(a)

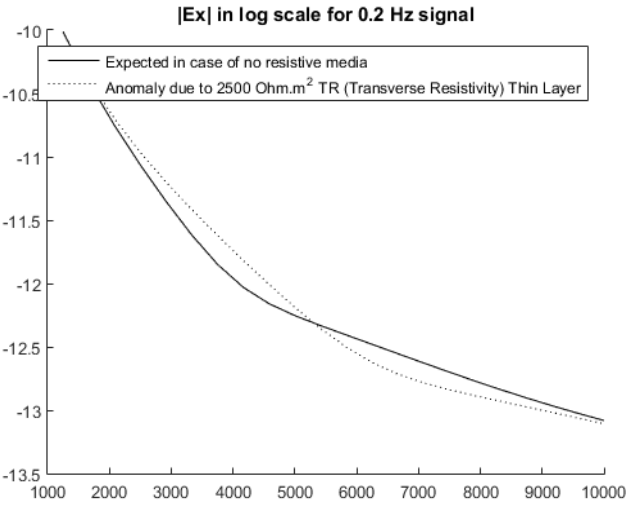

(b)

FIGURE 3.8.: *Impact of airwave; (a) sea depth of 1000m, (b) sea depth of 100m*

As shown in figure 3.8, which represents models differ one from another only in sea depth, particular offsets that airwave begin dominating are explicitly distinguishable. While airwave starts dominating about offsets 8000m in figure 3.8a, it takes over about offsets 4000m in figgure 3.3.3. It is immediately realized that a quick domination clearly decreases the quality of exploration by diminishing the difference between magnitudes of measured fields between background and anomaly cases.

3.4 Sensitivity and limitations

3.4.1 Conventional csem

Although figure 3.2 and 3.8 give clear empirical evaluation of the impact of an anomalous body within sub-seabed, a quantitative description of received signal differences is obviously necessary for more effective comparison as far as the ability to sense the target, which is simply called: sensitivty, is concerned.

Figure 3.8 differs from figure 3.2 only in transverse resistance. Considering TR is 4 times larger in case represented by figure 3.2, difference in observed field trends are noticeably distinguishable.

A very trivial expression of how much anomalous case differs from uniform one for a specific receiver (offset) k, could be given as

$$R_k = \left| \frac{E_a - E_{back}}{E_{back}} \right| \tag{3.5}$$

where E_a is denoted to complex electric field related to anomalous field (shown as dashed lines in previous figures), E_{back} represents complex electric field in case of no anomaly (indicated with solid lines through the whole work) and R is normalized instantaneous deviation from background model. Normalization step (denomitaor) is necessary for supression of the effect of attenuation. In literature, method is called Normalized Amplitude Response (NAR) [38].

Another version of deviation indication can take into consideration not the modulus of difference of fields (MODOF), but difference of modulus of fields (DOMOF) as

$$R'_k = \frac{|E_a| - |E_{back}|}{|E_a|} \tag{3.6}$$

Since (3.6) does not include phase, it is subject to infinitesimal values when measured field magnitudes are close enough. Indeed, as shown in figure 3.9b, which applies (3.6) to the case processed in figure 3.8.b, transition occurs where so called background model response becomes equal in amplitude, with anomalous response. However, (3.5) is clearly robust against transitions and due to Schwarz inequality. Thus, (3.5) represents the difference of fields in maximum possible manner and widely adpoted in literature.

Note that both these response interpretations are functions of sea depth, burial depth, transverse resistance of reservoir, frequency, and positions of transmitter and receivers.

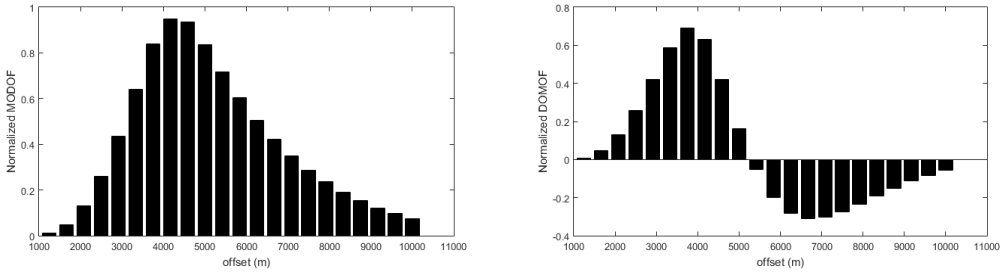

(a) (b)

FIGURE 3.9.: *NAR behaviours versus offset depicting the cases represented in figure 3.8b; (a) NAR vs offset for MoDoF approach,, (b) NAR vs offset for DoMoF approach*

Although, (3.5), (3.6) thus, figure 3.9 comprehensively provides the response seperations between background model and observed data, for practical reasons, it is important to represent whole response related to all offsets by a single quantity. A very straightforward one can be determined as

$$V = \frac{1}{N}\sum_{k}^{N} R_k \tag{3.7}$$

where V respesents the mean value of field differences related to receivers, and N is the nuber of receivers. This representation is a powerful and simple tool when comparing models with different parameters (transverse resistance, target depth, sea depth, background resistivity, frequency).

In figure 3.10 and 3.11, mean response values (V) regarding varying TR and burial depth combinations are sketched for an acceptable CSEM scenario where airwave is present, and in case airwave phenomena is mitigated significantly by setting the sea depth to 4000m, respectively.

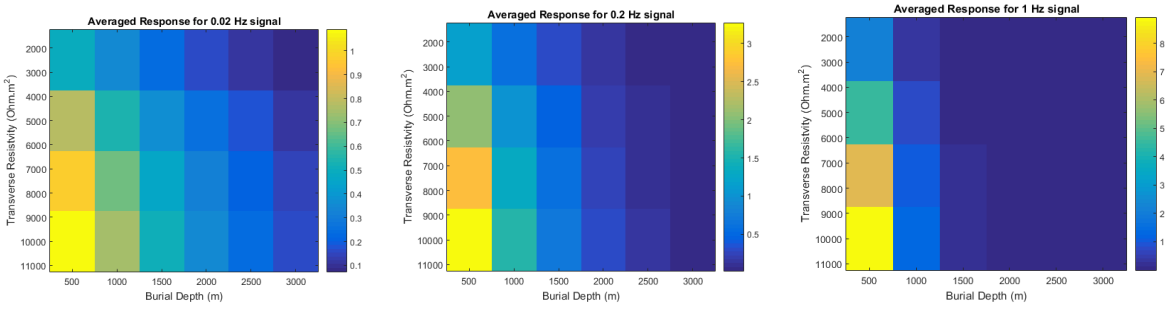

(a) (b) (c)

FIGURE 3.10: *NAR behaviours concerning varying TR and burial depth for 500m sea; (a) for f=0.02 Hz, (b) for f=0.2 Hz, (c) for f=1 Hz*

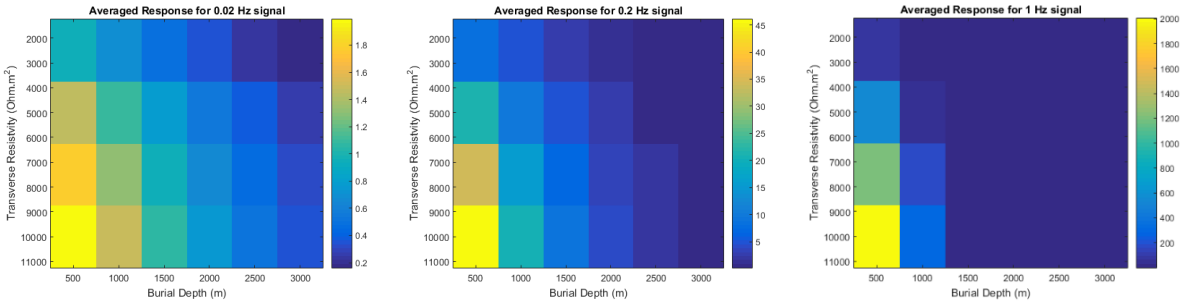

(a) (b) (c)

FIGURE 3.11: *NAR behaviours concerning varying TR and burial depth for 4000m sea; (a) for f=0.02 Hz, (b) for f=0.2 Hz, (c) for f=1 Hz*

As clearly seen, airwave has a strong impact in distingiushability. Normalized responses related to data blocks of weak airwave case (3.11) are far more strong than their equivalents for the case where airwave is serious (3.10).

Note that all figures shown in this chapter does not include noise. Hence, given sensing abilities can be seen as upper limits.

Seemingly, sensibility is proportional to transverse resistance and inversely proportional to target depth, as expected. However, proportionality to frequency is not that easy to predict, due to attenuator behaviour of diffusive, conductive media. [3] states that a 0.15-0.2 anomaly is ususally regarded as sensing limit and [11] indicates that anomaly strength about 0.3 can be considered good and above is excellent.

Releasing target depth and fixing all the other parameters, figure 3.12 gives another aspect; a visual behaviour as far as logarithmic electric field behaviour versus offset is concerned. The same for TR is processed in figure 3.15. Following two figures are subsets of data acquired by the case given in figure 3.10 and figure 3.11.

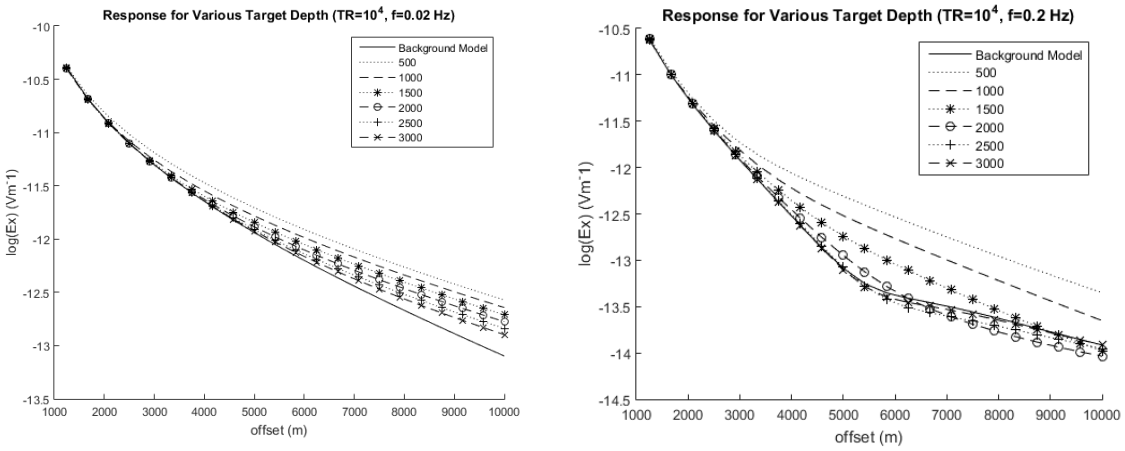

(a) (b)

FIGURE 3.12: *MVO for varying burial depths taken from the same data which produced 3.10 and 3.11 for 500m sea depth; (a) for 0.02 Hz, (b) for 0.2 Hz*

As expected for TR fixed, response seperation decreases with increasing burial depth. Moreover, for intermediate parameters (reasonable target depths and TR), sensing ability seems to be greater in latter case (figure 3.12.b), which issues a bigger (10 times) frequency. Yet, for very deep targets, higher frequency (0.2 Hz) obviously becomes inefficient due to rapid attenuation. Observed signal is not resolvable for depths 2500 and 3000m. Notice that the increase in frequency, in figure 3.12b and 10b, also shifts airwave effect earlier. Increasing frequency obviously causes the signal through water attenuate rapidly, however, an earlier domination in the presence of higher frequency signal is not an intuitive fact, because increasing frequency causes the signal through sub-seabed attenuate rapidly as well.

The discussion, indeed, is supported by findings of Morris given in [17]. Figures 3.13 and 3.14 are drawn for 2 frequencies: 1 and 0.1 Hz respectively. Coloured curves represent the inline electric fields (Ex) measuerd at related offsets (horizontal axis) in case of no airwave (infinitely deep water) for various background resistivities and dashed lines show airwave magnitude for various water depths. Intersection points are where airwave starts to dominate.

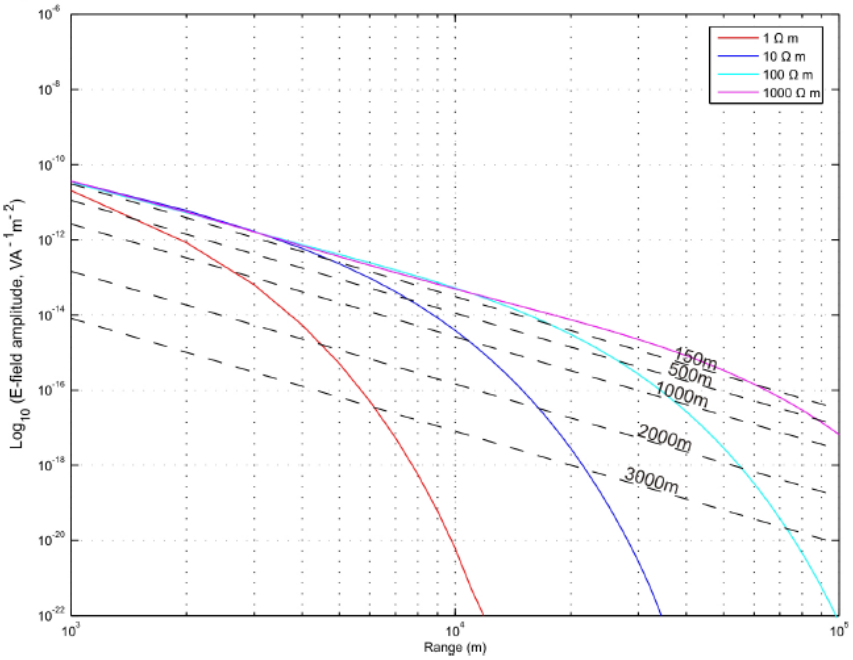

FIGURE 3.13: *Airwave behaviour for several sea depths and background resistivities for 1 Hz signal* [17]

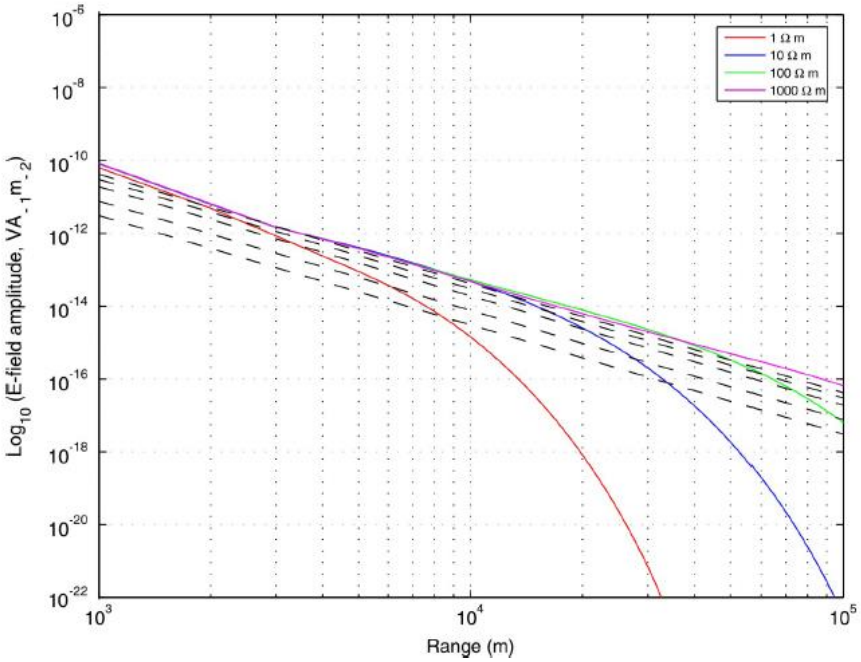

FIGURE 3.14: *Airwave behaviour for several sea depths and background resistivities for 0.1 Hz signal* [17]

As clearly seen, for smaller frequency, airwave dominates at further offsets comparing higher one.

On the other hand, consistently with figure 3.10, increasing TR, which is the main actor in CSEM method, ensures better resolution. Notice that for given set of parameters figure 3.15 includes no blind points. Indeed, all targets that exhibit TR more than 2500 Ohm.m^2, will be detected.

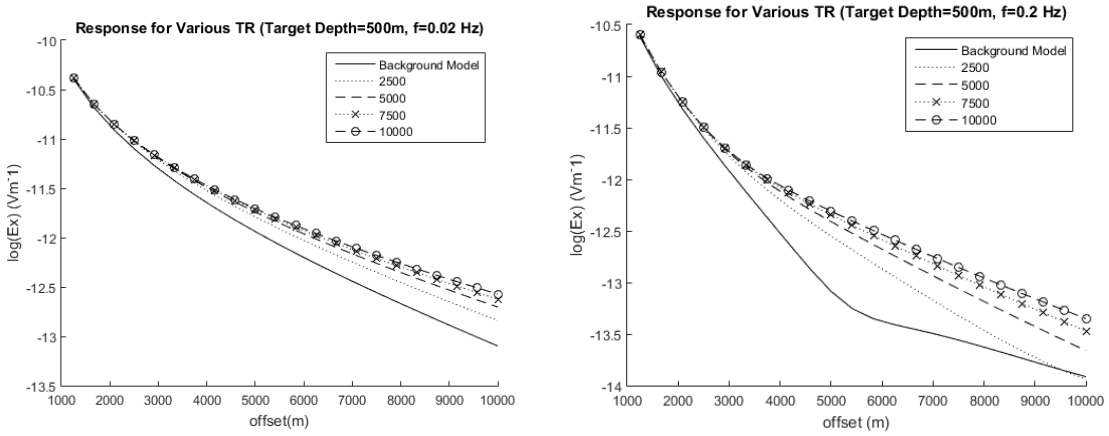

(a) (b)

FIGURE 3.15: *MVO for varying TR taken from the same data which produced 3.10 and 3.11 for 500m sea depth; (a) for 0.02 Hz, (b) for 0.2 Hz*

Speaking of which, considering average normalized response 0.2 as a sensing limitation, infinite set of parameters can be found to satisfy this condition (sensibility boundary). A few can be given as:

* TR = 5 x 10^4 Ohm.m^2, Target Depth = 2500m, f = 0.2 Hz, Sea Depth = 500m

* TR = 1000 Ohm.m^2, Target Depth = 2000m, f = 0.2 Hz, Sea Depth = 500m

* TR = 500 Ohm.m^2, Target Depth = 1500m, f = 0.2 Hz, Sea Depth = 500m

Under these conditions, not average normalized response but even the maximum normalized response remains below 0.2, sensing limit. Remark that, linearly increasing target depth requires an exponentially increasing TR, to stay at the same ability to get sensed. Regarding sensitivity, as can be seen in figure 3.16b canonically, [3] provides a compact graph, where resolution is worked in the presence of one varying parameter: TR.

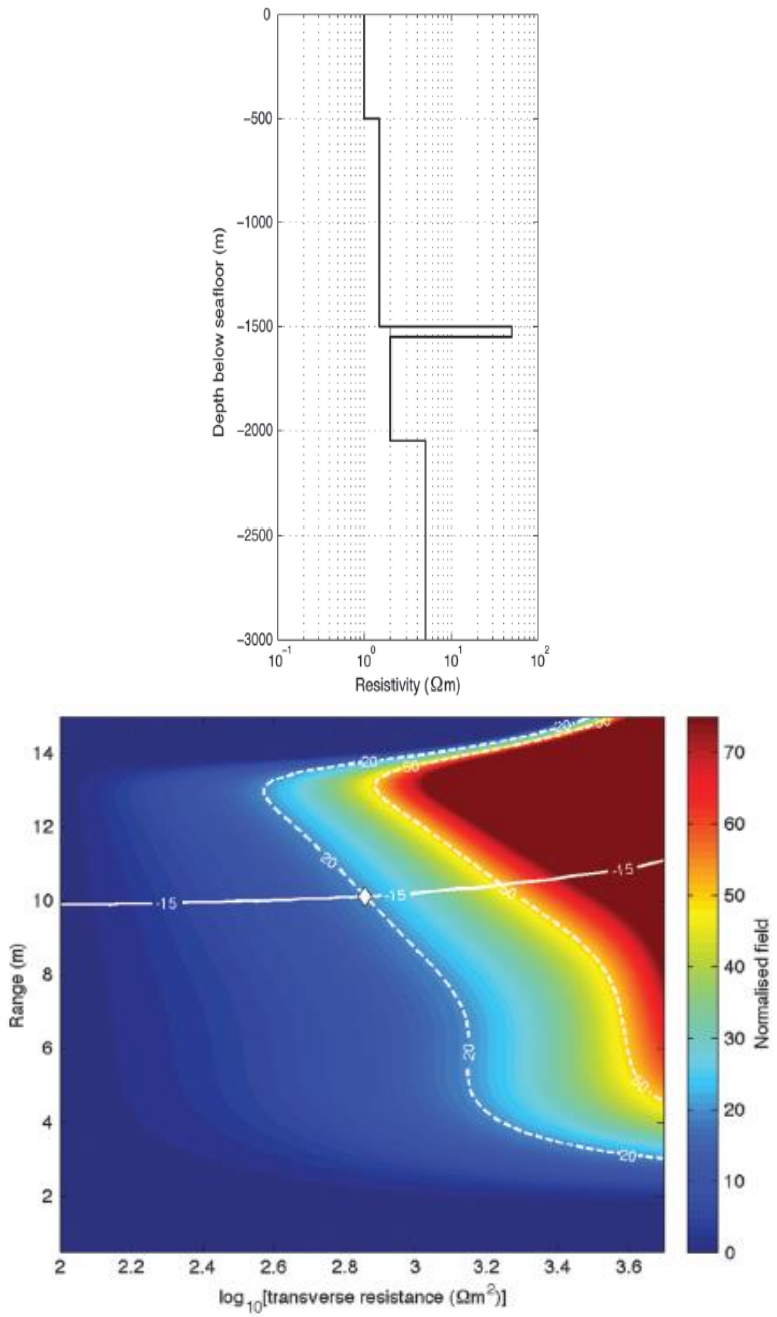

FIGURE 3.16: *Canonical representation of model with 1500m sea depth, 1500m target depth for 0.3 Hz frequency and 5.5km offset with related background estimation, (canonical plot), white line represents the noise floor* [3]

Here, sensitivity behaviour can thoroughly be seen. Any point (related to one specific receiver) that remains below the noise level and provides greater inline normalized field than 0.2, is basically sensible. Considering the normalized response regarding one specific receiver offset and noise level, the point marked with diamond, the minimum TR is stated to be 720 Ohm.m^2 that the system is sensitive to.

Untill now, horizontal inline component of electric field (Ex) radiated from horizontally located (x direction) HED in three dimensional cartesian coordinate system is considered. As far as perpenicular component (Ez) is concerned, interesting behaviours can be encountered. [17] provides Ex and Ez behaviours belong to one certain receiver located in 4km offset in a model in which a burial layer is present 1 km below the sub-seabed as depicted in figure 3.17. Here, dashed lines represent measured fields for a constant TR and continuous curves are measured fields for varying resistive layer thickness of the resistivity 75 Ohm.m.

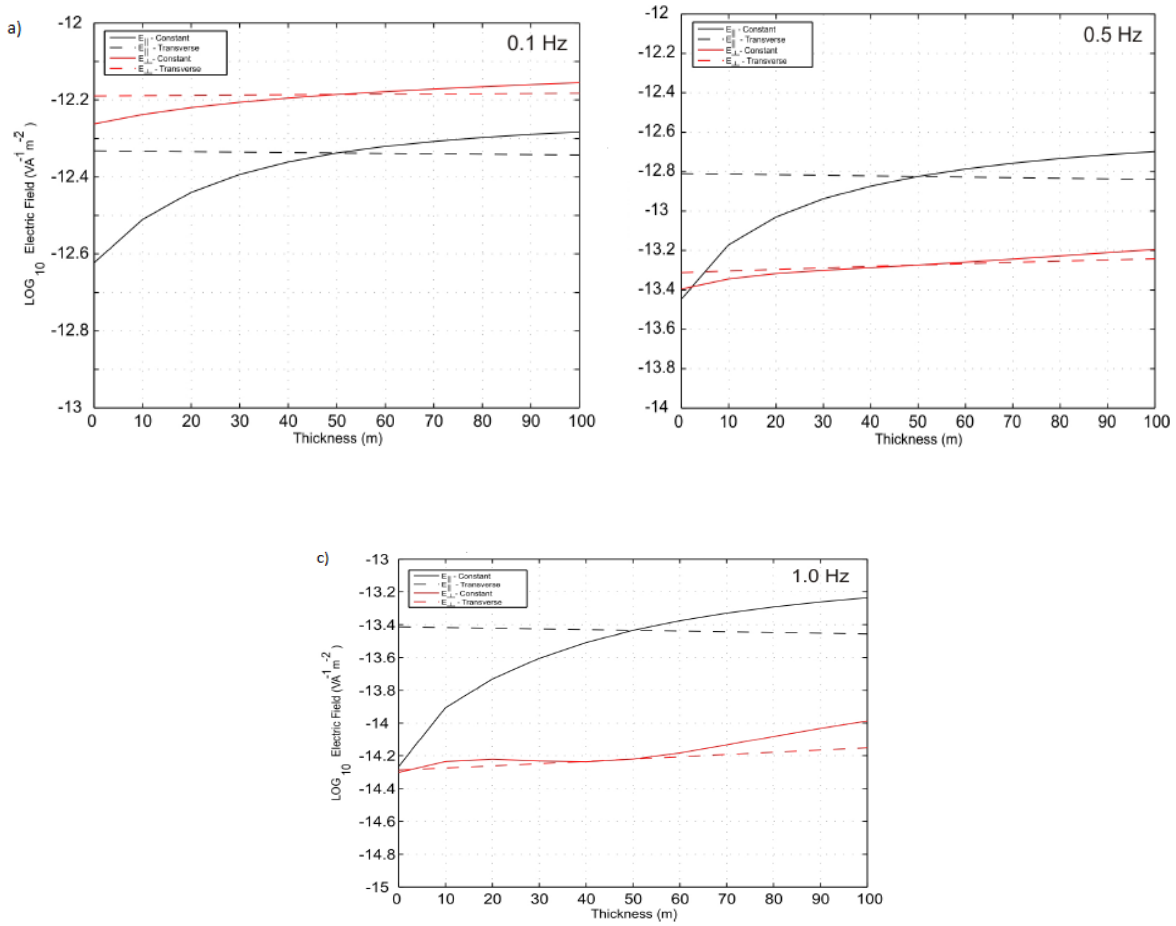

FIGURE 3.17: *Ex (black curves) and Ez (red curves) at a specific offset of 4km for frequencies; (a) 0.1 Hz, (b) 0.5 Hz, (c) 1 Hz. The solid lines show the electic fields for a 75 Ohm.m resistive layer of varying thickness, buried at 1km below the sea floor. The dashed lines show the electric fields for a layer with a constant TR of 3750 Ohm.m*^{2} [17]

Whereas consistently with previous discussion horizontal (parallel) fields exhibits negligible response to various combinations of the same TR, interestingly, perpendicular component behaves sensitively to thickness as frequency increases for a constant TR.

3.4.2 Non-conventional csem

Up to now, conventional CSEM schemes have been studied. In this subsection i would like to give basic insights regarding sensitivity conditions of alternative systems depicted in figures 1.13 and 1.15 where, unlike conventional one, receiver array is towed after transmitter or at least at the same altitude. In this chapter, this transmitter-receiver line will be called “streamer”, and its altitude from the sea floor will be denoted as “streamer height” or “streamer altitude”. In this section, two types just mentioned will be investigated further. First version suggests offsets as short as one thousand meters and aims shallower targets, however, the latter case does not compromise offset length, thus, emerges a challenging competitor against conventional schemes. Indeed, there are companies which operated that kind of CSEM reading and results are said to be pretty good.

3.4.2.1 Short Offsets

In this section, performance analysis for short offset CSEM scenarios has been investigated. As can be seen in literature [9], short offset CSEM systems are suggested to be implemented particularly for detecting shallow hydrate concentrations buried up to few hundred meters below sea floor. Indeed, deeper targets can not be subject to short offset CSEM surveys, since high frequencies must be used for having results in earlier offsets. Another expectations could be that, for very high frequencies are needed to be implemented, surface towed scenarios exhibits profound inefficiency due to strong attenuation in water. In this section, offsets up to 1000m will be considered for system analysis. Besides, target depths and sea depths up to 500m is implemented for frequencies 2Hz, 6Hz, 10Hz, 14Hz. Target resistivity and thickness are chosen to be as large as 100 Ohm.m and 100m, respectively, to provide best limit situations.

Initially, it is wise to see the set of system parameters that short offset CSEM scenarios won’t work at all. To begin with, it is useful to see figure 3.18

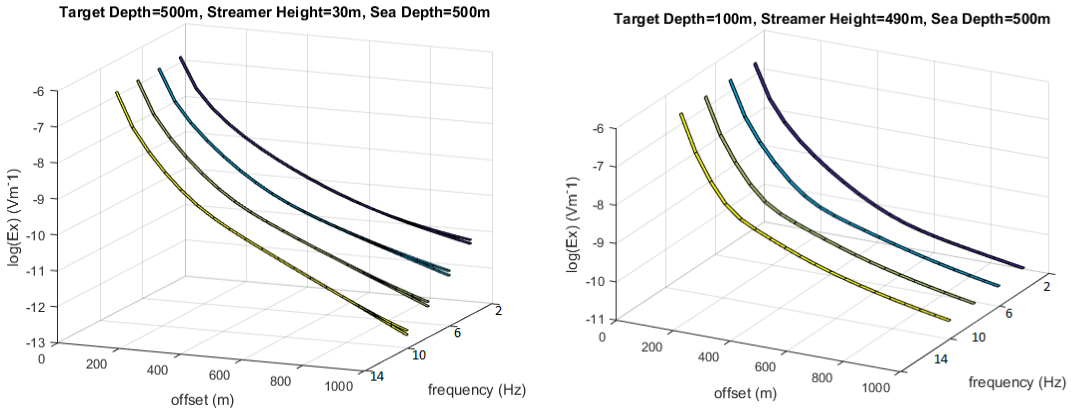

(a) (b)

FIGURE 3.18: *Short offset-towed CSEM off-limits for several system parameters; (a) for target depth of 500m and streamer altitude of 30m, (b) for target depth of 500m and streamer altitude of 30m for various frequency in both cases*

Figure 3.18a indicates that even in the case of a deep towed streamer, which suffers less from brine attenuation and sends more energy to earth, targets buried 500m deep or more is not detctable for a wide set of frequencies. Even this one basic observation is enough to state that in short offset streamer CSEM concept, targets deeper than 500m should not be expected to be detected. On the other hand figure 3.18b states that, in case of surface towed streamer, even targets buried around 100m below the floor, can not be resolved. This leads to the claim that short offset CSEM surveys must concentrat0 one deep towed streamers and must aim targets buried no more than 500m below the sea bed. Following results will focus on moderate parametric settings between the cases depicted in figure 3.4.2.1.

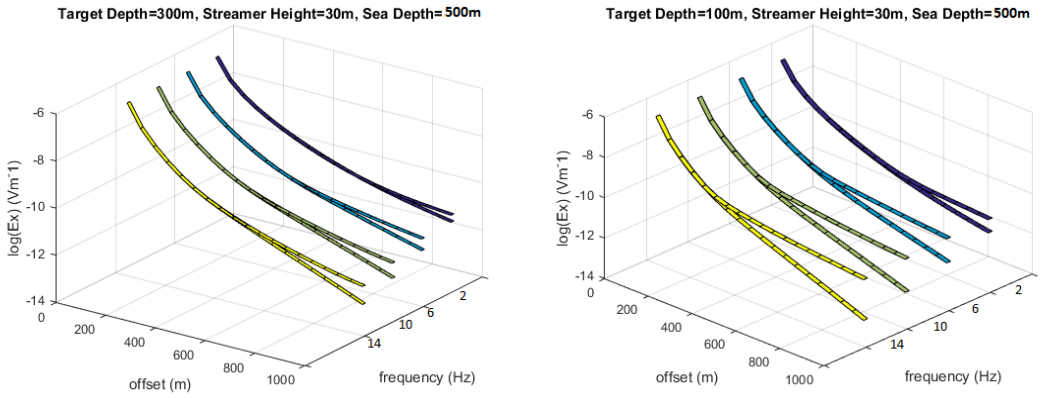

(a) (b)

FIGURE 3.19: *Short offset CSEM responses on various frequencies; (a) for 300m target depth, (b) for 100m target depth, where streamer height is 30m and sea depth is 500m for both models*

Model depicted in figure 3.19a concerns a shallower target (300m) with respect to the case given in figure 3.18.a. In this case, it is clear that a shallower target (all the other parameters are the same) begins promising fine results for offsets as late as 900m. Moreover, when figure 3.19.b and 3.18.b are compared, for the case concerning deeper towed one, surveyor is capable of detecting it, for all frequencies. Notice that even frequencies as large as 14 Hz give finest results for shallow target-deep towed scenarios. On the other hand, cases related to figure 3.19a and b are comparisonal in between. With all the other parameters are the same, of course, shallower target gives better results (b).

On the other hand, if a shallow target is concerned, gathered results are shown in figure 3.20. For two possible streamer altitudes each, figure 3.20a and 3.4.12.1.3.b present scenarios where the target depth is 100m, and sea depth is 100m and 300m, respectively.

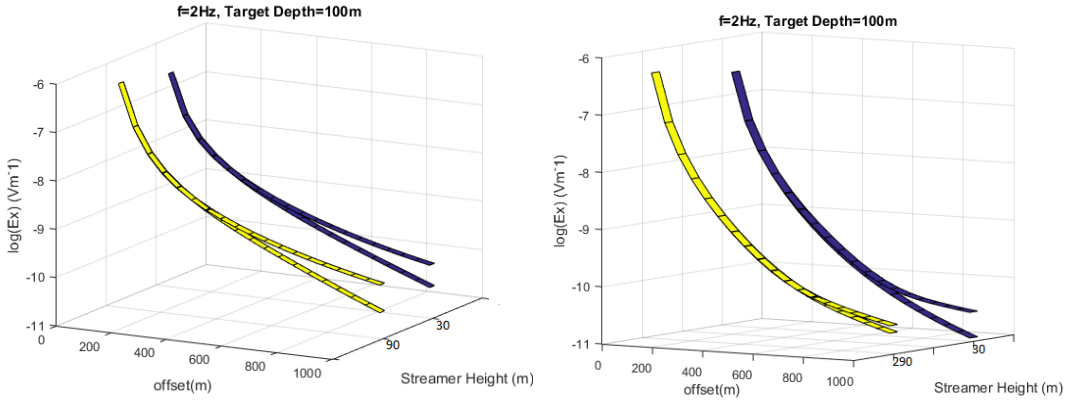

(a) (b)

FIGURE 3.20: *Short offset CSEM performance for varying streamer height for 2Hz frequency, 100m target depth and; (a) sea depth of 100m, (b) sea depth of 300m*

Situation clarifies that, for even very shallow target, sensitivity diminishes dramatically as streamer altitude gets closer to the surface. It is easy to predict that for 500m sea depth, a streamer close to surface won't provide any good results, either. However, for that case (500m sea depth), it can be shown that for parameters just employed, deep towed streamer provides detection (for simplicity, not included).

Now for the frequency 2Hz again, to see the effect of a deeper target, figure 3.21 is given.

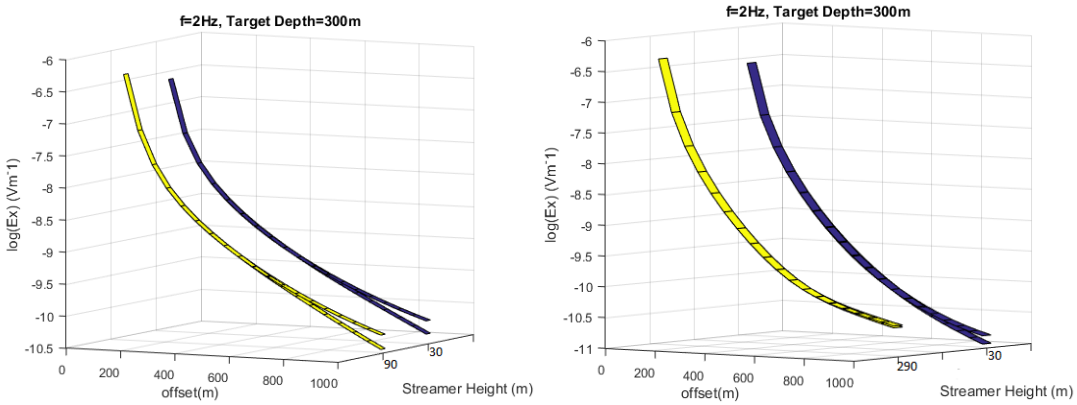

(a) (b)

FIGURE 3.21: *Short offset CSEM performance for varying streamer height for 2Hz frequency, 300m target detph and; (a) sea depth of 100m, (b) sea depth of 300m*

Clearly a serious impact is present. For 300m deep sea, it is not very difficult to claim that there is no reasonable detection for any streamer height employed. And for 100m deep water, only late offsets promise poor results.

In order to see the effect of frequency, figure 3.22 is prepared. Related plots (a) and (b) must be compared to 3.21.b. It is, indeed, interesting to observe that for a 300m target depth and 300m deep sea, increasing frequency provides better sensitivity for deep towed system. However, surface towed cases both in figures 3.22.a and 3.22.b, suffer too much from brine attenuation, thus, ensures no detection capability.

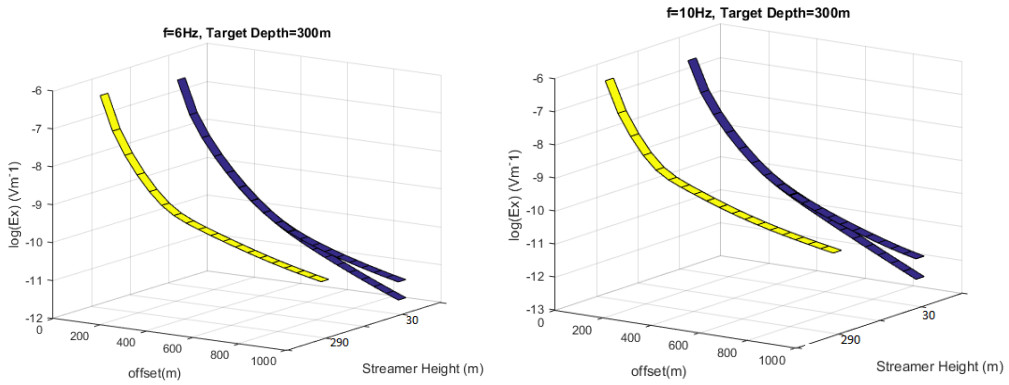

(a) (b)

FIGURE 3.22: *Short offset CSEM performance for 300m target and 300m sea depth for varying streamer height for; (a) 6 Hz (b) 10 Hz frequencies*

On the other hand, it is interesting to observe that, as depicted in 3.23.a, comparing with 3.22.a, a possible decrease in sea level supports a performance improvement on surface towed case, while it diminishes the performance of deep towed one. This is due to a stronger airwave effect that damages the data related to deep towed streamer case. However, a decrease in sea depth effects surface towed case positively, because it now suffers less from brine attenuation and conveys more energy through the subsurface.

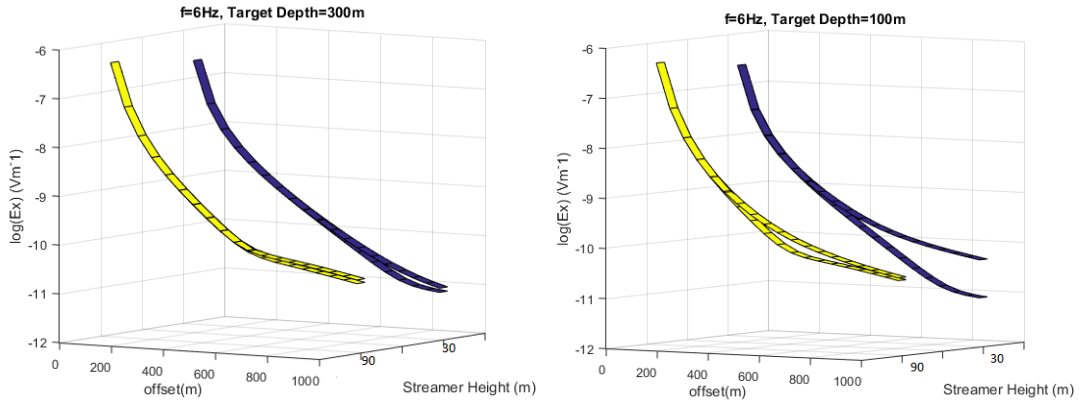

(a) (b)

FIGURE 3.23: *Short offset CSEM performance for model parameters 6 Hz, 100m sea depth; (a) 300m target depth, (b) 100m target depth for varying streamer height*

Yet, as far as shallower target is concerned with all the same other parameters with the case given in 3.23.a, results given in 3.23.b are reached. Here, a slight detection is possible for surface towed streamer case. On the other hand, tremendous detection capability is achieved for deep towed streamer scenario.

Comparing with 3.23.b, a deeper water scenario would prevent surface towed system from detection, however increases the performance for deep towed one as shown in 3.24.a, because of reducing the effect of airwave in latter case. This plot (3.24.a) is also comparable with 3.22.a. Case represented in 3.24.a provides better detection capability, of course, for a shallower target involved. 6d is comparable with 3.20.b as well. Rather than the case given in 3.24.b, scenario related to 3.20.b is able to provide a better surface towed system performance, due to greater coupling with earth (less water fading for less frequency). However, suffers from small frequency, as far as deep towed streamer case detection performance is concerned.

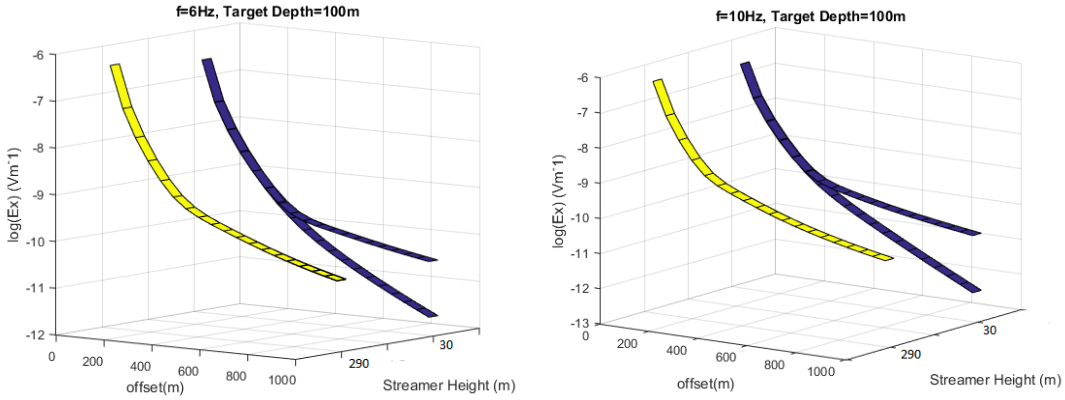

(a) (b)

FIGURE 3.24: *Short offset CSEM performance for model parameters, 100m target depth, 300m sea depth; (a) 6 Hz (b) 10 Hz for varying streamer height*

13.24.b introduces a frequency change into the system depicted in 3.24.a. In this case, new frequency is 10 Hz, sensitivity of surface towed streamer scenario is already gone. Besides, it is easy to claim that for deep towed streamer CSEM scenarios, as long as data remain above the noise threshold, anomalous cases are always detectable, given acurrate background information. Comparing 3.4.2.5.b case with the case related to 3.24.b, however, reveals an expected view, deeper the target, the more difficult to detect it.

The same parameters provided as in the case related to 3.22.b, except a higher frequency 14 Hz, 3.25.a shows the resulting data. Deep towed case again provides detection. Furthermore, if sea depth is increased to 500m, with respect to the scenario represented in 3.25.a, even greater result for deeper towed streamer CSEM system is present. This is due to previously discussed, mitigated airwave effect.

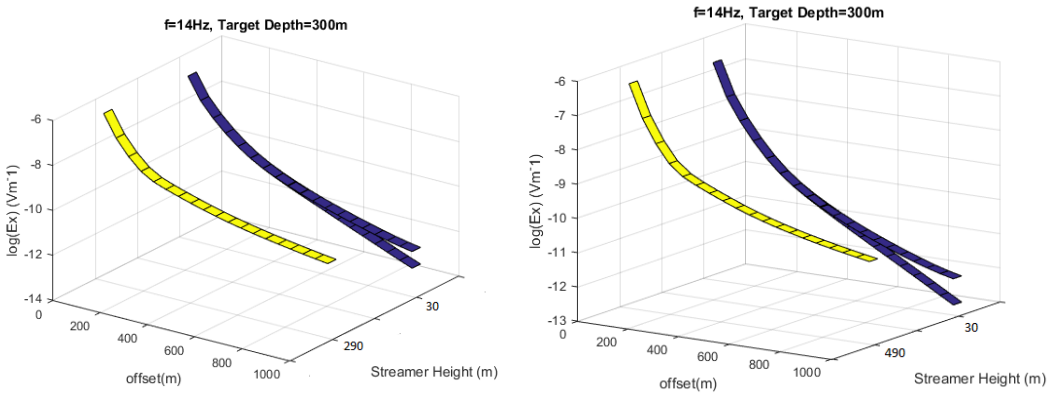

(a) (b)

FIGURE 3.25: *Short offset CSEM performance for model parameters, 300m target depth, 14 Hz frequency, sea depth of; (a) 300m (b) 500m for varying streamer height*

Following graphs are prepared to provide comparisonal tools from other perspectives. Figures 3.26.a and 3.26.b summarize the surface towed cases where frequencies 2Hz and 6Hz are used, respectively, for a sea depth of 300m. It is clear that, although it is the most operational case and main focus, surface towed cases do not promise much.

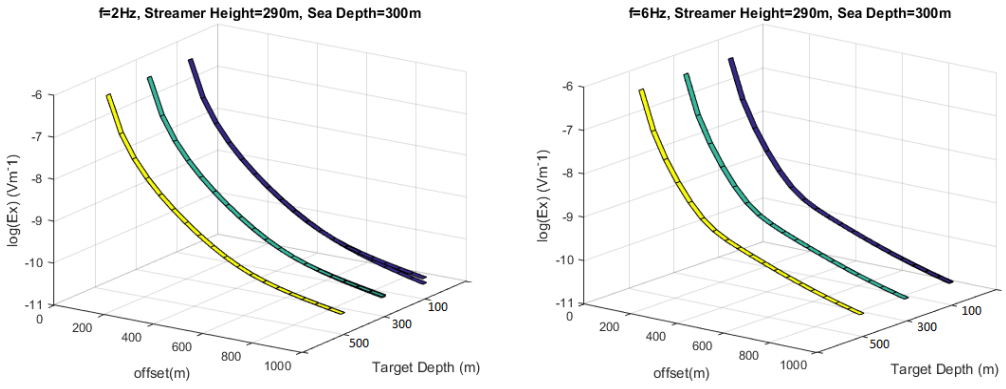

(a) (b)

FIGURE 3.26: *Short offset CSEM performance for model parameters, 290m streamer height in 300m sea; (a) 2 Hz, (b) 6 Hz frequencies for varying target depth*

However, if a water as shallow as 100m is present, then surface towed scenarios can be useful, as figures 3.27.a and 3.27.b indicate. In these cases, targets buried up to 300m below the floor can be seen. Yet, that case may not be success, because it is not very different to tow a streamer at 30m or 90m altitude in a 100m deep water.

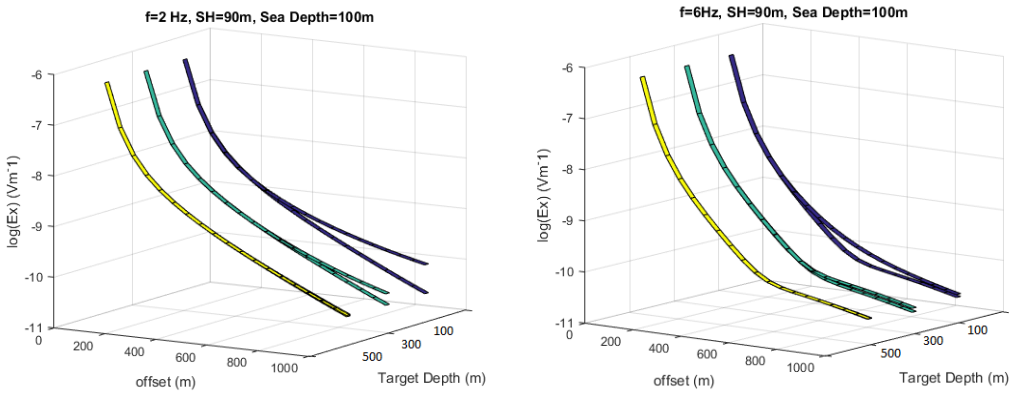

(a) (b)

FIGURE 3.27: *Short offset CSEM performance for model parameters, 90m streamer height (SH) in 100m sea; (a) 2 Hz, (b) 6 Hz frequencies for varying target depth*

Concisely, an alternative short offset towed streamer CSEM system will be able to detect targets buried only up to 500m below the floor and since very hih frequencies are needed to be employed, surface towed applications will not promise. However, if streamer altitude flexibility is present (especially in shallower water it is easy to provide it), by towing the streamer deeply, it is almost certain to detect any sufficiently large target up to 500m depths.

3.4.2.2 Long offsets

In this case, increasing frequency would cause greater losses, therefore poor performance, on the other hand, it is expected that increasing streamer height would bring on stronger airwave effect thus poor performance as well. However, it is worth bearing in mind that the bigger streamer height, the greater professional and operational advantages on the field. Thus, a challenge and a trade of balance seem to be present. Moreover, long offset CSEM applications are always more sensitive to low frequencies, in most cases the only way seeing deeper.

Intrinsically, alternative CSEM models that implement long offsets where transmitter and receivers are towed together, can be studied under three sub-topics as very shallow waters, shallow-moderate deep waters and deep waters. In this subsection, an offset length of 10km is used with 25 receivers equally distributed.

3.4.2.2.1 Shallow waters (200m)

Shallow water CSEM surveying draws serious attention in the literature, because there are considerabe number of prospects ([9], [1]) that lie below shallow waters. Thus, it is worth studying a section devoted to it.

To see the general features and limitations related to shallow water CSEM probing, a scenario where sea depth is set to 200m is configured with frequencies 0.125 Hz, 0.2 Hz, 1 Hz and 2 Hz. The scenario issues varying target depth and varying streamer altitude chosen as 30m, 105m and 180m above the sea floor. Besides, TR is chosen as 10000 Ohm.m^2 where target thickness is 100m for all the models in this sub section to provide an upper limit.

In this case, it can be shown that 2Hz data appears only in burial depths as shallow as 500m for smaller streamer altitudes as 30m and 105m. When taken into consideration that high frequencies will decay rapidly in water medium, this is expected. As far as shallow targets are concerned (500m) with high TR (10000 Ohm.m^2), it is observed that very high frequencies up to 15 Hz can be used for 30m streamer altitude. Since skin depth is very small in this case, both vertical and horizontal range is expected to be very limited [4]. It is also expected to see the target only for small streamer height (30m). In such high frequency case, field responses would be as shown in figure 3.28.

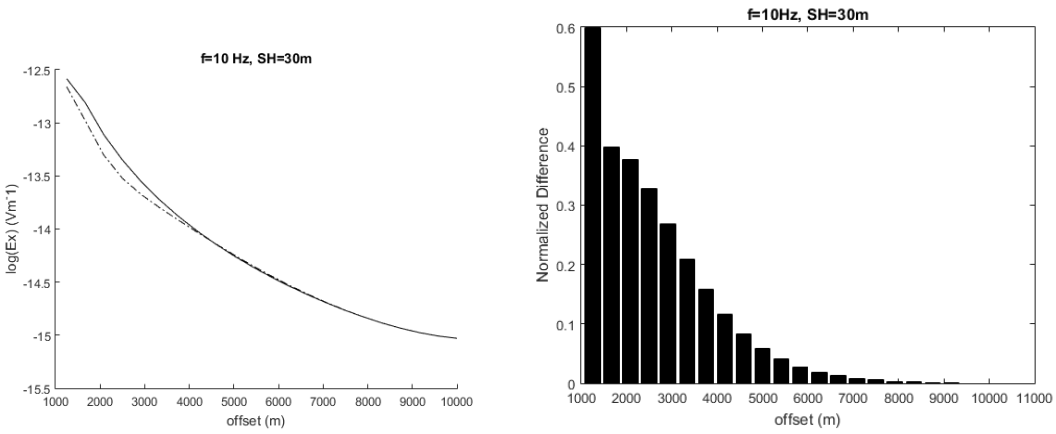

(a) (b)

FIGURE 3.28: *CSEM experiment for model parameters 200m water, 30m streamer altitude, 10 Hz frequency; (a) MVO, (b) Normalized amplitude response vs. offset*

Limited range in high frequency case, would allow only the offsets of first few thousand meters seem to have useful data, correspondingly cause stronger normalized field difference responses in earlier offsets which decays exponentially as indicated in figure 3.28.

As far as reasonable frequencies are concerned, results exhibited in following figures are gathered. For 1 Hz frequency, figure 3.29 shows that when the streamer is towed on the altiude of 30m from above the sea floor, targets up to 1000m depths are detectable.

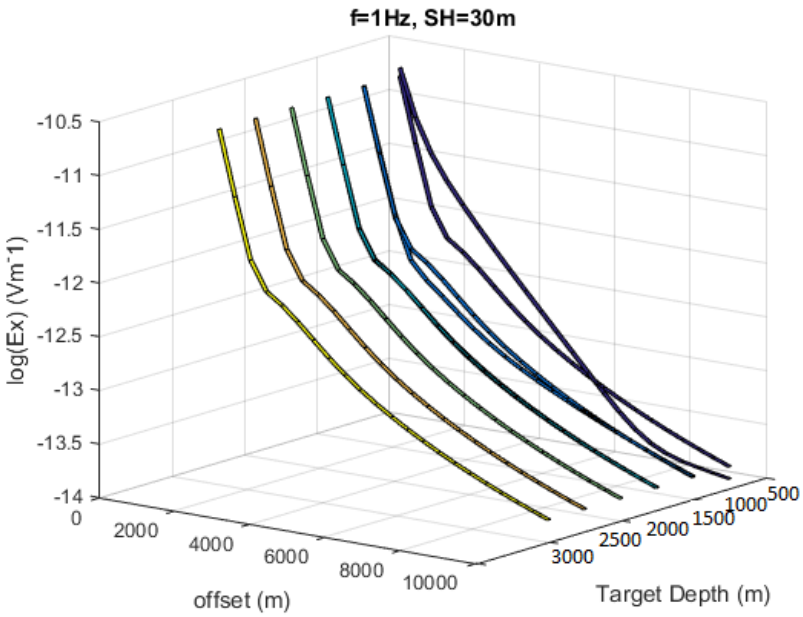

FIGURE 3.29: *CSEM responses for varying target depth for model parameters 1 Hz frequency, 30m streamer height, 200m sea depth*

However, as streamer altitude increases, distinguishability of the target on greater depth (1000m) vanishes Thus, figures 3.30 and 3.31 where the streamer height (SH) is set to 105m and 180m respectively, target is detectable only if it is around 500m below the floor.

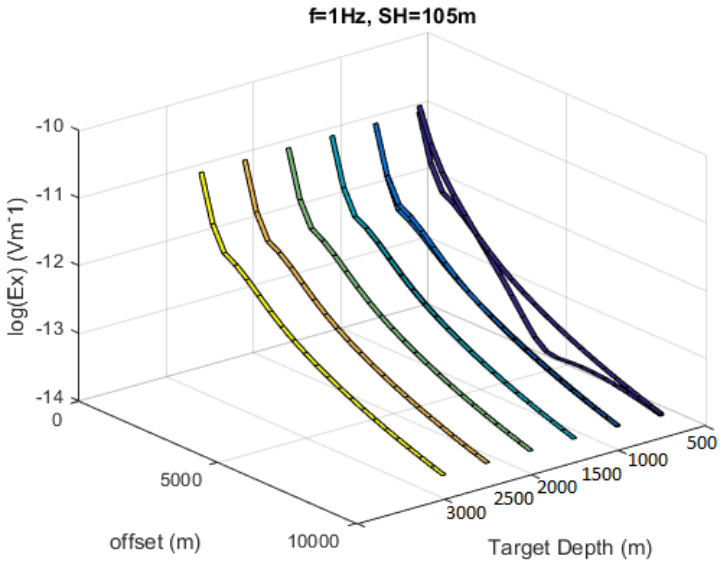

FIGURE 3.30: *CSEM responses for varying target depth for model parameters 1 Hz frequency, 105m streamer height, 200m sea depth*

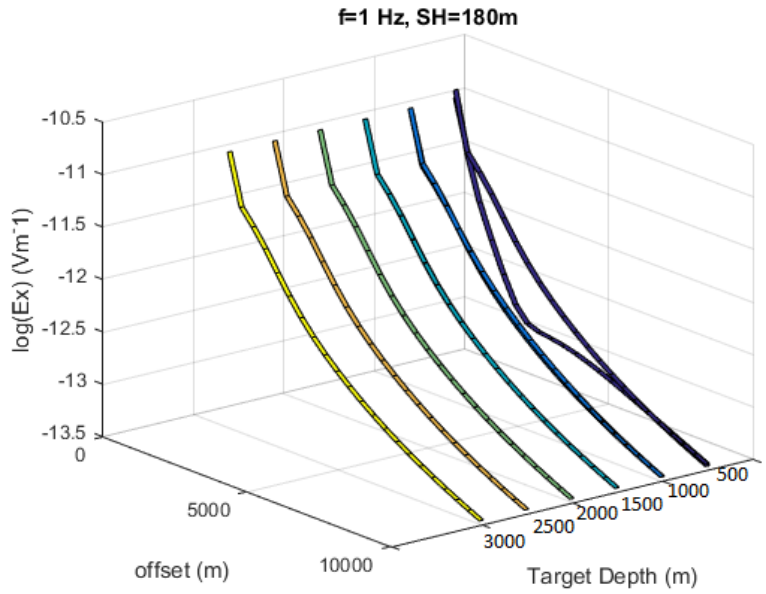

FIGURE 3.31: *CSEM responses for varying target depth for model parameters 1 Hz frequency, 180m streamer height, 200m sea depth*

In conclusion, associated to relatively high frequency, 1 Hz, targets buried deeper than 1000 m is never spotted. On the contrary, a lower frequency provides a different framework. Figures 3.32, 3.33, 3.34 show what happens if 0.125 Hz low frequency signal is implemented instead, for adopted streamer altitudes 30m, 105m and 180m from the floor respectively.

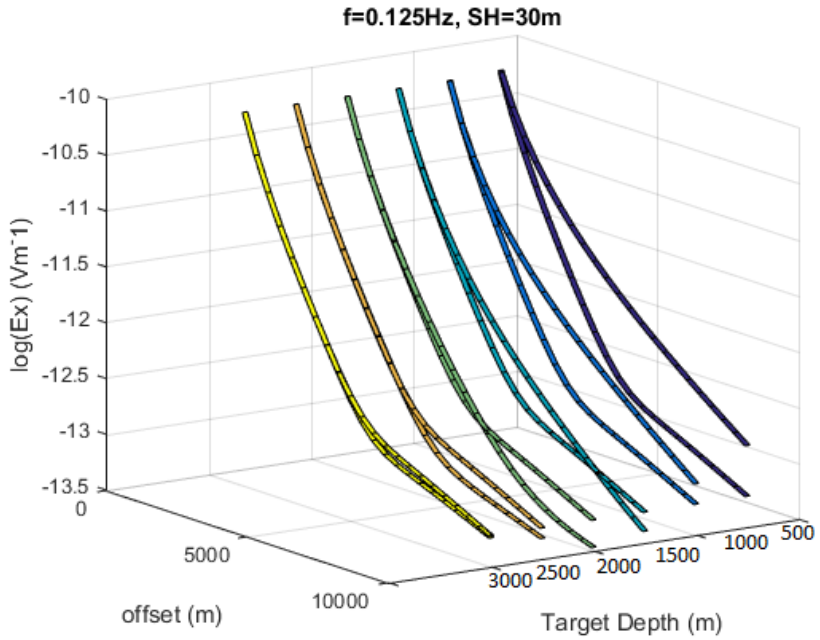

FIGURE 3.32: *CSEM responses for varying target depth for model parameters 0.125 Hz frequency, 30m streamer height, 200m sea depth*

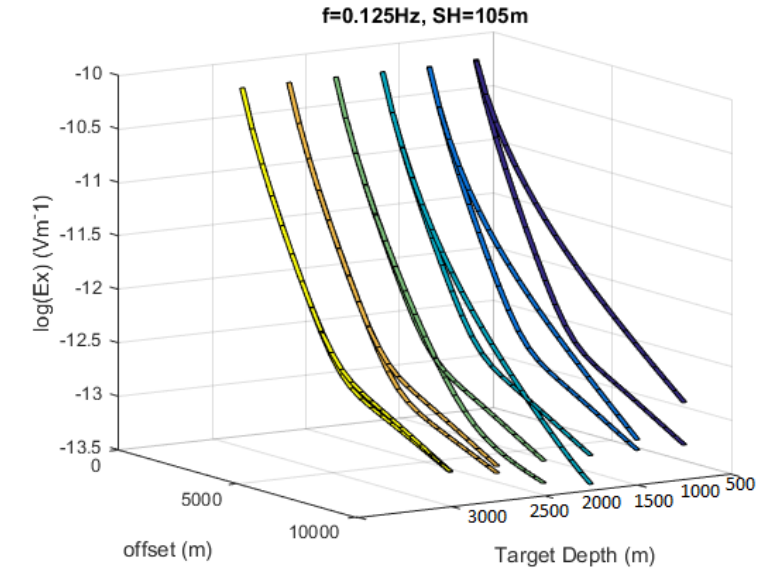

FIGURE 3.33: *CSEM responses for varying target depth for model parameters 0.125 Hz frequency, 105m streamer height, 200m sea depth*

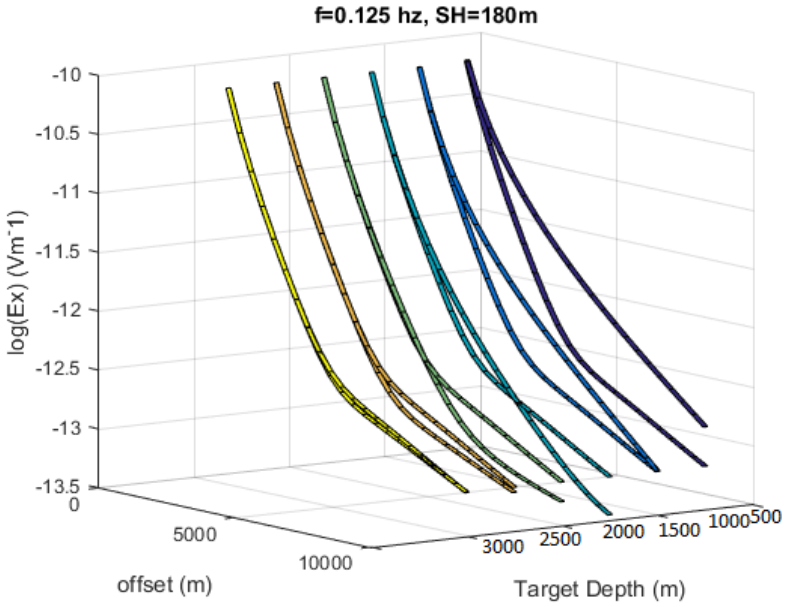

FIGURE 3.34: *CSEM responses for varying target depth for model parameters 0.125 Hz frequency, 180m streamer height, 200m sea depth*

Notice that, as frequency decreases, difference between models belong to different streamer altitudes diminishes. This observation is clearly supported by figure 3.35.

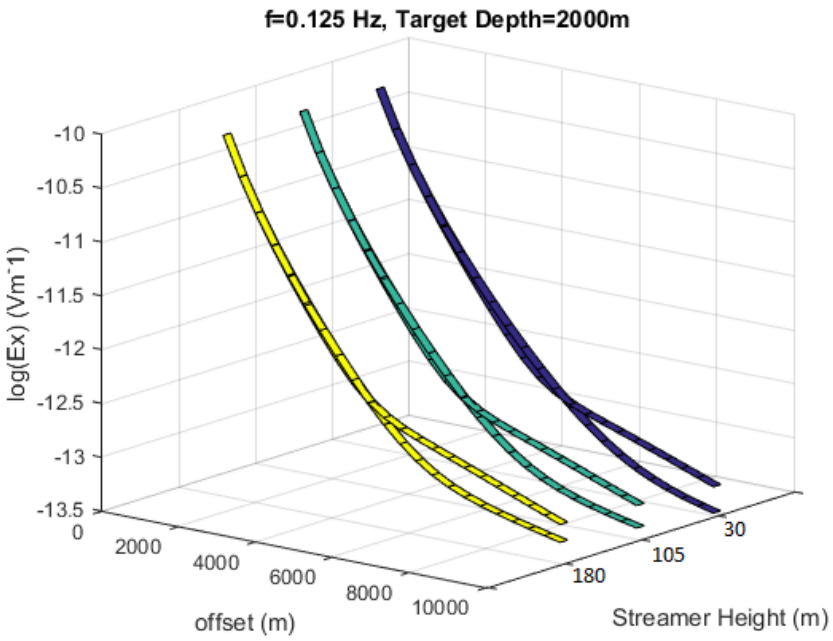

FIGURE 3.35: *CSEM responses for varying streamer height for model parameters 0.125 Hz frequency, 2000m target depth, 200m sea depth*

As previously mentioned, for deep waters, streamer height is important, deeper it is, better the results. However, figure 3.35 suggests that for waters as shallow as 200m, streamer altitude does not change the results too much. This is simply because reduced brine attenuation. Therfore, as expected, normalized field differences behaviour related to this case looks very similar to each other as shown in 3esa and 3esc, the graphs sketched for 30m and 180m streamer altitudes respectively.

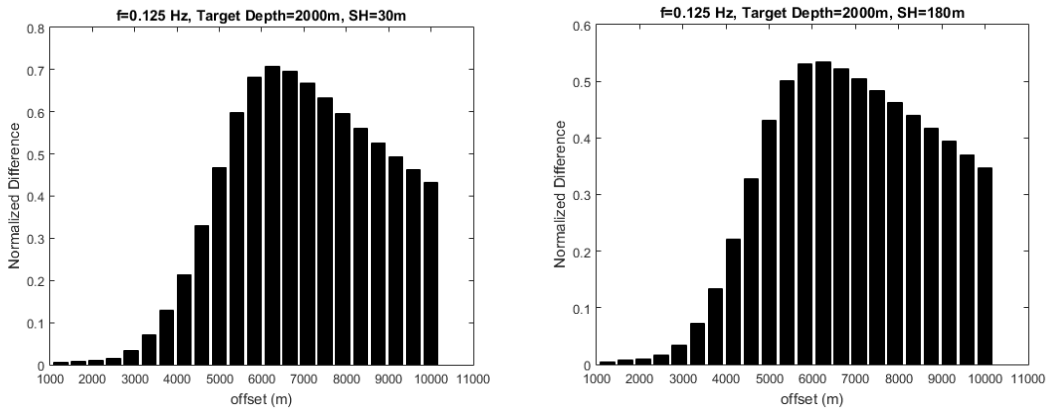

(a) (b)

FIGURE 3.36: *Normalized ampliude responses vs offset related to the case processed in figure 3.35 for (a) 180m, (b) 30m streamer altitudes*

Averages of two responses given in figures 3.36.a and 3.36.b are 0.3 and 0.37 respectively. As clearly seen there is no considerable difference. This view immediately promotes the idea that there might be no need for deploying the receivers on the bottom, at all.

From another aspect, [1] claims that the configuration with ocean floor deployed receivers with deep towed transmitter (30m above) and ocean floor deployed receivers with surface towed streamer (10m deep) also give almost the same results for very shallow waters as deep as 100-200m. In figure 3.37, they represent the results that support their statement.

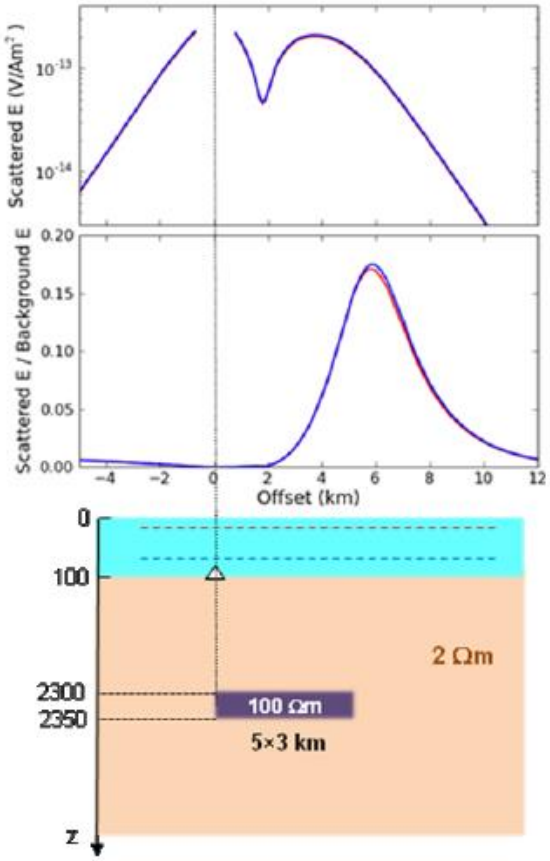

FIGURE 3.37: *CSEM field responses of surface towed transmitter (red curves) and deep towed transmitter (blue curves) for ocean floor deployed receivers in both cases* [1]

However, i prefer to go one step further and compare base deployed receiver conventional CSEM scenario with surface towed streamer alternative CSEM approach. To clarify this query, a fair comparison must be given between fixed receiver case (not 30m altitude), and towed streamer case, preferentially towed close to sea surface. Figure 3.38 provides such a comparison between conventional CSEM case where receievers are located on the ocean floor and transmitter is towed 30m above it, and newly introduced CSEM concept where streamer, which carries transmitter and receivers together, towed 20m below the sea

surface in the presence of 200m deep water. Notice that, in terms of offset vs recorded field amplitude, there is no a remarkable distinction.

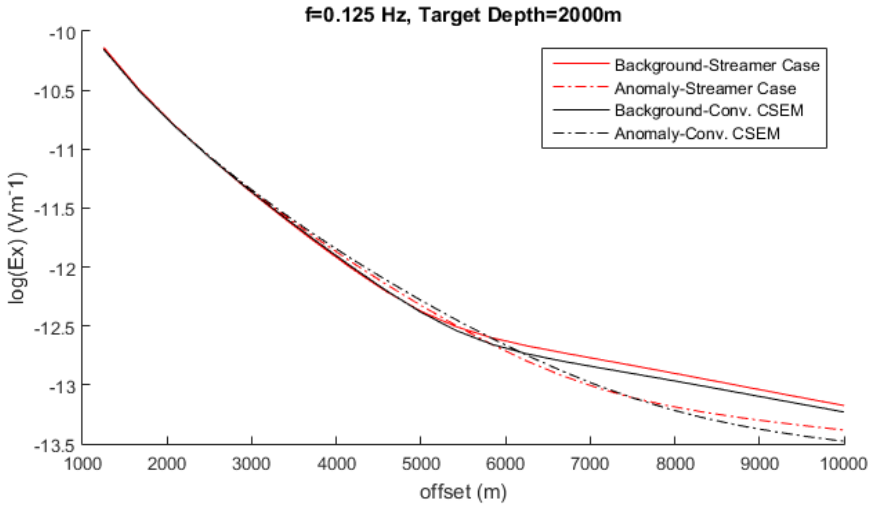

FIGURE 3.38: *Comparison of CSEM concepts: fixed receivers vs surface towed streamer for model parameters 0.125 Hz frequency and 2000m target depth.*

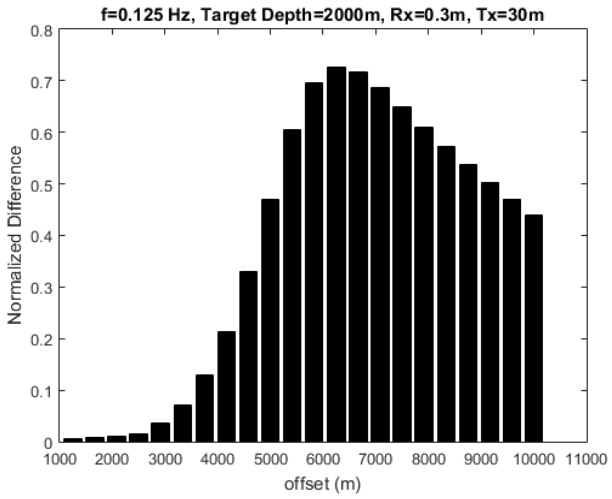

FIGURE 3.39: *Normalized amplitude response vs offset for fixed receiver case*

Figure 3.39 depicts the normalized field difference related to conventional CSEM case which is shown with black curves in figure 3.38 and it is given for the purpose of supplying a quantitative comparing ability. In conventional case, normalized field difference tuns out to be 0.38. This ensures a small improvement up to 25% with respect to 180m high towed streamer case. Furthermore, in this scenario it is observed that whilst target detection range is around 2900m for conventional CSEM, it is around 2750m for 180m high towed

streamer CSEM case. That seems to remove the need for fixed receiver deployment. In the light of this discussion, i suggest that for very shallow waters it is operationally more convenient to use a towed streamer alternative, instead of a classical CSEM fixed receiver concept.

On the other hand, very shallow water introduce well known air wave problem, thus care must be taken.

3.4.2.2.2 Moderately Shallow Waters (550m)

To have a basic idea on the impact of itroducing varying streamer height, figure 3.40 can be seen for moderately deep waters. Here, model parameters are set to 50m thick, 1500m below buried target with 0.2 Hz probing frequency and 550m sea depth. Curves depict cases related to different towed stream heights from the floor. As expected, as streamer height goes upper and upper, distinguishability of the target from the background decreases. Whilst streaming as deep as 30m from floor provides the best performance as very similar to conventional cases, very high streaming scenario, 20m below the sea surface, provides the worst, whereas it is the economically valued one.

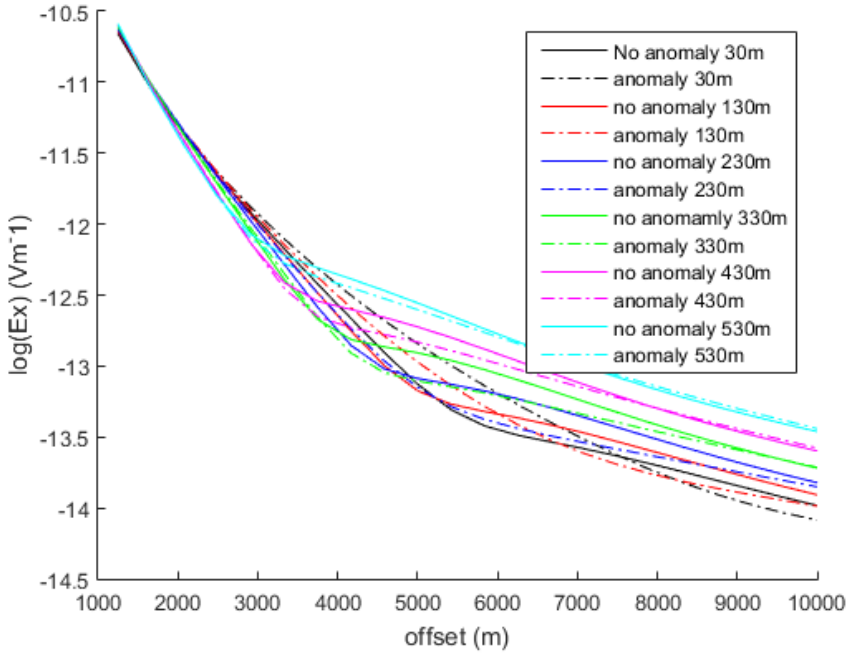

FIGURE 3.40: *Impact of streamer height for model parameters 5000 Ohm.m^2, 1500m deep target, 550m sea depth and 0.2 Hz frequency.*

Figure 3.41 provides a quantitative evaluation on the case related to figure 3.40. Supporting the previous graph, 430m height seems to be just around detection capabilities and the case where it is located 530m above the floor, is clearly difficult to detect, however in some cases possible.

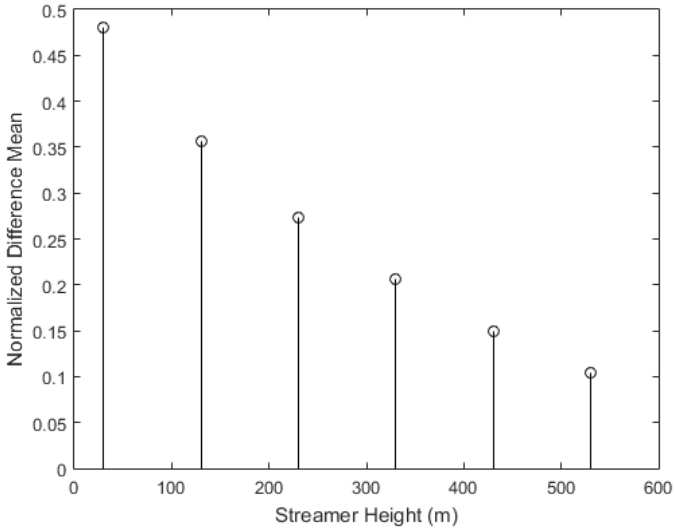

FIGURE 3.41: *Impact of streamer height in terms of mean normalized difference for the case represented in figure 3.40*

Figure 3.42 is prepared to give a reference insight to the reader. In figure 3.42, same target and frequency conditions as in the case related to the case given in figure 3.40 are implemented for comparison. Here, conventional CSEM where transmitter is located 30m above the floor and there are fixed receivers on the floor (30cm) is compared with the non convemtional case where transmitter-receiver streamer is located 30m above the floor. As clearly seen, there is no distinguishable difference. This graph is given for the purporse of supporting the idea that reader can use 30m-streamer height cases as “conventional CSEM” reference for related subsequent plots for comparisonal concerns. Comparison is done also in other parametric settings, therefore approach can be used safely.

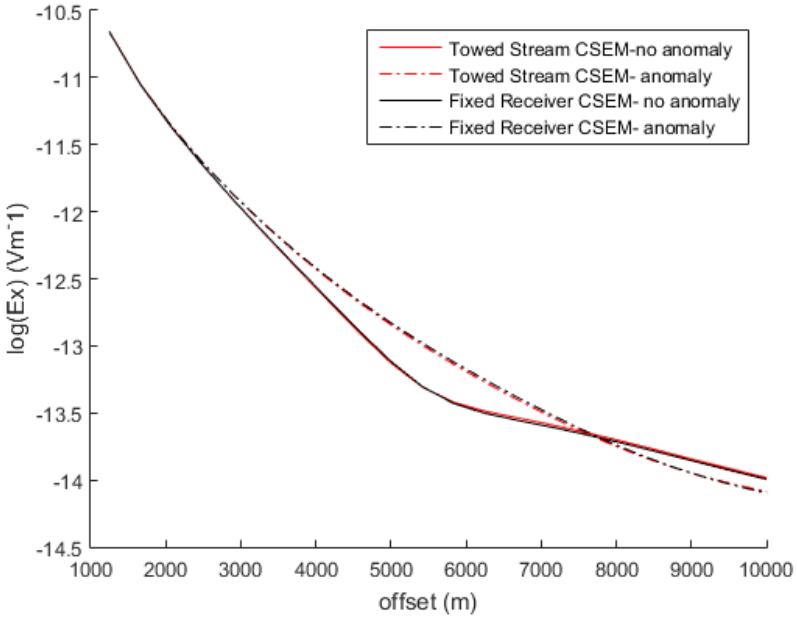

FIGURE 3.42: *Reference providing plot: for comparisonal reasons, conventional CSEM (fixed rx, 30m tx 30m above the floor) performance could be accepted as the same with 30m above towed streamer CSEM (rx,tx 30m above the floor)*

For a comprehensive investigation of long offset streamer CSEM referred in figure 1.15 a model which include 100 Ohm.m resistive target varying in thickness and burial depth is considered to be the issue of the experiment inwhich 5 harmocis (0.2, 0.4, 0.6, 0.8, 1) are used. Background resistivity is chosen to be 1 Ohm.m. In first focus, a realistic case that suggests a 550m deep water with streamer height varying between 30-530m is present. Due to computational reasons, step differences of varying parameters can not be chosen very small. Moreover, sensitivity amalysis conducted in this work rely on 1D electromagnetic propagation simulation and aims to give a qualitative and pragmatic argumentation capacity to the reader.

As far as the impact of varying frequency with specific reservoir thickness, burial depth and newly introduced variable: streamer height (above ocean floor) is concerned, following plots provide several perspectives. Figure 3.43 issues a thick target (100m) and a streamer towed above 330 m above seabed, or 220m below the sea surface. In figure 3.43.a, target depth is chosen to be 500m, and in this case, target is resolvable in all the frequencies. However, as figure 3.43.b suggests, if target depth were 1000m, only frequencies 0.2 Hz and 0.4 Hz would be able to resolve the target.

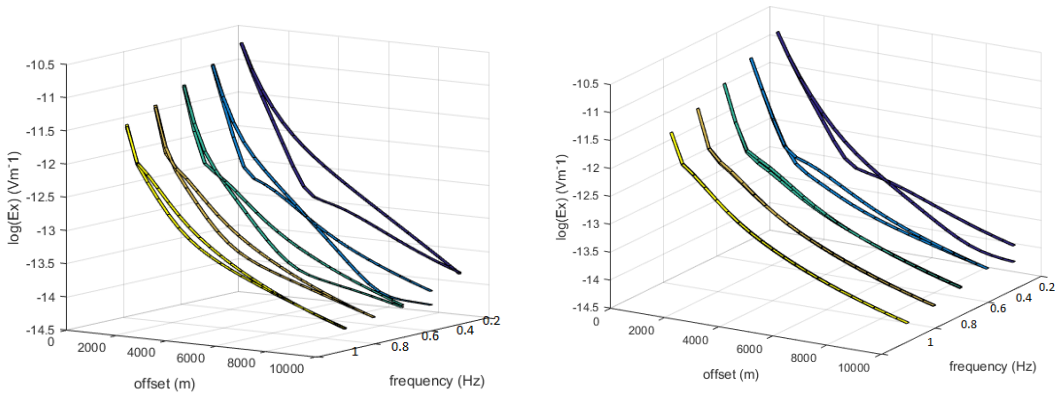

(a) (b)

FIGURE 3.43: *CSEM responses related to CSEM concepts with model parameters: 550m sea depth, 5000 Ohm.m^2, target which is buried (a) 500m, (b)1000m below the ocean floor*

Moreover, due to operational ease, streamer height can be introduced as big as possible rather than the one given in 3.43.a. Particularly, a streamer height of 530m, just 20m below the surface would provide results given in figure 3.44.a. In this case, model differs from the one given in figure 3.43.a only in streamer height. It is clear that for this model, frequencies that can be used to detect the target seem to be 0.2 Hz, 0.4 Hz. On the other hand if model depicted in figure 3.43 is modified on target depth to a new value of 1500m, it is now clear that only 0.2 Hz is able to see the reservoir as seen in figure 3.44.b.

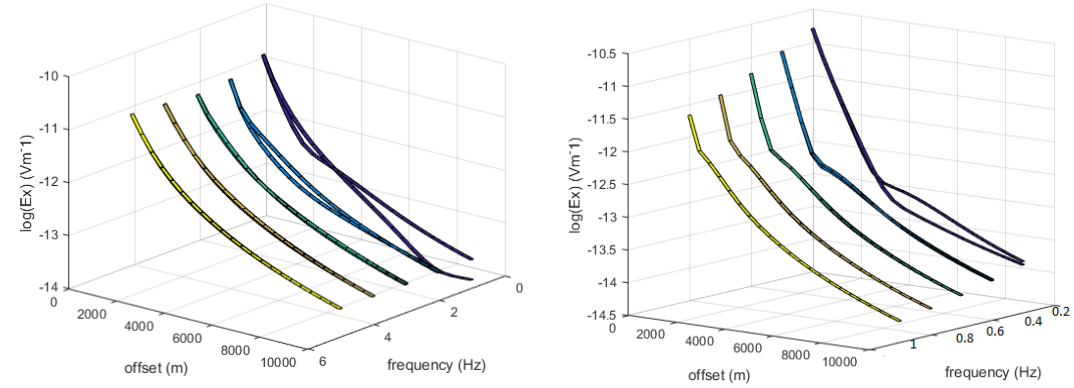

(a) (b)

FIGURE 3.44: *CSEM responses related to CSEM concepts with model parameters: (a) 530m streamer height and 5000 Ohm.m^2 500m deep target, (b) 330m streamer height and 1500m deep target in 550m deep sea*

For moderate settings implemented, models depicted in figure 3.45.a and b present edge conditions that at most 0.6 Hz can be used for detection. That means any improvement made in

target thickness, burial depth or streamer height, would lead to clear detection under when probing frequency is chosen to be 0.6 Hz or less. Figure 3.45.a and b also suggest smoother performance loss as frequency increases, while detection performance in precedent graph (figure 3.44) drops dramatically as frequency increases. In models given figure 3.45, 75m thick, 1500m below buried target with 130m streamer height and 75m thick, 1000m below buried target with streamer height of 230m are used, respectively.

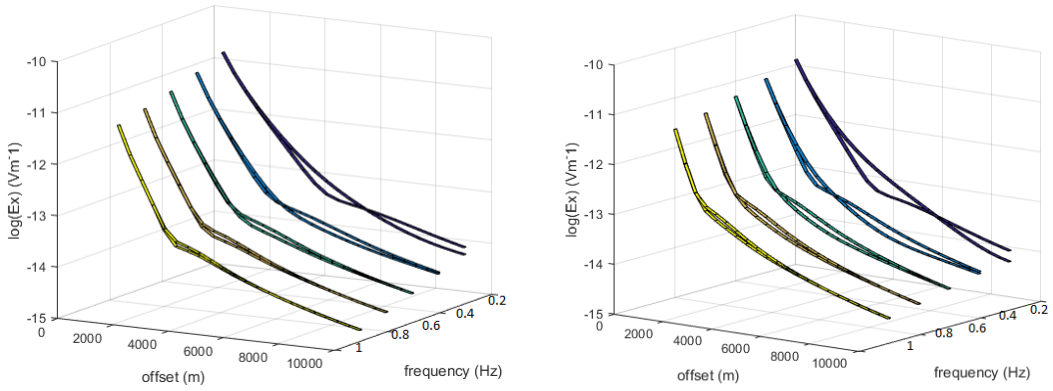

(a) (b)

FIGURE 3.45: *CSEM responses related to CSEM concepts with model parameters: (a) 130m streamer height and 7500 Ohm.m^2 1500m deep target, (b) 230m streamer height and 7500 Ohm.m^2 1500m deep target in 550m deep sea*

Figure 3.46.a suggests a model with a relatively thick resistive layer (100m) buried 1500m below the sub-seabed with a streamer height of 530m. Additionaly, figure 3.46.b introduces a thin resistive layer (25m) buried 1000m below with a streamer height of 530m as well. Both cases, where only 0.2 Hz probing frequency is slightly able to detect the target, exhibits similar peformance. Namely, when a streamer height of 530m is introduced, it is highly possible not to be able to resolve a target buried 1500m below the ocean floor in any frequency, unless its thickness is around 100m, which brings a TR in the order of 10000 Ohm.m^2, a considerably great value. Thus, figure 3.46.b focuses on a target buried 1000m below and presents a detection condition, which turns out to be a TR in the order of 2500 Ohm.m^2, for the same streamer height.

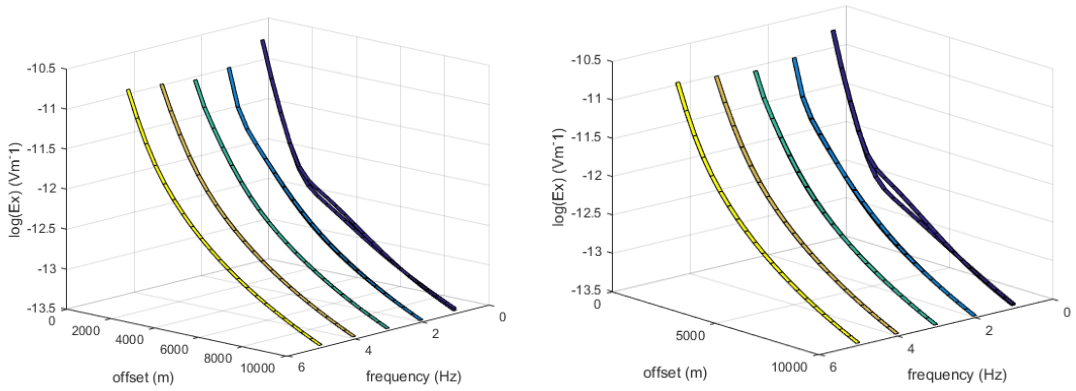

(a) (b)

FIGURE 3.46: *CSEM responses related to CSEM concepts with model parameters: (a) 530m streamer height and 10000 Ohm.m^2 1500m deep target, (b) 530m streamer height and 2500 Ohm.m^2 1000m deep target*

Furthermore, figure 3.46.a exhibits that even in the presence of very good target conditions (TR=10000 Ohm.m^2), seeing targets 1500m below the ocean floor would be impossible even when very low frequency (0.2 Hz) is used, if high altitude streamer (20m below the sea surface in this case) is used. This concludes that this new CSEM scheme when sea depth is considered around 500m, aims targets no deeper that 1500m. However, more accurate background resstivity estimation and experiment instruments may mitigate the detection level of NAR=0.15-0.2 which is currently accepted in the literature.

However, if there is no constraint on stremar height, therefore regarding varying streamer height when all the other parameters are fixed to specific values, figure 3.47.a and 3.47.b gives reasonable results. Figure 3.47.a suggests a model where 100m thick target is located 1500m below the ocean floor with frequency 0.2 Hz. In this case, it is possible to resolve the target streamer heights up to 430m. On contrary if the same configuration is preserved except target depth which is 2000m now, streamer heights up to only 230m is supported for clear detection as figure 3.47.b indicates.

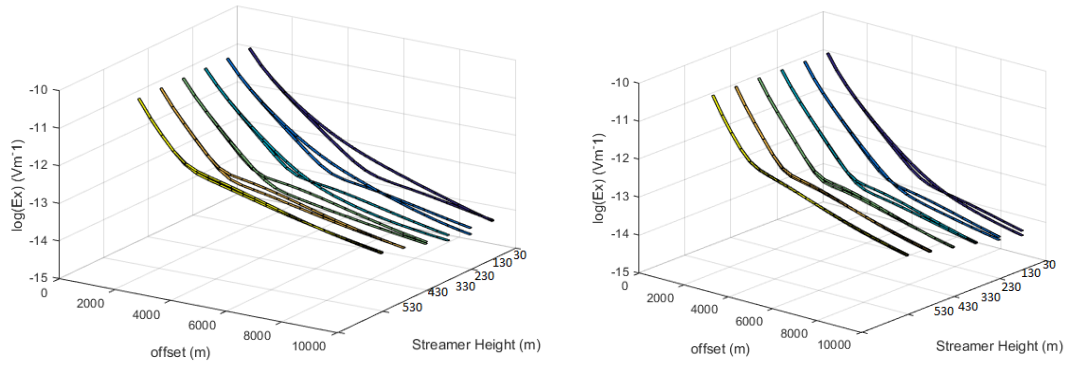

(a) (b)

FIGURE 3.47: *CSEM responses related to CSEM concepts with model parameters: (a) 10000 Ohm.m^2 1500m deep target, 0.2 Hz frequency (b) and 10000 Ohm.m^2 2000m deep target, 0.2 Hz frequency in 550m deep sea*

Notice that as streamer height increases, the distance that wave component which heads for sea surface must propagate diminishes, consequently, airwave effect appears in the earlier offsets. Linear shift is very clear in figure 3.47.

Because of operational interests, it is worth to dwell on maximum streamer altitude (530m) a little bit more. Figure 3.48a and 3.48.b show the results of a 0.4 Hz experiment that issues a varying target depth with a transverse resistancee of 10000 Ohm.m^2 (100 m thick). It seems that when 0.4 Hz is used as probing frequency, even very good targets can only be detected in depths as shallow as 500m. Related mean normalized difference given in figure 3.48.b supports that, indeed, there is no detection for depths greater than ~650m if values are interpolated.

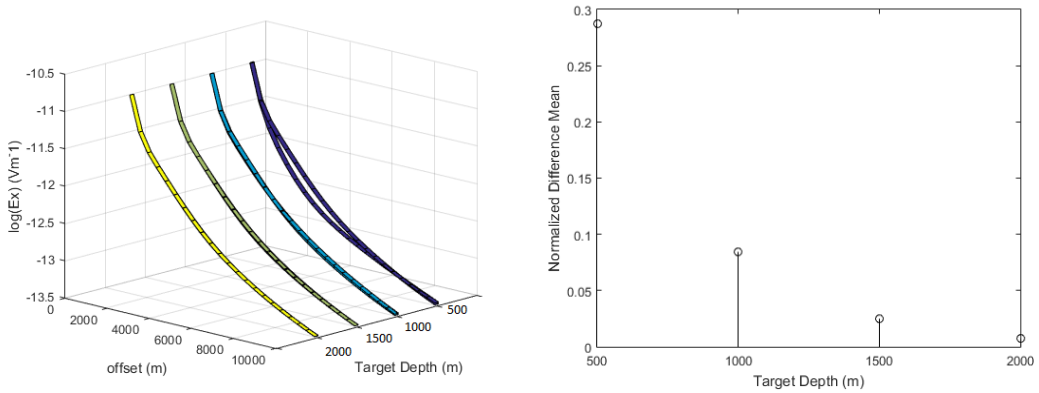

(a) (b)

FIGURE 3.48: *CSEM responses for model parameters 10000 Ohm.m^2 target with varying depth, 550m deep sea, 530m streamer height and 0.4 Hz frequency: (a) MVO, (b) Mean normalized difference for varying target depth*

If the same configurations, except a new frequency 0.2 Hz, are used, results given in figure 3.49 are reached. In this frequency, a well conditioned target (TR=10000 Ohm.m^2) is subjet to detection even around 1500m of burial depth.

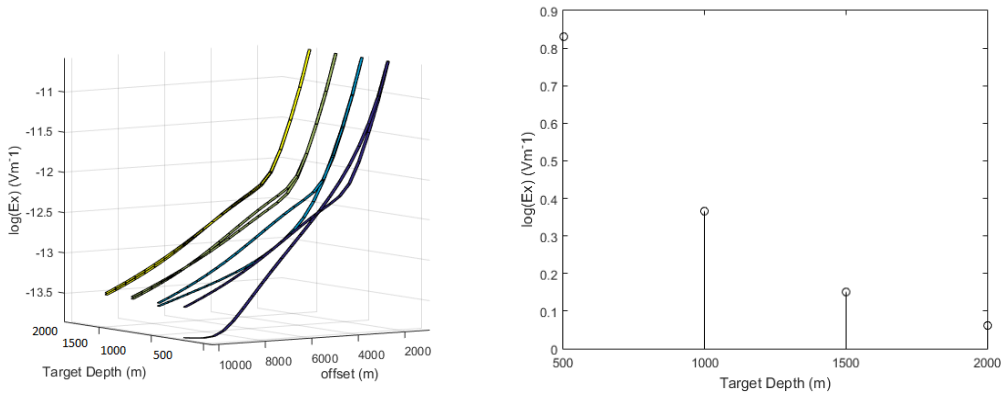

(a) (b)

FIGURE 3.49: *CSEM responses for model parameters 10000 Ohm.m^2 target with varying depth, 550m deep sea, 530m streamer height and 0.2 Hz frequency: (a) MVO, (b) Mean normalized difference for varying target depth*

Also notice that in higher frequency case given in figure 3.48.b, normalized amplitude difference decays more rapidly.

In brief, a new CSEM implementation which hosts a streamer consists of transmitter and receivers together, when moderate sea depths are considered (550m), is operational and flexible for streamers located in mooderate altitudes. However, as streamer altitude increases, detectable range of model parameters are getting more and more squeezed for most in frequency spectrum, such that only a low frequency 0.2 Hz provides detections up to 1500m deep targets. On the other hand, for the same TR given in previous case (10000 Ohm.m^2), frequency 0.125 Hz, which can be ragarded as the first harmonic of most experiments, provides good detection capabilities, though. As given in figure 3.50, in this case, detections up to 2000m target depth is promised.

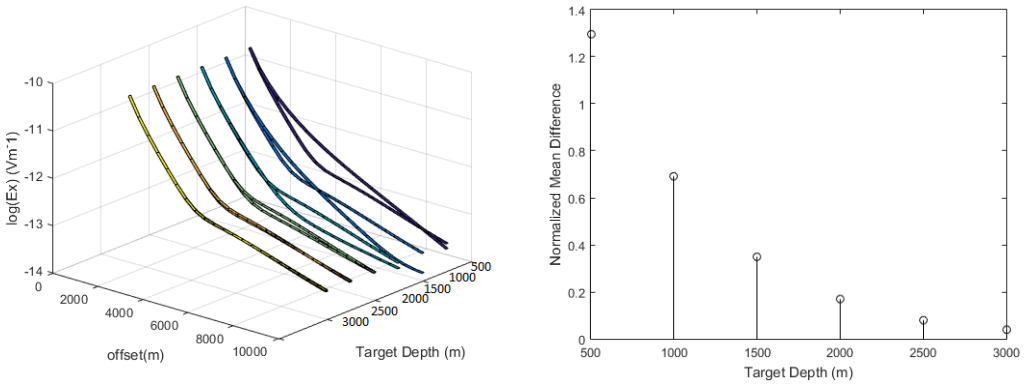

(a) (b)

FIGURE 3.50: *CSEM responses for model parameters 10000 Ohm.m^2 target with varying depth, 550m deep sea, 530m streamer height and 0.125 Hz frequency: (a) MVO, (b) Mean normalized difference for varying target depth*

3.4.2.2.3 Deep Waters

Performance of alternative CSEM applications intoduced for very shallow and moderate deep waters will be studied for deep waters in this section. To begin with, sea depth is chosen to be 960m and four possible streamer altitudes as 30m, 330m, 630m and 930m above the ocean floor are set. Target TR is chosen to be 10000 Ohm.m^2 for all the cases (100m thick, 100 Ohm.m resistive).

As the main focus of CSEM alternatives must be the case where the streamer is towed at maximum altitude (close to surface), towing height of 930m will be considered first. As figure 3.51.a indicates, around 1km water depth, such a system is able to detect targets up to 1500m. This is somehow an unexpectedly fine result when the serious depth is considered. It is worth bearing in mind, such detection range is available for low frequency used: 0.125 Hz. It can be shown that even for 0.375 Hz harmonic, system depicted in figure 3.51.a provides no detection even at 500m target depth, due to stronger decay through the brine.

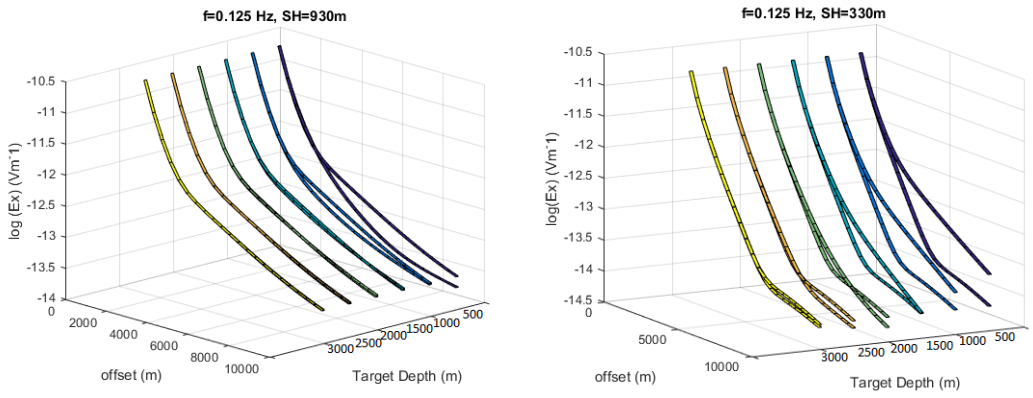

(a) (b)

FIGURE 3.51: *CSEM responses related to model parameters 0.125 Hz frequency, 960m deep sea; (a) 930m streamer height, (b) 330m streamer height for varying depth of 10000 Ohm.m^2 target*

On the other hand, expectedly, for a lower altitude streamer, targets of depths up to 3000m are subject to clear detection as seen in model represented in figure 3.51.b for low frequency 0.125. This case where streamer is towed considerably deep, 330m above the floor, even allows detections for targets buried at 1500m, in the presence of 1 Hz probing frequency, as represented in figure 3.52.

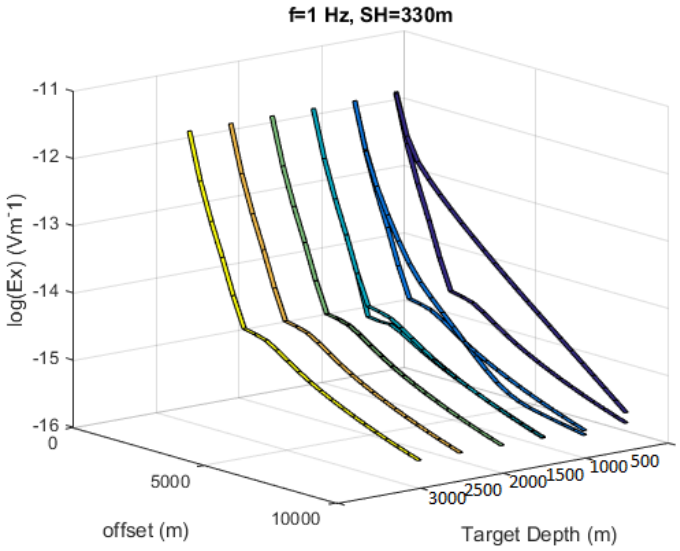

FIGURE 3.52: *CSEM responses related to model parameters 1 Hz frequency, 960m deep sea, 330m streamer height for varying depth of 10000 Ohm.m^2 target*

However, for high frequencies, care must be taken, because field amlpitude decays too rapidly with increasing offsets, thus, signal may remain below the noise threshold 10^{-15} Vm^{-1} at some points.

As far as the impact of the change of streamer height is concerned, system responses plotted for constant target depths would be useful. Thus, following two figures are prepared. Since it is shown in figure 3.51.a that even 930m streamer altitude case guarantees detections up to targets with depths up to 1500m, figure 3.53a and 3.53.b issue constant target depths of 2000m and 3000m respectively.

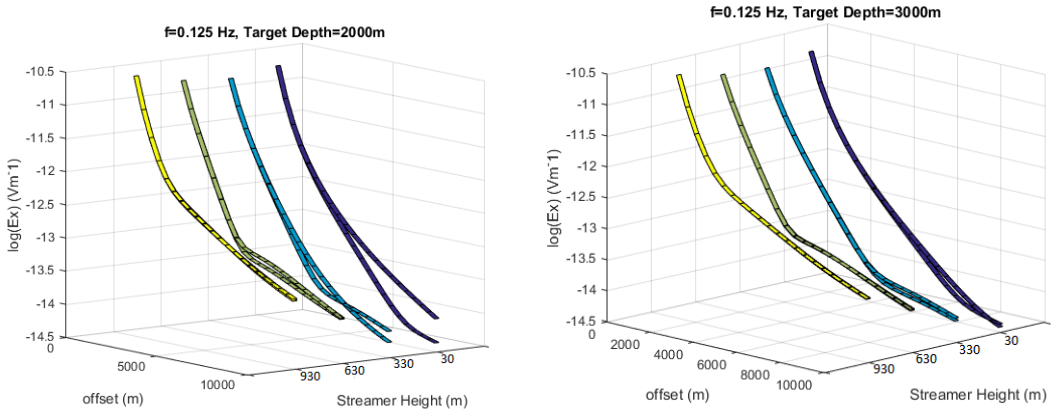

(a) (b)

FIGURE 3.53: *CSEM responses related to model parameters 0.125 Hz frequency, 960m deep sea, 10000 Ohm.m^2 target; (a) 2000m target depth (b) 3000m target depth for varying streamer height*

Figure 3.53 shows that case related to streamer altitude 930m (30m below sea surface) is not able to detect the targets. However, it seems that for targets buried up to 2000m below the floor, case related to a streamer altitude of 630m provides detection, while if target is buried 3000m below the floor, cases where streamer altitudes up to 330m adopted, are slightly able to detect this deeply located target.

Now i introduce a new sea depth, 1560m, and possible streamer altitudes as 30m, 330m, 630m, 930m, 1230m and 1530m. To investigate the detection performance when the most operational streamer amplitude, which is 1530m, is adopted, figure 3.54 is prepared. Figure 3.54 shows that there is no detection even when target is buried 500m below the sea bed. This is bad news, because the view means that kind of CSEM experiments in seas deeper than 1500m, is not able to detect the target, unless it is buried just 100m below the floor.

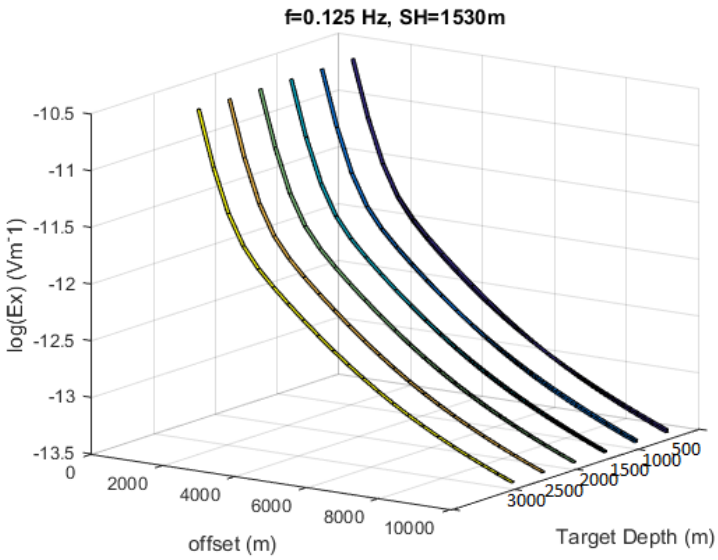

FIGURE 3.54: *CSEM responses related to model parameters 1 Hz frequency, 960m deep sea, 330m streamer height for varying depth of 10000 Ohm.m^2 target*

Hence, it is more convenient to concentrate the focus on flexible streamer height cases. In figure 3.55, received field responses with background responses are given for varying streamer altitude. In condition with target depth of 3000m, at most, the height of 630m promises detection.

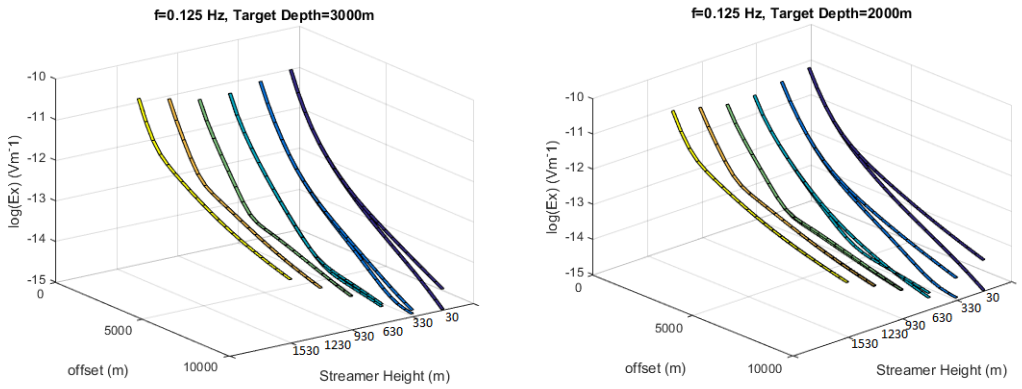

(a) (b)

FIGURE 3.55: *CSEM responses related to model parameters 0.125 Hz frequency, 1560m deep sea, 10000 Ohm.m^2 target; (a) 3000m target depth (b) 2000m target depth for varying streamer height*

However, if shallower target (2000m) is aimed, streamer altitudes up to 900m seems to be effective.

As far as constant streamer altitudes are concerned, impact of target depth change acts as given in figure 3.56.a and 3.56.b which adopts altitudes 630m and 1230m respectively. Figure 3.56.a is critical, because it suggests that on this altitude and frequency 0.125 Hz, even targets lie 3000m below the seabed are subject to detection. This immediately leads to the idea that any streamer altitude smaller than 630m in 1560m sea, will provide detection capability. Thus, assuming flexible streamer height is available (if available), there is again no need for receiver deployment on the floor unless very high frequencies are needed to be used.

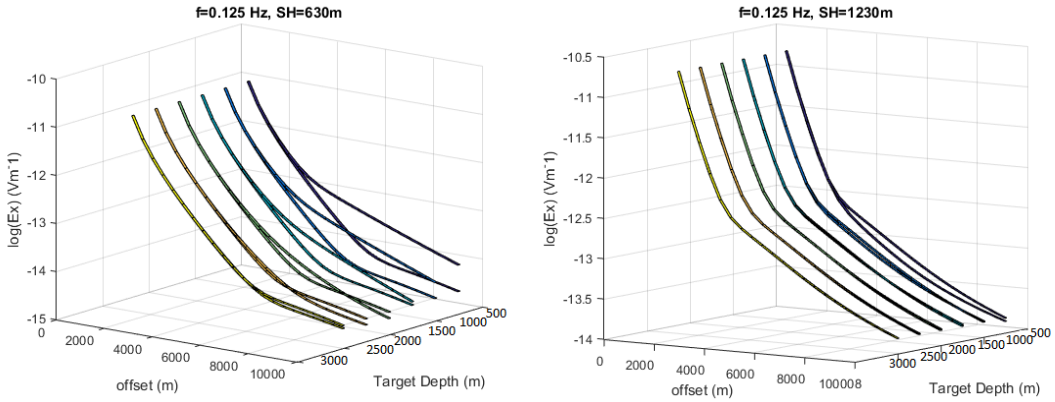

(a) (b)

FIGURE 3.56: *CSEM responses related to model parameters 0.125 Hz frequency, 1560m deep sea, 10000 Ohm.m^2 target; (a) 630m streamer height (b) 1230m streamer height for varying target depth*

On the other hand, figure 3.56.b introduces a greater streamer altitude, which limits the detection ability to the targets buried up to only 1000m below the sea bed.

Considering the models related to figure 3.55, but this time as far as a greater harmonic, 0.375 Hz is concerned, results appear as given in figure 3.57.

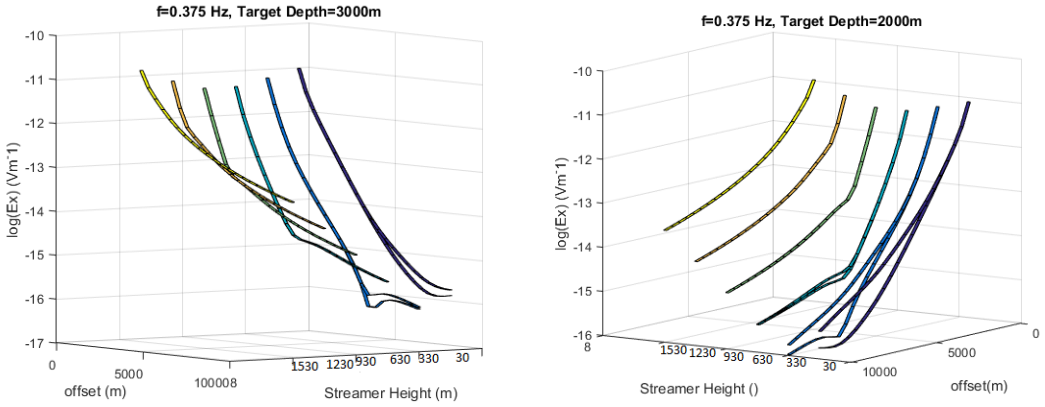

(a) (b)

FIGURE 3.57: *CSEM responses related to model parameters 0.325 Hz frequency, 1560m deep sea, 10000 Ohm.m^2 target; (a) 3000m target depth (b) 2000m target depth for varying streamer height*

In this case, higher frequency causes stronger decays. It is clear that for streamer locations closer to the floor, signals are more distinguishable. This is because of reduced airwave effect. However, for higher altitudes, airwave dominates quickly. Also notice that in some areas, although it looks like received field and background fields look like distinguishable, they actually remain below noise threshold: 10^{-15} Vm^{-1}. This data is meaningless.

In conclusion, CSEM scenarios that adopt transmitter-receier array streamer instead fixed receivers on the floor, promises. The real challenge is, for the most operational case that streamer altitude is chosen to be maximum, namely close to the water surface, only small harmonics are able to reach the bottom and effective target depth detection range seems to be poor, 1500m for 960m deep sea, and even smaller than 500m for 1560m deep sea. Therefore, for deep water surveys, surface towed systems are not recommended. However, if a flexibility is present on streamer's altitude, whoose results are just discussed, this new CSEM alternative works fine, and there can be found reasons to prefer it to the conventional one, where receivers are located on the sea bed.

3.5 Impairments

3.5.1 Incorrect background model estimation

This section is prepared to emhasize the importance of background model in CSEM surveys. Since observed data is expected to be evaluated with respect to a reference model, deviations on background model would obviously cause deviations in the difference between observed data and expected data in presence of no anomaly (background model), which are simply deviations on sensitivity. In this context, an overestimation of background model might be expected to bring on a performance loss when (3.5) is taken into consideration.

Figure 3.58 represents a CSEM experiment based on 5 Ohm.m resistive background model where 100m thick, 25 Ohm.m resistive layer is placed 2000m below sea-bed. Here conventional CSEM approach is adopted, thus, transmitter and receivers are located 30m and 0.3m above sea-bed, respectively. Frequency is set to 0.4 Hz and sea depth is chosen to be 500m to get more realistic results. Parameters are chosen such a way that a slight visibility of reservoir ensured in 5 Ohm.m background model as depicted in figure 3.58.a and 3.58.b.

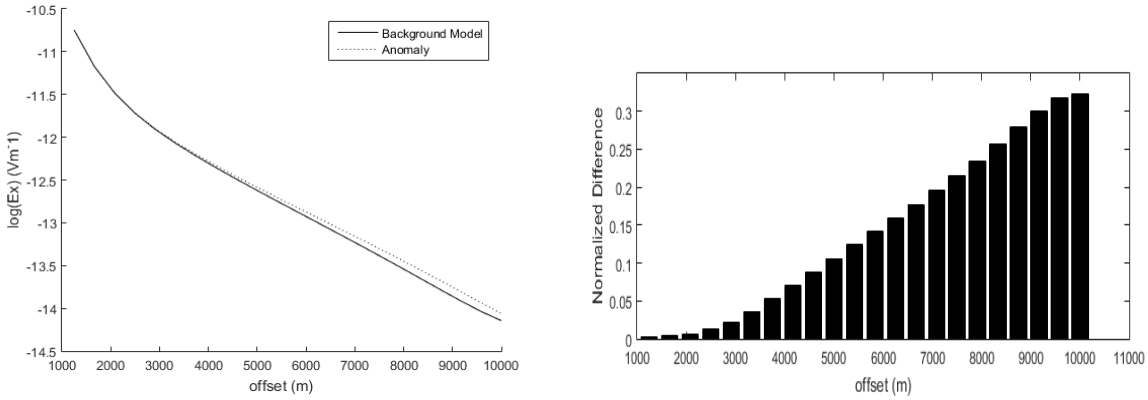

(a) (b)

FIGURE 3.58: *Slight detection related to model parameters 0.4 Hz frequency, 100m thick, 25 Ohm.m resistive, 2000m deep (below floor) target for 5 Ohm.m background resistivity and 500m sea depth; (a) MVO, (b) Normalized amplitude response: DETECTION*

Here, normalized difference behaviour with respect to offset is around 0.2, which is considered as a detection. Hence, there is a detecion. However, if background resistivity is incorrectly detemined as 8 Ohm.m, result are gathered as shown in figure 3.59.

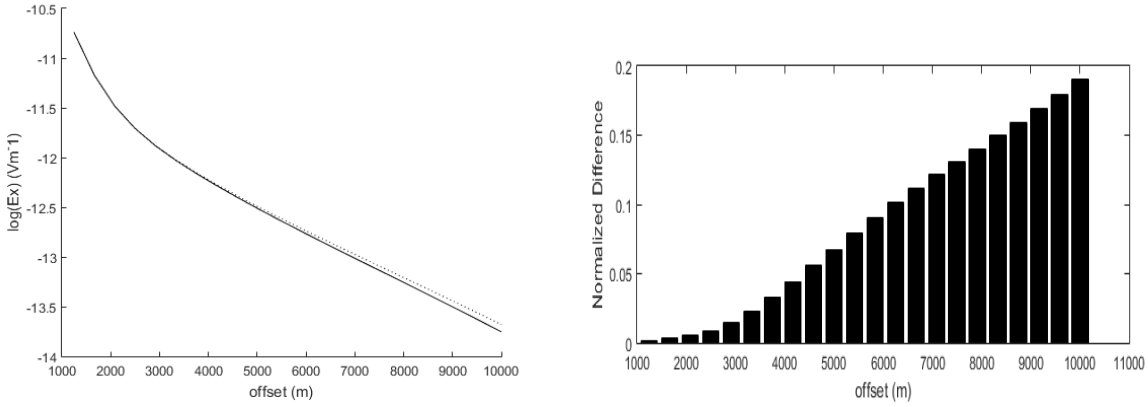

(a) (b)

FIGURE 3.59: *Slight detection related to model parameters 0.4 Hz frequency, 100m thick, 25 Ohm.m resistive, 2000m deep (below floor) target for 8 Ohm.m background resistivity and 500m sea depth; (a) MVO, (b) Normalized amplitude response: NO DETECTION*

Normalized difference behaviour versus offsets always remain below 0.2. There is no detection in this case. As clearly seen, an overestimation of background model could easily lead targets to be missed, especially around the edges of detection capabilities.

For the sake of discussion, a more compact dataset that reveals detection sensitivities based on background model regarding varying TR and burial depth must be provided.

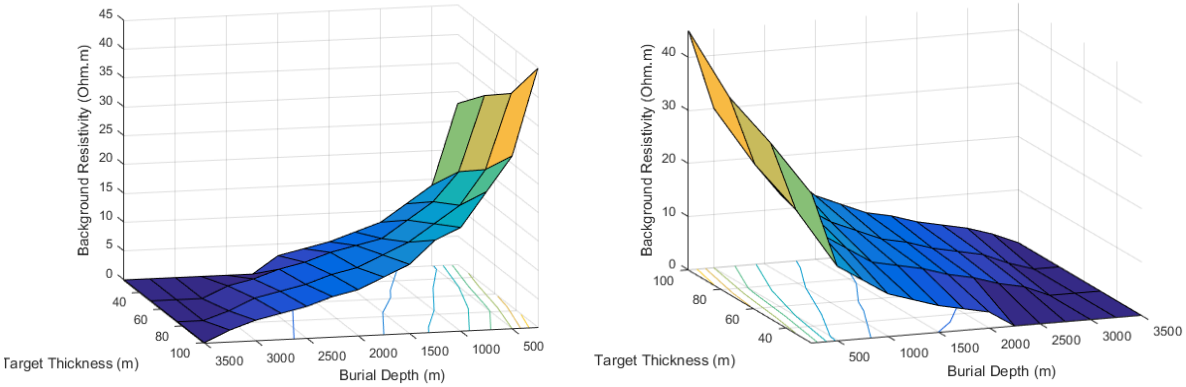

FIGURE: 3.60: *Limit background resistivities (last acceptable) for 100 Ohm.m resistive target detection as far as varying target depth and varying TR are concerned. Plots exhibit different perspectives of each other: for conventional CSEM*

In figure 3.60, for conventional CSEM scenario, where transmitter and receivers are located 30m and 0.3 m above seabed respectively, specific background resistivity (maximum background resistivity) that allows detection, is given for a 100 Ohm.m resistive layer that vary in thickness. Here, for instance, a 50 m thick target buried 1000m below the ocean floor can be detected in presence of resistive background with resistivty up to 12 Ohm.m. That means, for given real background resistivity around 10 Ohm.m, if surveyor determines it as 13 Ohm.m, the target is not possible to be solved. However, for a real background resistivity around 13 Ohm.m, if one determines it as below 12 Ohm.m, clearly a false alarm is present. Results clarify the importance of detecting background resistivity accurately. In addition, it is not very difficult to claim that even if background resistivity estimation is conducted accurately enough to have a true detection, any deviations from real background resistivity values will cause performance deviations which are unwelcome. Also notice that contours linearly act.

3.5.2 Anisotropy

Another very important spoiler effect is anisotropic nature of resistivities of underlying structures. Since, as already metioned, resistivity is a tensor in general, its estimation for scales as large as CSEM is concerned, is simply very difficult. [39] states that vertical resistivity is usually few times higher than horizontal resistivity. [3] indicates that even now, physical dynamics that govern resistivity anisotropy of underground structures, have not yet been understood. The most reliable data is generally acquired from 3D well logs, which suggests that the parameter is very variable. Also background model estimation built by seismic data is said to be promising. Moreover, true background resistivity can also be estimated from MT, however, this method basically requires even greater horizontal resistivity knowledge that CSEM can provide.

In the case of resistivity anisotropy such that vertical one is two times the horizontal one, [3] states the impact of detection performance by providing canonical representations as shown in figure 3.61 with model parameters same with those stated in model represented in figure 3.16.

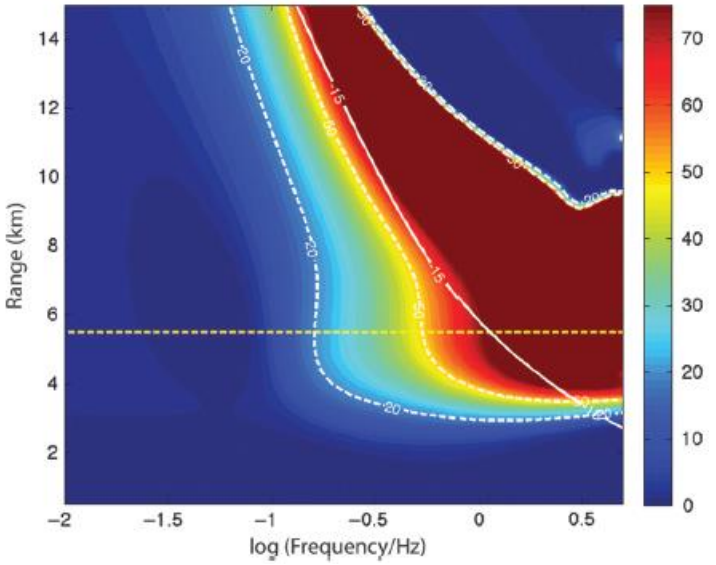

(a)

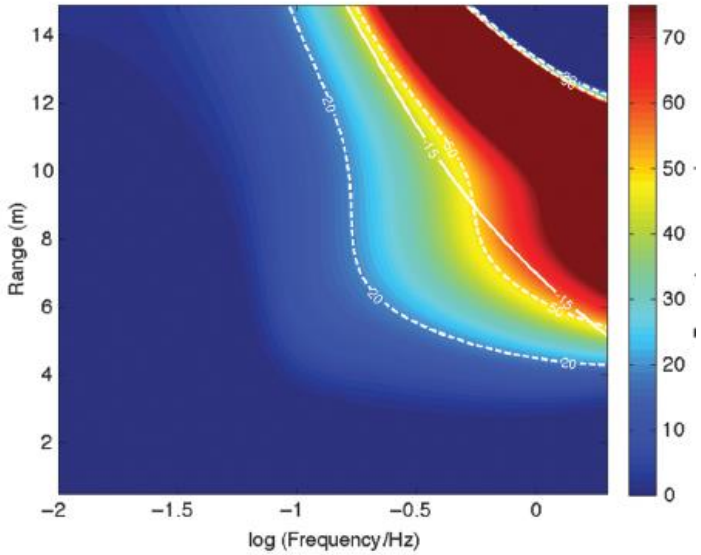

(b)

FIGURE 3.61: *Canonical representations of the model with parameters: 1500m target depth, 1500m sea depth, 2500 Ohm.m^2 target TR with; (a) isotropic background, (b) anisotropic background* [3]

It is clear that figure 3.61 suggests, isotropic estimation of anisotropic background leads false alarms.

Chapter 4

Migration

4.1 Introduction to migration

In seismic, migration is a commonly adopted and discussed imaging technique [40] that benefits constructive superposition of stimulant fields scattered by internal reflectors. In acoustic experiment, the occurance that scatters the incoming energy is simply strata interfaces. Alongside, it is suggested that migration might be implemented to electromagnetic surveying applications [25] inwhich, the scatterers are resistivity anomalies. In general, all kind of resistivity amomalies are subject to EM migration, like basalt floors, conductive metallic ores, hydrocarbon prospects. Considering the fact that, underlying hydrocarbon saturated porous structures present resistivity anomalies, EM migration can be be given as a fine tool for prospect hunt. In fact, EM migration is also capable of overruning "inversion" algorithms ,that regarded as the main standard imaging tecqnique for resistivity mapping, in many viewpoints. For expample, evaluation of data with EM migration would take several order of magnitudes less time than that of inversion, furthermore, EM migration technique requires no a-priori information, while inversion does.

In this chapter, as the first step, definition and theory of EM migration will be given. Then, similarities and differences between seismic migration and EM migration will be discussed. Finally, limitations and robustness of the technique will be investigated for point and block targets varying in depth, and transverse resistance. And impact of frequency will be discussed introducing several noisy conditions. Furthermore, a new imaging condition will be proposed and empirically analysed.

Intrinsically, migration is a method that avails locating a source or sources, given many receivers. Considering, a waveform is sent from source to receiver, migration suggests that extrapolating the temporal or spatial characteristics recorded at receivers into the space that it possibly comes from, would cause constructive effects where the source is located. For a 2D acoustic media, imagine a point source has radiated energy, concentrated into a small interval in time. For simplicity, it can be taken as delta Dirac funtion. Several receivers, in this case, would record the incoming signal in different times. If one receiver rewinds the time, it comes up with a parabol, that possibly can host the source. However, with the temporal information of a second receiver, now the intersection of two parabols is present as depicted in figure 4.1

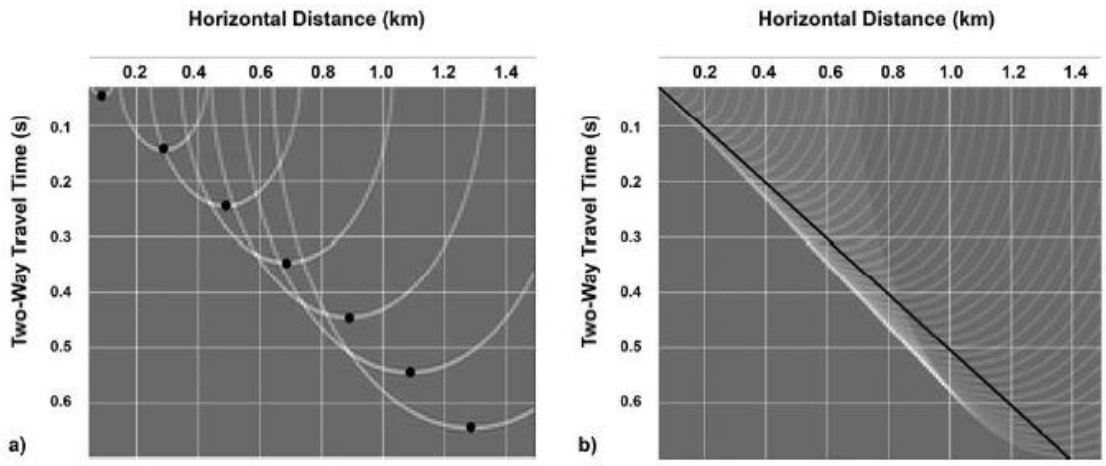

FIGURE 4.1: *Principle of migration* [41]

Repeating the experiment for also other available receivers, indeed, improves the the value assigned to the specific position that source is located by means of constructive interference at this point comes from all receivers' temporal information. Principally, concept is similar to GPS.

4.2 Electromagnetic migration

The "source" abovementioned, is usually underground scatterers (of EM or seismic energy) and algorithmically speaking, a discrete migration domain is necessary to be defined, which likely includes the scatterers (or sources, more generally).

In EM migration concept, magnitude of received fied gives important clue about the features of medium subject to propagation and conductivity of the scatterer layer. Furthermore, temporal characteristic of received field is phase. Phase information is crucial for depth localization.

In CSEM applications, guided received field components are mentioned before (bölüm ver) are strongest ones in most cases. However, considering their effect is compensated of minimised, recorded field can be as scattered field at the surface, which is subsequent to primary field that propagates towards the target as shown in fig mig2. Primary and scattered fields are also widely called as "Downgoing Continuation" and "Upgoing Continuation". In 2D space (x,z) considering a unitary amplitude and zero phase source field emitted from source located in position $\overrightarrow{r_{src}}$, using planar wave solution (helmholz denklem ver), exploiting phaser notation wavefield in any arbitrary position($\overrightarrow{r_{tar}}$) can be given as

$$P_s(\overrightarrow{r_{tar}}) = A(r)\, E_s = \frac{1}{4\pi r_{pr}}\ e^{j\vec{k}\cdot\overrightarrow{r_{pr}}} \tag{4.1}$$

where E_s denotes extrapolation function for plane waves (also known as Green's solutions) which is responsible for phase change, A stands for geometrical attenuation determined by the absolute value of $\overrightarrow{r_{tar}}$ - $\overrightarrow{r_{src}}$ = $\overrightarrow{r_{pr}}$ and for simplicity, r_{pr} stands for $|\overrightarrow{r_{pr}}|$. For position $\overrightarrow{r_{tar}}$ located on scatterer-background interface, there is a reflection, and taking into account the reflectivity behaviour [25] and corrresponding resistivity where index 2 denotes the scatterer medium, are given by

$$\alpha = \frac{(\sqrt{\sigma_1} - \sqrt{\sigma_2})}{(\sqrt{\sigma_1} + \sqrt{\sigma_2})} \tag{4.2}$$

$$\rho_2 = \left(\frac{1+\alpha}{1-\alpha}\right)^2 \rho_1 \tag{4.3}$$

which leads the scattered wave measured on a specific receiver located in position $\overrightarrow{r_{rc}}$ take form of

$$S_r(\overrightarrow{r_{rc}}) = \alpha \,.\, A(r)\, E_r = \alpha . \frac{1}{4\pi r_{sc}}\; e^{j\vec{k}\cdot\overrightarrow{r_{sc}}} \tag{4.4}$$

where index $_r$ denotes the receiver number, and $\overrightarrow{r_{sc}}$ is the position vector $\overrightarrow{r_{rc}}$ - $\overrightarrow{r_{tar}}$ = $\overrightarrow{r_{sc}}$ and r_{sc} is the absolute value of $\overrightarrow{r_{sc}}$. Indexes pr, tar, sc stands for primary, target, scattered, respectively. Primary field and secondary field vectors $\overrightarrow{r_{pr}}$ and $\overrightarrow{r_{sc}}$ are shown as red and blue arrows respectively, in figmig2. Notice that, both P_s and S_r representations are given in narrowband, provided that a single frequency is used.

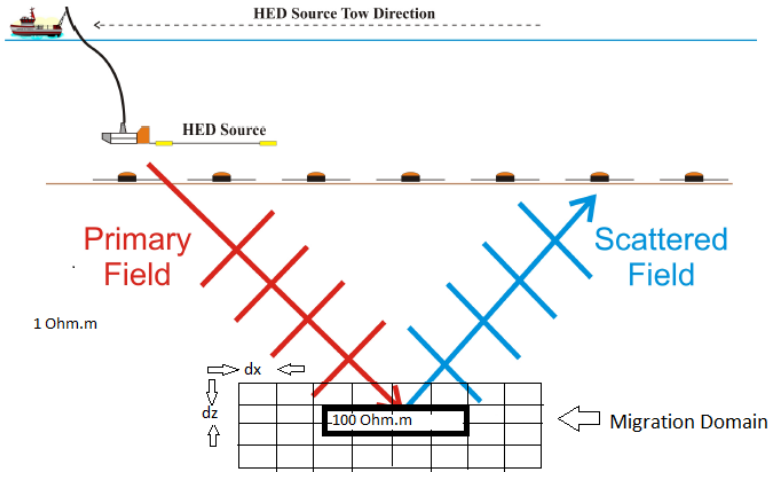

FIGURE 4.2: *Electromagnetic migration layout*

Material discussed up to now is enough to give the definion of field (emitted from source s) measured in receiver r as

$$D_s^r = P_s\, S_r \tag{4.5}$$

and of all data set for a single frequency as

$$\text{data} = \sum_r \sum_s D_s^r \tag{4.6}$$

in noise free approximation.

The main principle in EM migration is rewinding the measured field into all points in migration domain, which are defined as position vectors $\overrightarrow{r_{tar}} = \overrightarrow{r_x} + \overrightarrow{r_z}$ by mentioned extrapolating functions, however, considering reverse action in time. This procedure is governed by backwards propagation of upgoing continuation as

$$\text{TR}_\text{r} = \frac{1}{\text{A(r)}}\text{E}_\text{r} = 4\pi r_{sc'} e^{j\vec{k}\cdot-\overrightarrow{r_{sc'}}} \tag{4.7}$$

where time reversal is achieved by reversing the amplitude and position vector and TR_r stands for "time reversal process towards migration domain" and $\overrightarrow{r_{sc'}} = \overrightarrow{r_{rc}} - \overrightarrow{r_{tar}}$. Considering one data sample that represents one source and one receiver, then resulting time reversed data signal in arbitrary position (position information is embedded in $\overrightarrow{r_{sc'}}$) in migration domain is given by equation

$$M_s^r = D_s^r\, TR_\text{r} = P_s\, S_r\, TR_\text{r} \tag{4.8}$$

where M_s^r is migrated field. For one data sample and all defined migration domain points, which is assumed to contain the target, we have M_s^r values in the number of N_x x N_z, where N_x, N_z are numbers of differential units that discretize spatial domain (number of dx and dz in fig mig1), for x and z axis respectively. For simplicity, let us drop reflection coefficient for now. In this case, phase of multiplication $S_r\ TR_\text{r}$ is equal to $\text{k}(\text{r}_\text{sc} - \text{r}_\text{sc'}) = \Phi$. For $\text{r}_\text{sc} - \text{r}_\text{sc'} = \lambda\text{n}$, where n is integer, resulting phase will be equal to $2\pi n$, and $\text{phase}(\text{P}_\text{s}) = \text{phase}(M_s^r)$. This condition is simply called *detection*, however, there might be many migration domain coordinates without any scatterer, nevertheless satisfy it. Yet, we are looking for just one specific point (scatterer), where r_sc is exactly equal to $\text{r}_\text{sc'}$ and resulting phase is 0. The key fact is that, the migration points that randomly satisfies expression $\text{phase}(S_r\, TR_\text{r}) = 2\pi n$ for one specific source-receiver set, would very unlikely satisfies it for the next source-receiver set. However for the scattering point, condition is satisfied for all source-receiver combinations. Therefore, assigning all primary fields to all migration domain grid (for just one source-receiver pair) and introducing the ratio with migrated fields, would decisively provide unitary value:

$$\frac{M_s^r}{P_s} = 1 \tag{4.9}$$

in mentioned scatterer point which surveyor is looking for localization considering ideal case. Then summing over all sources and receivers as:

$$\text{I(x,z)} = \sum_r \sum_s \frac{M_s^r}{P_s} = 1 * \text{Nr} * \text{Ns} \tag{4.10}$$

will create great numbers where scatterer is located. This basicly is, migration.

In fact, geometrical magnitude decay and conduction losses are very strong in CSEM logging, hence, compensating through attenuation (A) may not be an appropriate way.

In most general case, it must be said that M_s^r/P_s normalization for target points would create likely real numbers:

$$\text{Im}\left(\frac{M_s^r}{P_s}\right) = \sim 0 \tag{4.11}$$

hyphotesising emitted source field was zero phase. Moreover, for block targets, perfect phase compensation, for long wavelegths, cannot be guaranteed. Thus, historically, basic imaging condition is given as

$$\text{I(x,z)} = \text{Re}\left(\sum_r \sum_s \frac{M_s^r}{P_s}\right) \tag{4.12}$$

Back into the point scatterer case, up to now, neglecting reflectivity effect, imaging condition suggested that reverse extrapolated (migrated) field M_s^r would be equal to primary field at scatterer point. Notice that, the first one is actually the field that backpropagated in time, till scattering moment. Hence, M_s^r is intrinsically an estimate of reflected field at the same time. Now introducing also reflectivity different from 1, imaging condition just mentioned directly gives reflection coefficient:

$$\text{I(x,z)} = \sum_r \sum_s \frac{M_s^r}{P_s} = \alpha * \text{Nr} * \text{Ns} \tag{4.13}$$

From this information, resistivity behaviour of scatterer medium can be estimated using 0.

Also, imaging condition (2) can be seen as

$$\text{I(x,z)} = \sum_r \sum_s \frac{M_s^r}{P_s}\frac{P_s}{P_s^*} = \frac{M_s^r P_s}{|P_s|^2} \tag{4.14}$$

as well. Apart from the normalization factor of $|P_s|^2$, this version of imaging condition is generally called convolutional imaging condition and (4.10) deconvolutional one. Furthermore, various modifications to mentioned imaging conditions will be suggested soon.

Discused extrapolation and imaging ways are obviously valid for just one field component among E_x, E_z, H_x,H_z. However, it can be shown that in 3D environment, best results are gathered using all 6 components [25]. It is a great challenge to recover all mentioned fields though. On the other hand, except inevitable noise, EM migration resolution and performance suffers also from several facts as long wavelentghs, misestimated background parameters and their heterogeneity, dispersion, immense attenuation. As (gola) states, one basic countermeasure against impairment due to strong attenuation is spatial filtering. The idea is to cut off very strong near field effects that might act as spoilers and far field ones that suffer too much from attenuation, which corresponds small values and large values, respectively, when total propagation distance $r_{pr} + r_{sc}$ is concerned. Variable d_i representing position domain masking cut off values belong to vector d=(d_1, d_2, d_3, d_4), filter can be given as

$$F_r^s(\mathrm{d}) = \begin{cases} 0 \;\; ; \;\; R \leqslant d_1 \\ 0.5 \cdot (1 + cos(-\pi(1 - \frac{R-d_1}{d_2-d_1})) \;\; ; \;\; d_1 \leqslant R \leqslant d_2 \\ 1 \;\; ; \;\; d_2 \leqslant R \leqslant d_3 \\ 0.5 \cdot (1 + cos(-\pi(1 - \frac{R-d_3}{d_4-d_3})) \;\; ; \;\; d_3 \leqslant R \leqslant d_4 \end{cases} \tag{4.15}$$

Including (mask) into work, decisively improve resulting performance observably. However, to be as brief as possible, with and without filter result comparisons are not included.

Respecting the concept discussed, as far as varying frequency and a point scatterer is concerned, varying detection resolution & performance is present. In figure 4.3, results are given for frequencies 0.2 Hz, 1 Hz, 10 Hz and 1 Mhz. As clearly seen, concept suffers from a serious performance degredation as frequency increased. Moreover, for intermediate frequencies, 2-10 Hz, strong vertical side lobs are intruduced, which actually prevents one from detecting the target in vertical axis. Contrarily, for microwave frequencies, point scatterer is perfectly recovered. Terrible resolution for a very commonly adopted 0.2 Hz frequency is gathered as 4 km in x and 2 km in z direction. However, it is a bit better in 1 Hz case, as 2 km in x and 1 km in z direction.

Experiments are held by a model with source number of 1000 and receiver number of 100 which are linearly equispaced on z level 0. Migration domain is discretized in dx=100m and dz=50m. Conductivity of propagation medium is chosen to be 1 S/m, as the most sub-ocean floor sediments, and relative magnetic permeability is set to 1, which states that magnetic effects are neglected. Masking effect (4.15) is applied for all results as well. On the other hand, both E_x and E_z components are used in migration. In the rest of the discussion, for EM migration scenarios, this basic model will be taken as basis.

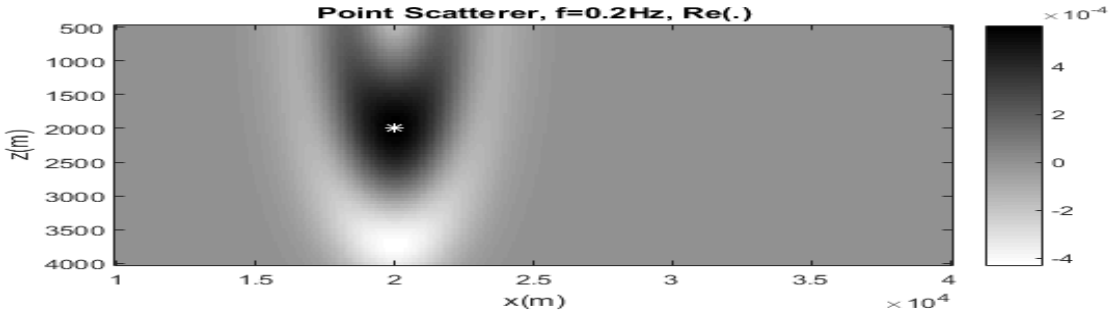

(a)

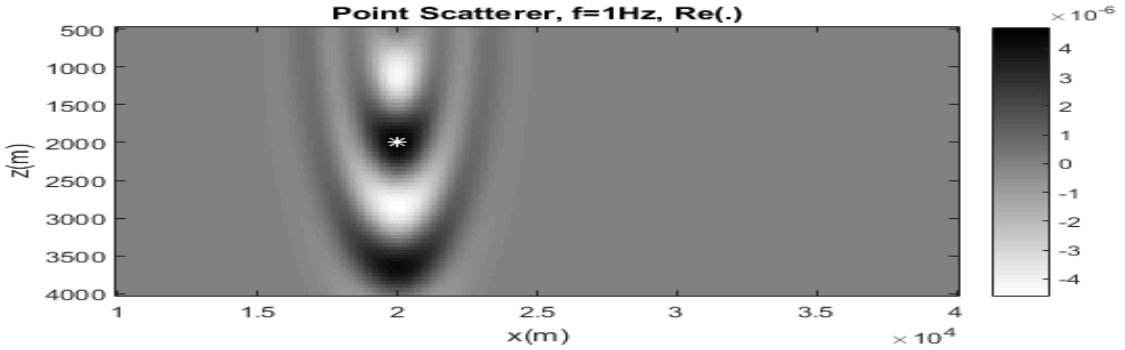

(b)

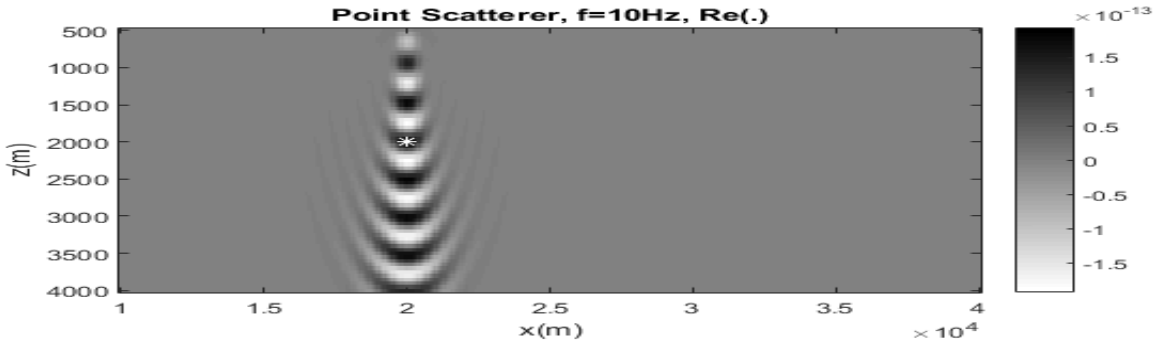

(c)

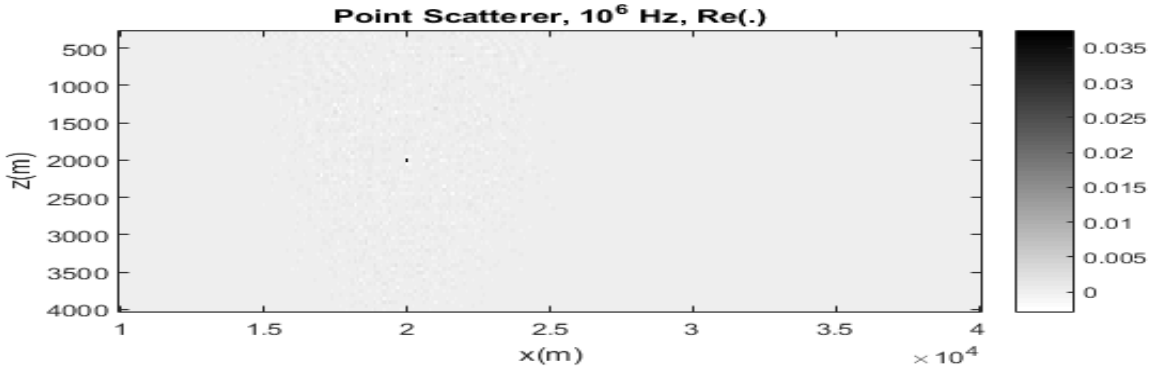

(d)

FIGURE 4.3: *Conventional EM migration: (4.12) applied to point scatterer scenario for; (a) 0.2 Hz, (b) 1 Hz, (c) 10 Hz, (d) 10^6 Hz with target coordinates (20km,2km)*

Gola ([15]) presents a very similar result for the same parametric configurations given in figure 4.4.

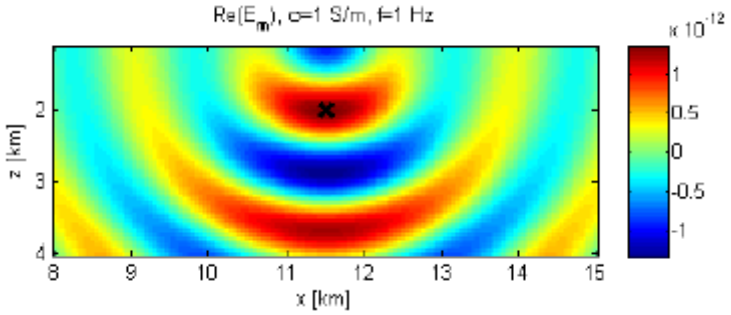

FIGURE 4.4: *EM migration of point scatterer, 1 Hz working frequency* [15]

It is very intuitive that rather than electromagnetic properties of the model, wavelength change might be impacting the performance. This idea is, at least in a quasi reasonable way, testable observing seismic case with same wavelenth employed. Seismic behaviour for long wavelentghs as in the order of thousand meters, as in the case of CSEM, is also bad, spread in both directions in most cases and exhibits very strong uncertainty.

For 1 Hz frequency used only, resulting image contains near and strong vertical side lobs that makes localization of the target in z axis impossible. Moreover, although smaller harmonic, 0.2 Hz provides better vertical certainty, at least for first 4 km, secondary deeper targets tend not to be seen. Apparently, without applying further improvements, detection performance seems to be poor.

4.3 An imaging condition suggestion

It is already mentioned that the standard imaging conditions in literature are very similar to (4.12). Certainly, the contribution related to one source-receiver (s-r) pair in target location (in migration domain) must likely close to be large in real and small in imaginary parts. However, summing over s and r, might cause a lot of useful contributions' to cancel each other in real parts, which must be degrading the imaging quality. Moreover, in the locations where target is located, migration results (for one s-r pair) with small phase (large Re, small Im in magnitude), their ratio would even be larger. This motivation led introducing a new imaging condition

$$I(x,z) = \sum_r \sum_s \left| \frac{Re\left(\frac{M_S^r}{P_S}\right)}{Im\left(\frac{M_S^r}{P_S}\right)} \right| \tag{4.16}$$

which intends to strengthen the contribution where its real part is greater in matnitude. The point that care must be taken is that, as it is, imaging condition will almost never work, because

of the migration contribution events where occasionaly imaginary part gets close to zero. This condition destabilizes the resulting image, thus, an amplitude filter must be applied. In this work, in order to prevent instability, values greater than $10^3 \sim 10^4$ are cut off.

Indeed, for point scatterers, method provides promising results given in reim1abc. These images must be compared with figure 4.3.

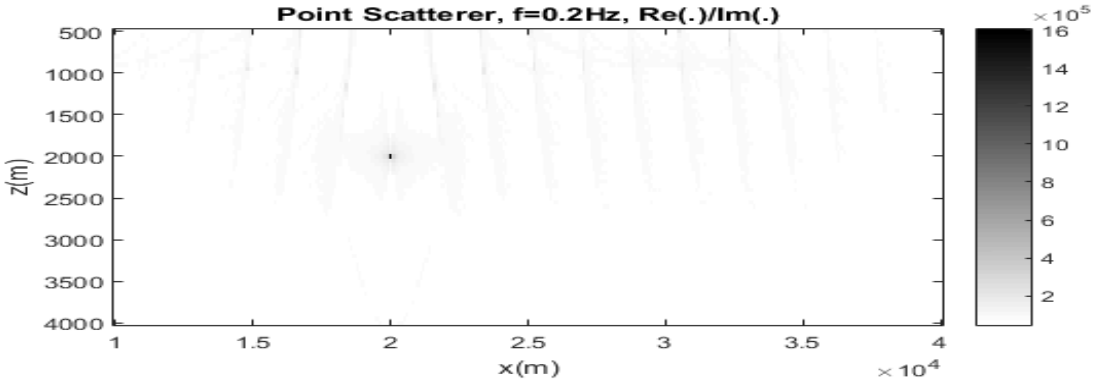

(a)

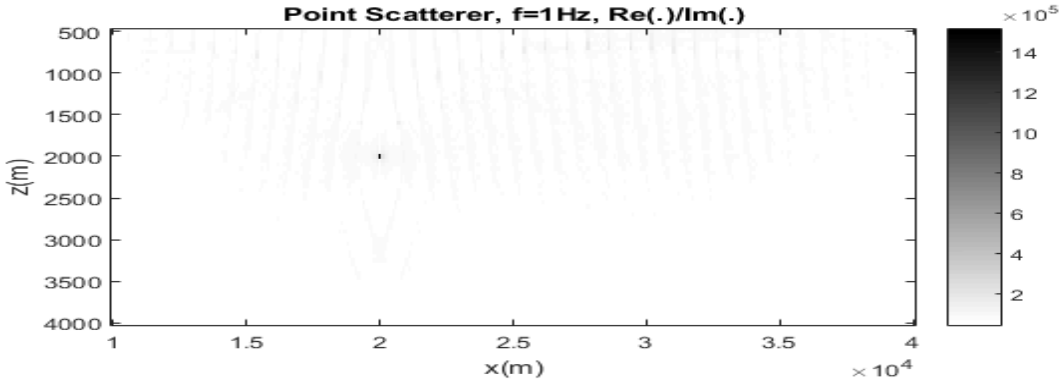

(b)

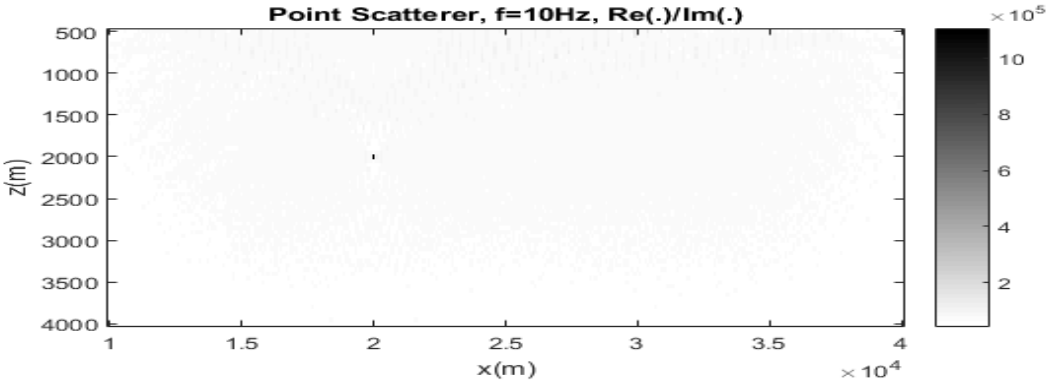

(c)

FIGURE 4.5: *Suggested IC (4.16) EM migration for point scatterer scenario; (a) 0.2 Hz, (b) 1 Hz, (c) 10 Hz with target coordinates (20km, 2km)*

As claerly seen, resolution is maximum achievable, because, scatterer points are recovered completely for any frequency usable in CSEM.

On the other hand for block targets, which is the actual interest in most cases, conventional approach (4.12) would exhibit the results given in Figure 4.6.

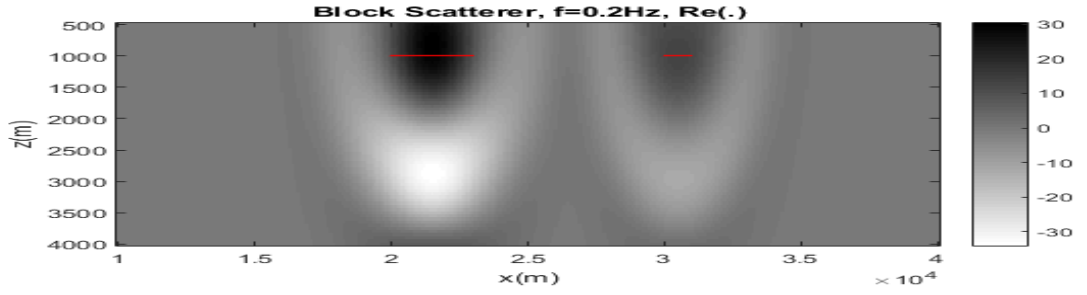

(a)

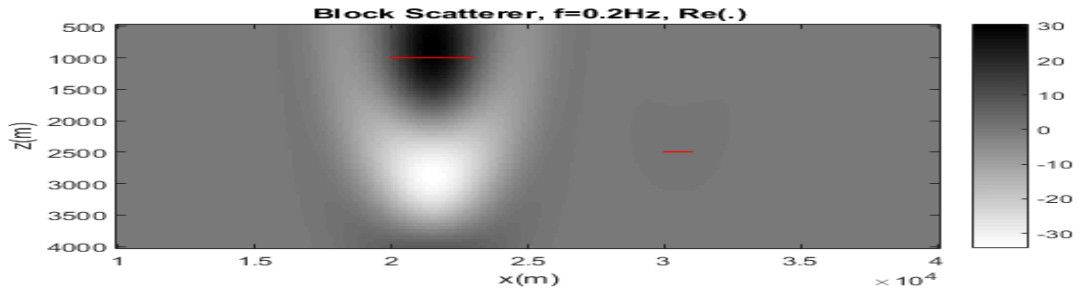

(b)

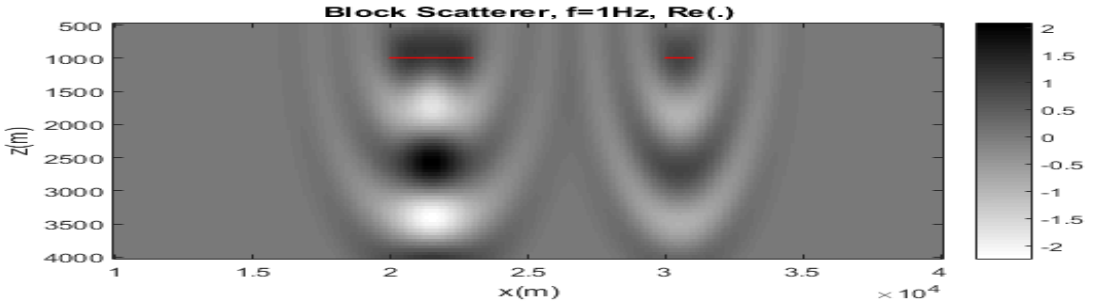

(c)

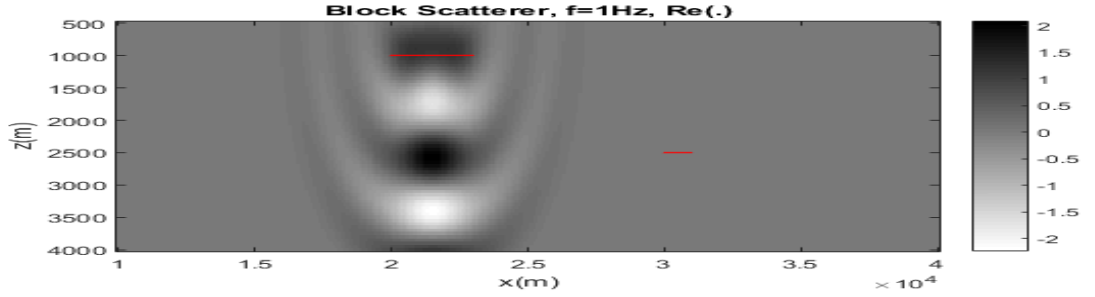

(d)

FIGURE 4.6: *Conventional EM migration: (4.12) applied to block scatterer scenario with actual target locations indicated*

It is clear that results show great uncertainty, with even misdetections. On the other hand, when (4.16) is applied to the scenario represented in figure 4.6, results depicted in figure 4.7 are gathered, respectively.

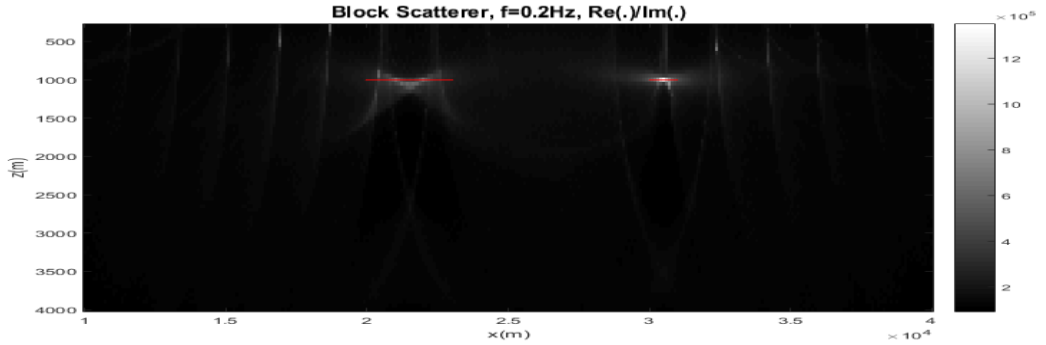

(a)

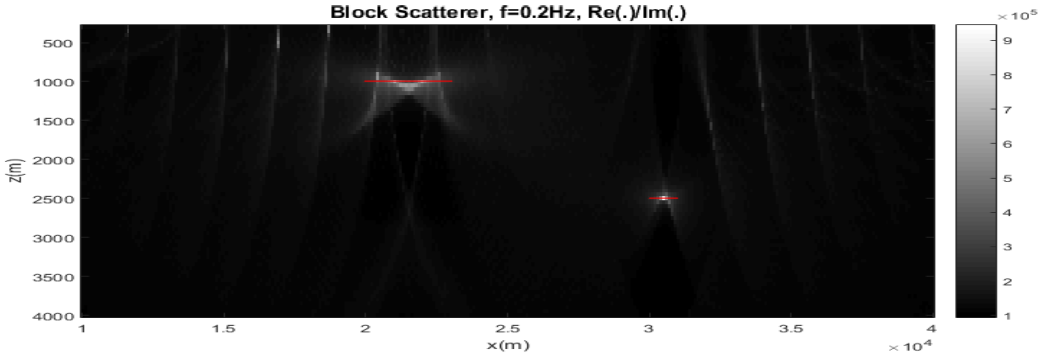

(b)

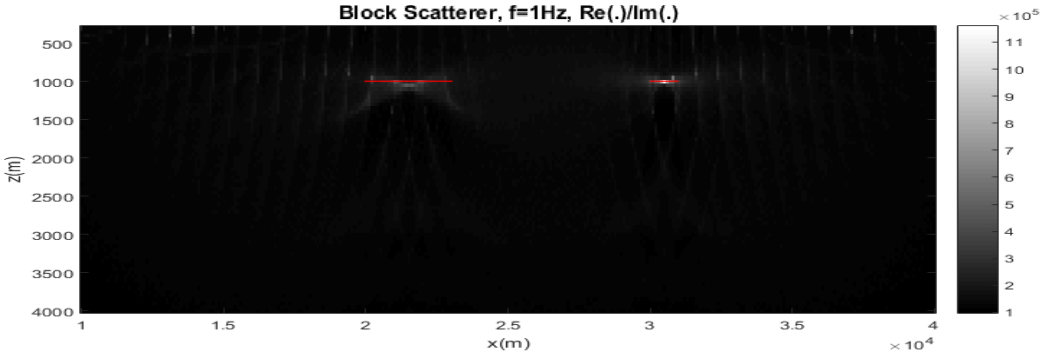

(c)

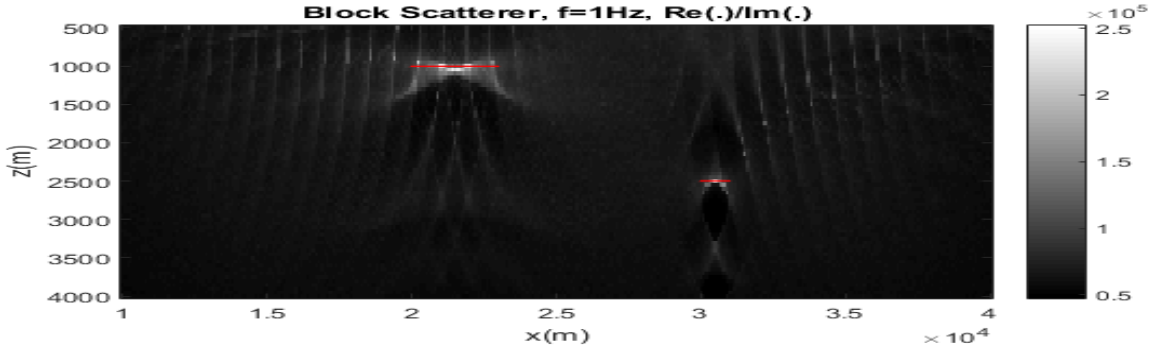

(d)

FIGURE 4.7: *Suggested IC (4.16) EM migration for exactly the same models represented in figure 4.6*

When the brightest focus points are considered, method promises perfect resolution in x axis and 100m resolution in z axis, instead of kilometers provided previously.

As far as the impact of depth is concerned, figure 4.8a and 4.8b can be compared with figure 4.7.a and 4.7c, respectively. For 0.2 Hz case, deeper targets still preserves their visibility. However, for 1 Hz case, in deeper targets situation, artifact density has increased. Yet, targets are still recognizable.

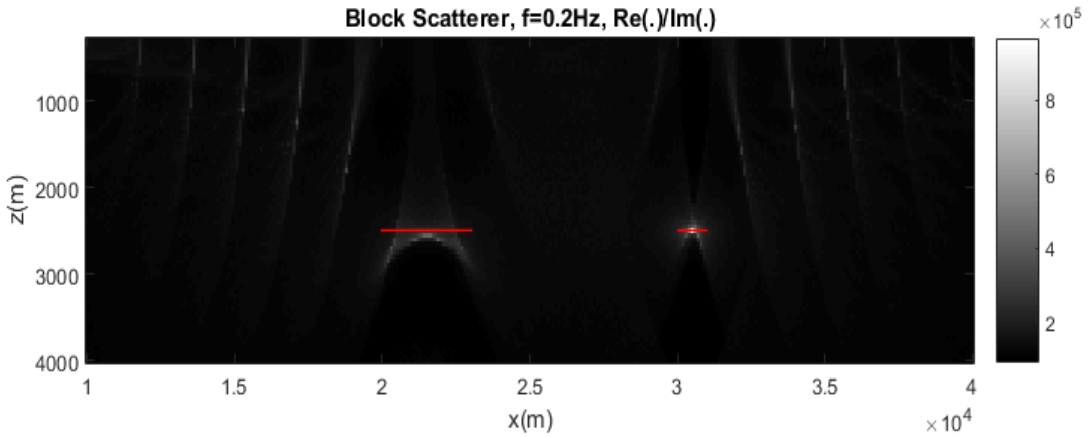

(a)

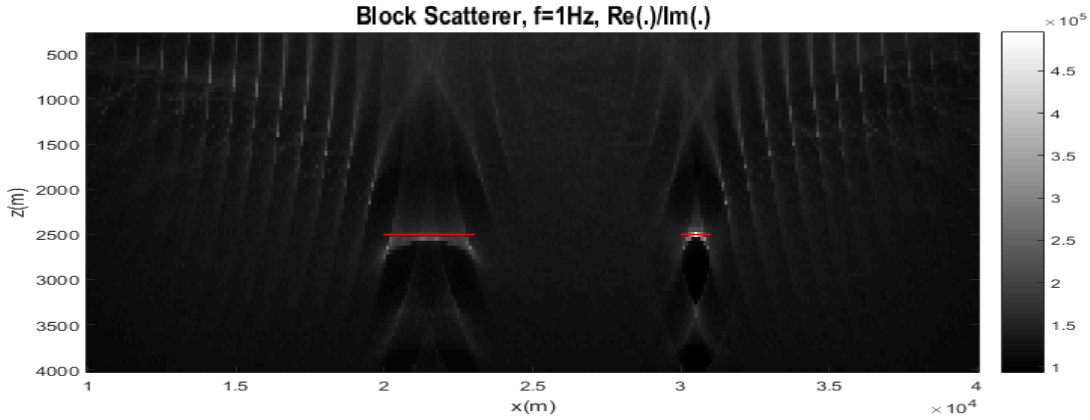

(b)

FIGURE 4.8: *Suggested IC (4.16) EM migration for deeper target versions of cases depicted in figure 4.7.a and 4.7.c, respectively for (a) and (b)*

Resolution is preserved, however, brightness of the targets degraded. Observably, both models related to depths 1000 and 2500m (both targets) indicates worse performance when probing frequency is 1 Hz. Indeed, in 1 Hz, there has been more background noise and unprecedently worse detection performance.

Up to now, perfect reflection (all the energy), noise free reception and only phase compensated cases are processed. Now models varying in reflection and noise will be studied. Considerig a phase compensation, two cases one of which employs a reflection coefficient of 0.3 and the other one 1, is compared in figure 4.9.a and b. Since the fields are only compensated for the phase, an amplitude factor is not detectable.

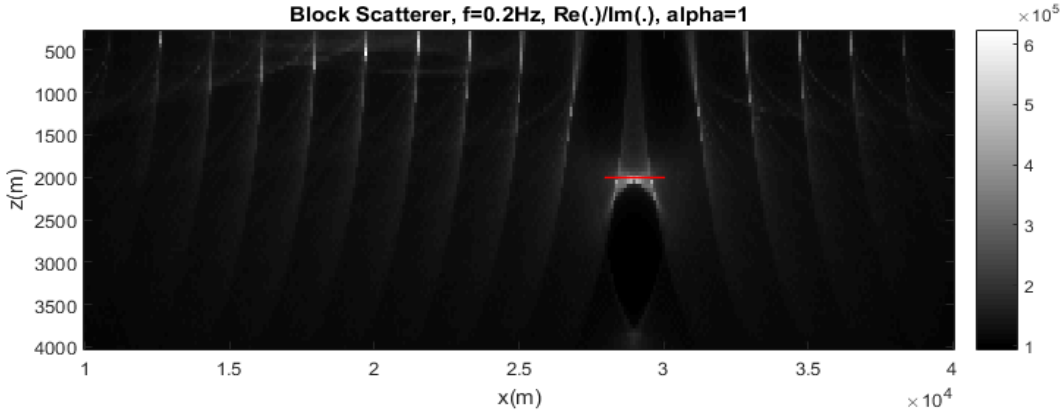

(a)

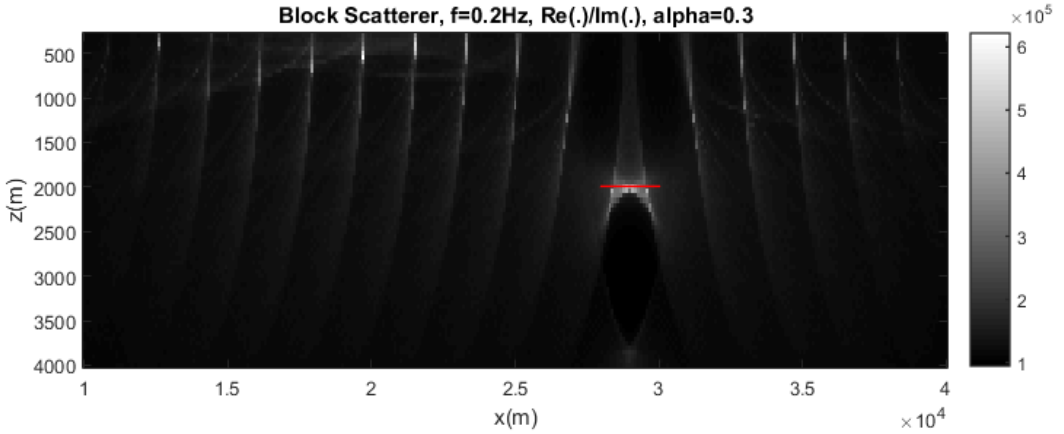

(b)

FIGURE 4.9: *Impact of reflectivity; (a) perfect reflection, (b) partial reflection*

In EM migration, received signal strength is in the order of 10^{-15} V/m. Hence, sensing an extra factor of 0.3, which actually corresponds very small resistivity difference (4.2 requires immense amplitude sensitivity and moreover, perfect amplitude compensation. Indeed, amplitude compensation is achievable only if perfect knowledge of extrapolators (Green's functions, E_r, E_s) are known. For a background resistivity model, this is done by analyticaly or numerically. However, determining the true background resistivity model is one of the greatest challenges in CSEM [3].

4.4 Effect of noise

Now, impact of additive white Gaussian noise will be included. Fig noise abcd represents the models designed for simulating the receiver SNR 100dB, 150dB, 200dB and infinite, respectively, for 0.2Hz probing frequency.

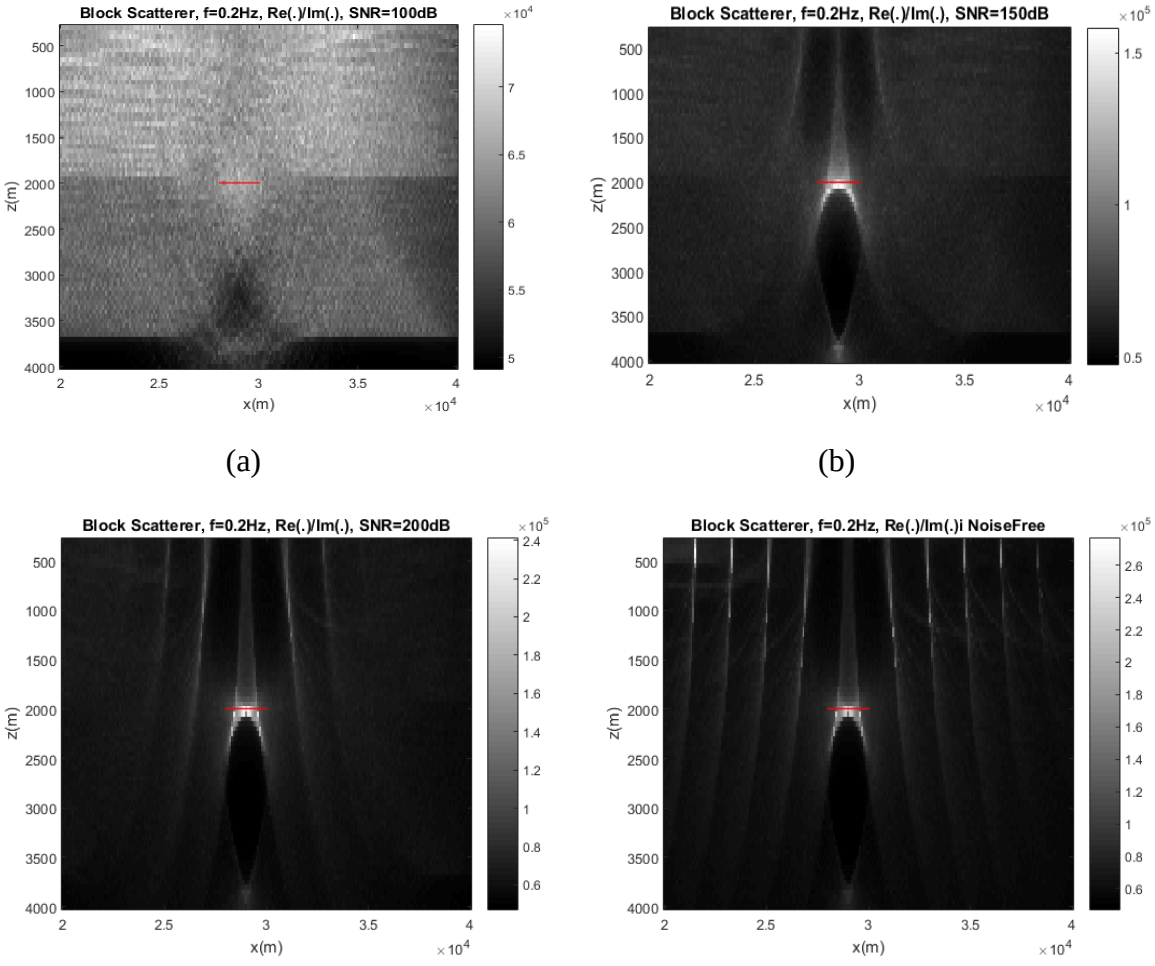

(a) (b)

(c) (d)

FIGURE 4.10: *For 0.2 Hz frequency, EM migration (4.16) applied to block scatterer case where targets are indicated with red lines and effect of noise included as; (a) SNR=100dB, (b) SNR=150dB, (c) SNR=200dB, (d) No noise*

For 100dB SNR data given in a, despite it is a really high value, target is still unrecognizable. However, in the plot related to results representing 150dB SNR case, in b, target is perfectly detectable, moreover, vertical distortions, which appeared in previous figures (4.7, 4.8, 4.9) seem to be weakened seriously. This is a very interesting consequence, which disturbingly suggests that some noise might improve the imaging performance in some cases.

Indeed, as SNR increases in c, vertical artifacts appear again as model gets closer to noiseless case, which is actually given in d.

As far as impact of frequency is concerned, figure 4.11.a and 4.11.b provides comparisonal potential with figure 4.10b, and 4.10.c, respectively, between of which, only frequency differs. It is clear that impact of frequency increase is negative in this high frequency case, which contradicts the general understanding of CSEM concepts. Another point must be remarked is that for high frequency, negative noise effects are stronger. In fact, SNR 150dB case for 1Hz promises almost nothing, while SNR 150dB case for 0.2 Hz promises almost perfect results.

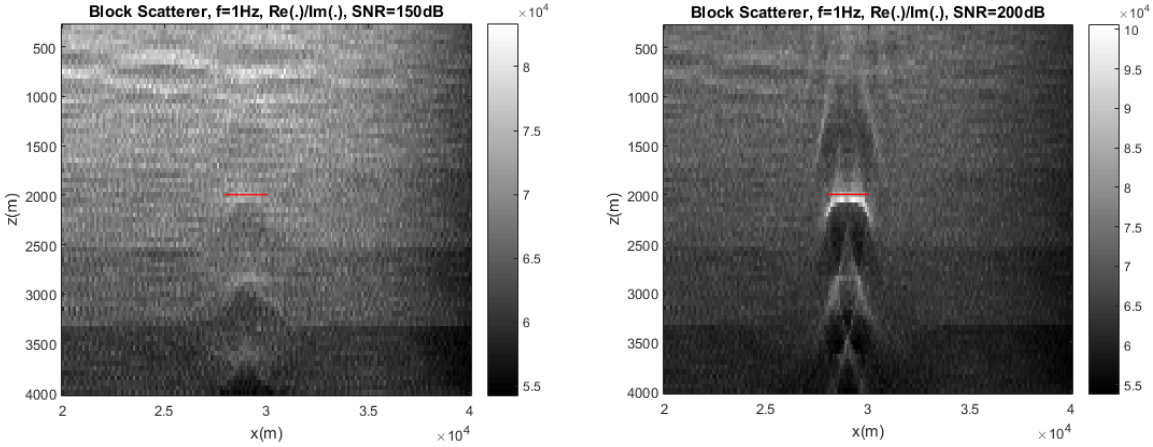

(a) (b)

FIGURE 4.11: *For 1 Hz frequency, EM migration (4.16) applied to block scatterer case where targets are indicated with red lines and effect of noise included as; (a) SNR=100dB, (b) SNR=150dB, (c) SNR=200dB, (d) No noise*

Since it has a potential to draw some attention, noisy case will be investigated further where SNR is chosen to be 150dB for 0.2Hz signal. Under mentioned conditions, impact of depth can be seen in figure 4.12. As noticed, there is no remarkable performance loss in this case. As far as introduced resolution definition is based on the most brightest point likelihood, actually, vertical resolution is so powerful that it is needed to draw the figures elongated through z axis, for targets to appear. Plots in figure 4.12 can also be compared to figure 4.10.b.

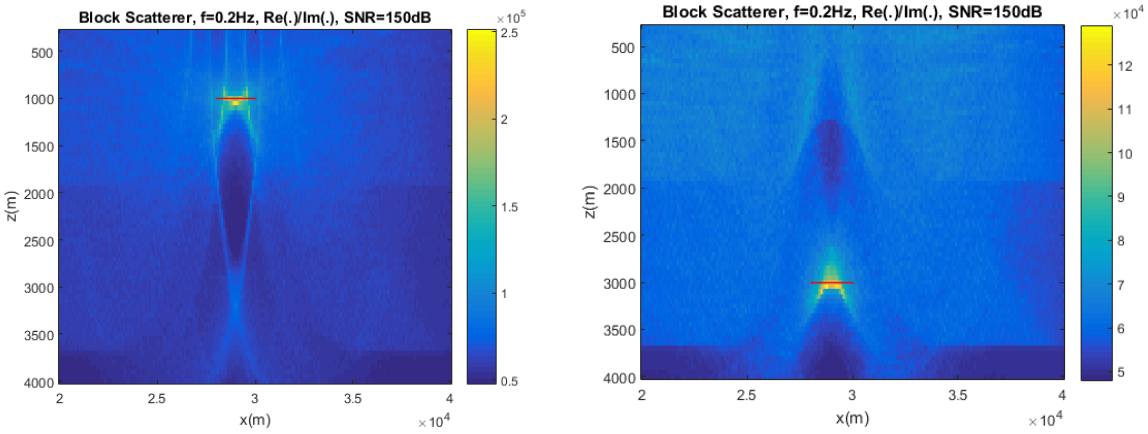

(a) (b)

FIGURE 4.12: *EM migration (4.16) applied for 150 dB SNR to block scatterer case where; (a) 100m, (b) 3000m deep targets are indicated with red lines*

Now for fixed frequency (0.2 Hz) and depth (2000m), a modification of target type will be given for noisy case where SNR is 150dB. In figure 4.14 vertical certainty of 200m is achieved and even shapes of targets are almost estimated. Notice that second type of target depicted in figure 4.14.b, exhibits a close representation of most common hydrocarbon traps in real life.

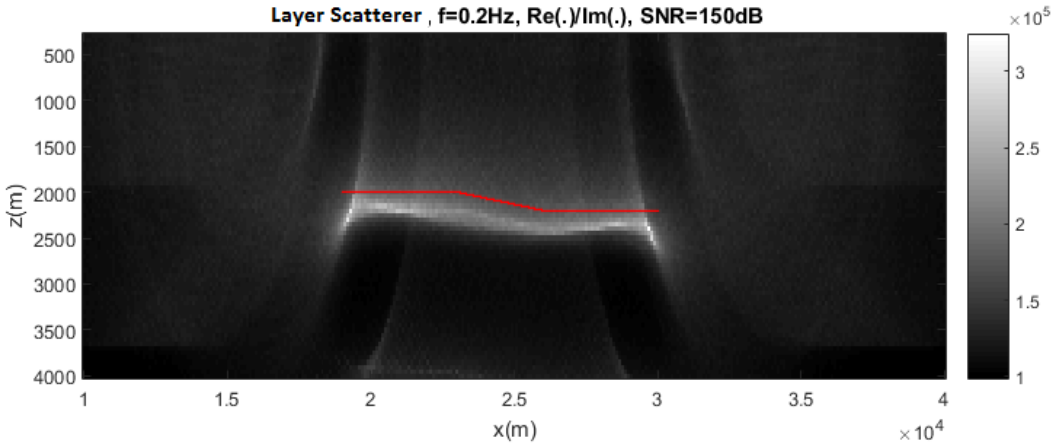

(a)

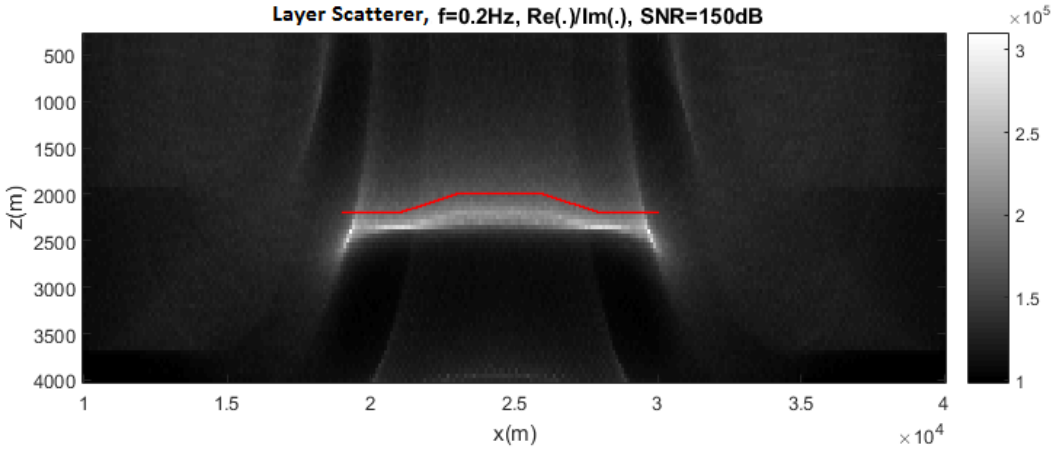

(b)

FIGURE 4.13: *EM migration (4.16) applied for 150 dB SNR to layer scatterer case where targets are indicated with red lines*

In order to provide a comparisonal basis, model represented in 4.13.b is processed by conventional algorithm (RE(.)), as well. Result is shown in figure 4.14.

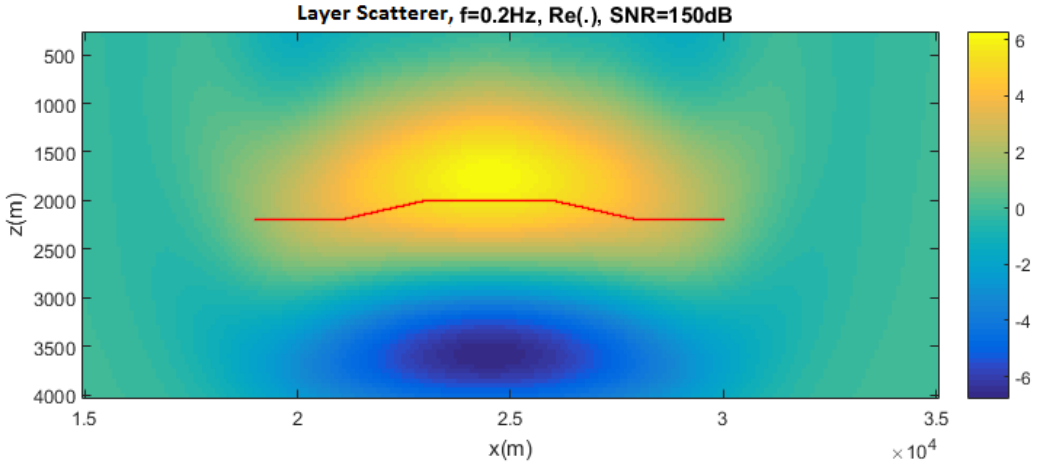

FIGURE 4.14: *Conventional EM migration application of very same case and target depicted and processed in figure 4.13.b*

As far as two block targets are considered again, however noisy case this time, it is clear that even though they are perfectly recognizable locally, they may not panoramically. Because of the simple fact that even they are migrated correctly, their peak contributions do not match, which leads one of them to appear much dimmed. Phenomenon was observed in figures 4.7, 4.8, also in 4.15 which depicts the situation in noisy case and is introduced now.

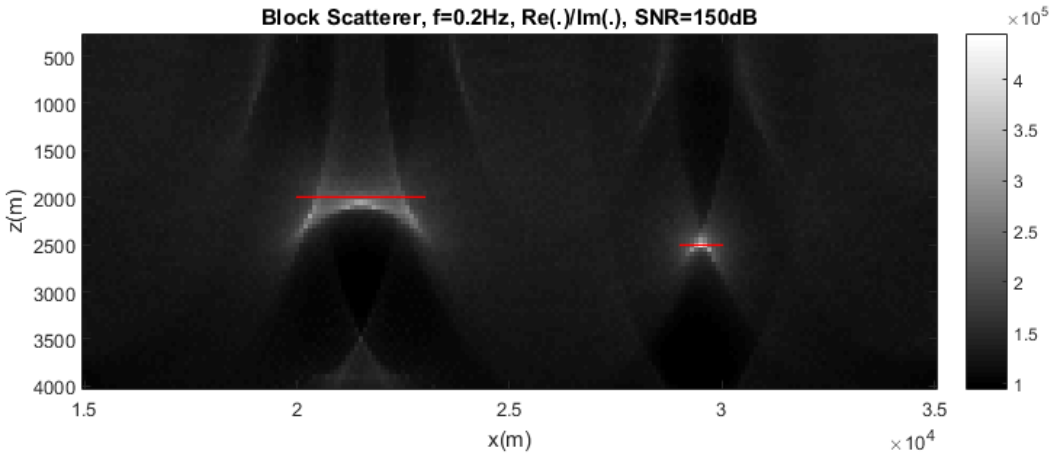

(a)

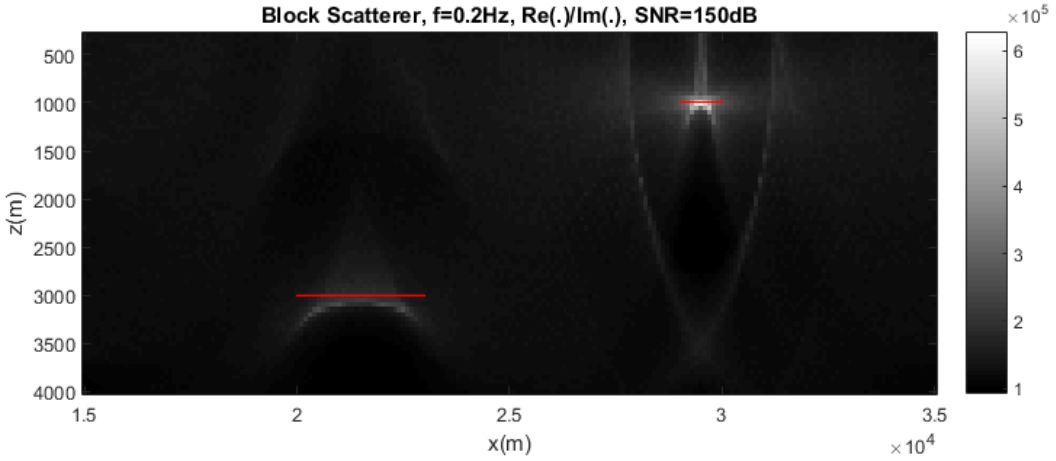

(b)

FIGURE 4.15: *EM migration (4.16) applied for 150 dB SNR to block scatterer case where targets moving in z direction are indicated with red lines*

In conclusion, newly introduced imaging condition (4.16), which in fact applies angular process, includes advantageous properties, however, it has challenging facts as well. The main advantage seems to be very accurate resolutions achieved, which sometimes allows even seeing the target's shape. On the other hand, since method requires amplitude filtering, some real point like targets may be missed. To overcome this, repeating imaging process for many filtering values (amplitude cut off), can be conducted. This way, all potential targets would be seen. On the other hand, it is observed that method sometimes introduces vertical artifact patterns for noiseless cases. This effect is reduced with added noise. On the other hand, any perturbing occurances that are tought to be artifically reasoned due to their periodic disturbance, can be degraded by a horizontal low pass filtering. Moreover, resulting images are highly recommended to be reviewed for various non-linear amplitude filters (interactive color map). Example results are given in figure 4.16.

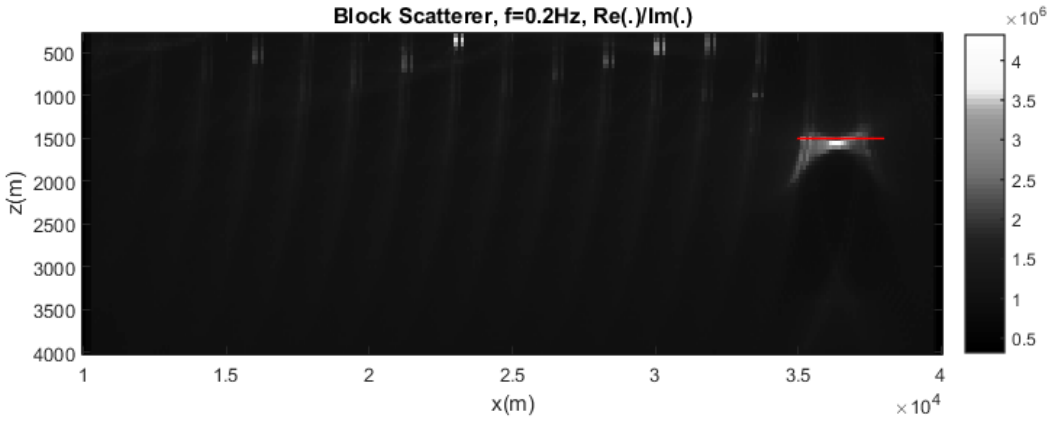

(a)

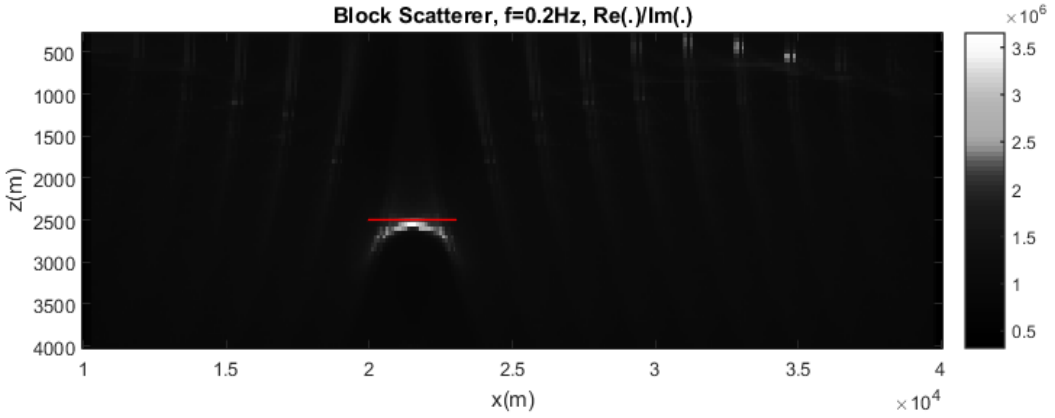

(b)

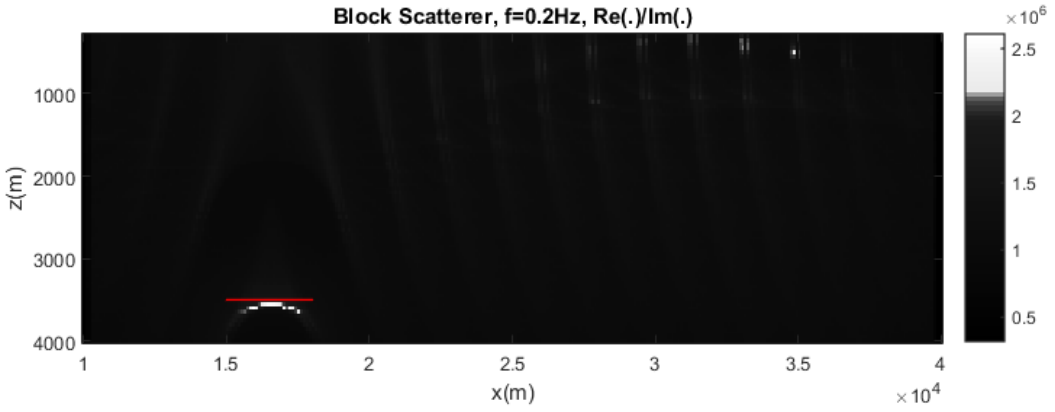

(c)

FIGURE 4.16: *EM migration: Re(.) / Im(.), non-linear amplitude filtering and horizontal low pass filtering applied in noiseless case for various target depths*

Chapter 5

Applications to real dataset

5.1 Model introduction

In previos chapters, intrinsic behaviours of CSEM data (chapter 3) and migration (chapter 4) as an imaging method are studied with the help of simulated data. However, this chapter aims applying earlier mentioned approaches to a real dataset acquired in Faer Øer field. In this chapter, data related to the model given in figure 5.1 will be considered. In this model, data is gathered by 919 sources and 28 receivers distributed along approximately 170 km inline distance as given in figure 5.1. On the other hand, background fields are numerically computed for each source and receiver pair and for each point belongs to subsequently mentioned migration domain.

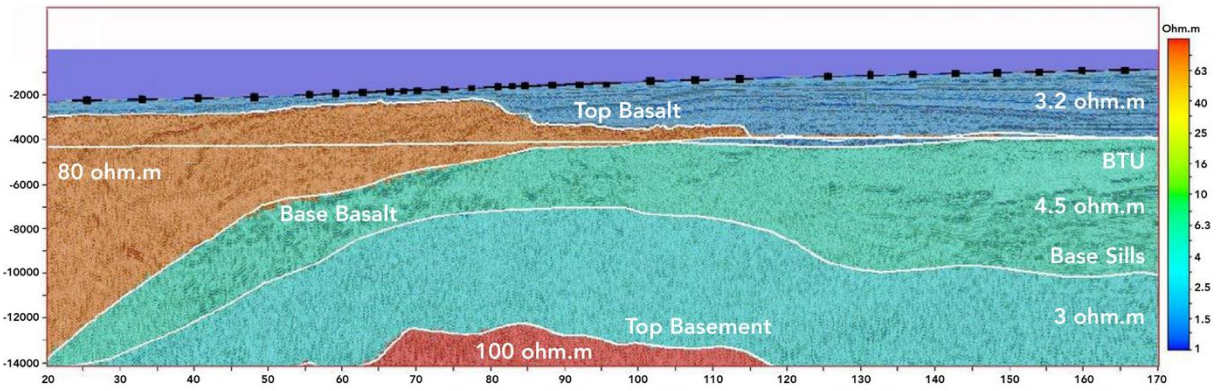

FIGURE 5.1: *Faer Øer field cross section and parameters with receivers shown as black markers*

Experiment is held by a frequency range of 0.125, 0.25, 0.375, 0.5, 0.625, 0.75 Hz.

5.2 MVO and PVO

Mentioned model, has large basalt layer as resistor and expected anomalies would be derived from this structure. Indeed, figure 5.2 states that as far as logarithmic received field

amplitude is concerned with respect to source-receiver positions domain, a large anomaly seems to be present till 80th km, as can be seen in figure 5.2.a and 5.2.b where both harmonics given. In this interval, clearly, for one shot released from one source located around 70th km, neighbouring recivers measure larger amplitudes with respect to other receivers close to another shot which is related to one source located, for instance, in 140th km. This basically means that there is anomaly underlying around early offsets (seemingly between 40-90km). However, this observation is a comparison without considering backgroud data. On the other hand, notice that for higher frequency (0.75 Hz), any shot fades stronger than the low frequecy equivalent.

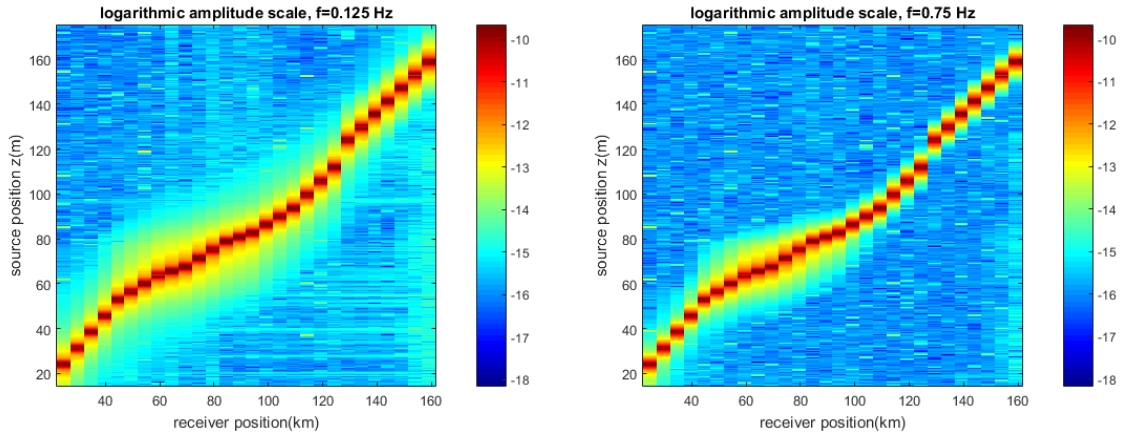

(a) (b)

FIGURE 5.2: *Faer Øer field logarithmic observed data amplitude behaviour with respect to source and receiver positions, for (a) 0.125 Hz and (b) 0.75 Hz frequency*

For a more solid evaluation of the data, as conducted in chapter 3, also background data must be considered. In figure 5.3.a and b, magnitude versus offset behaviours extracted for frequencies 0.125 Hz and 0.75 Hz respectively, for sources located at 70km and 140km in both graphs. As already observed from figure 5.2, shot around 140th km promises no significant anomaly, whereas its equivalent for 70 km exhibits large deviations between observed and background data for both frequencies. Figure 5.3 obviously indicates anomaly presence around 70th km, for both harmonics. Also notice that for higher frequency case, MVO behaviours fade more rapidly, as expected. In both sub-figures, values smaller than noise level is cut.

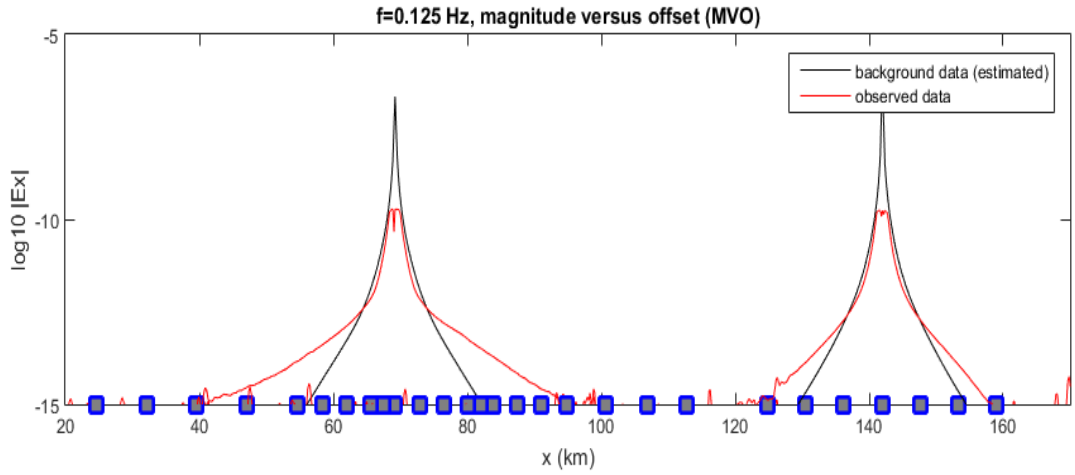

(a)

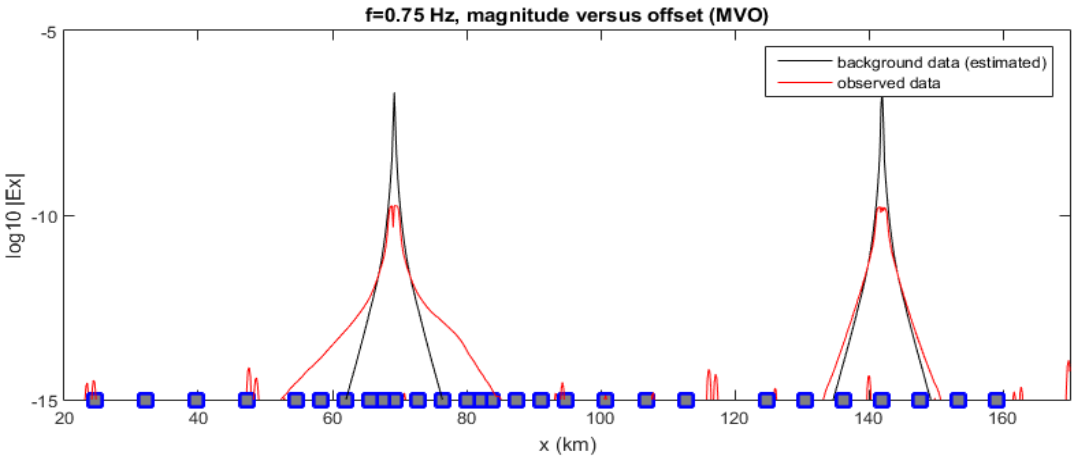

(b)

FIGURE 5.3: *Faer Øer field logarithmic magnitude versus offset (MVO) behaviour for; (a) 0.125 Hz and (b) 0.75 Hz frequencies on receivers located 70th and 140th km*

5.3 Migration

In previous chapter, intrinsic behaviours of migration was focused on as far as simulated (artificial) data was concerned. However, this chapter is devoted to understanding actual responses of migration to a real dataset, as an imaging technique.

Acquired data is interpreted for 2 overlapping migration domains as indicated in figure 5.4.a and b respectively

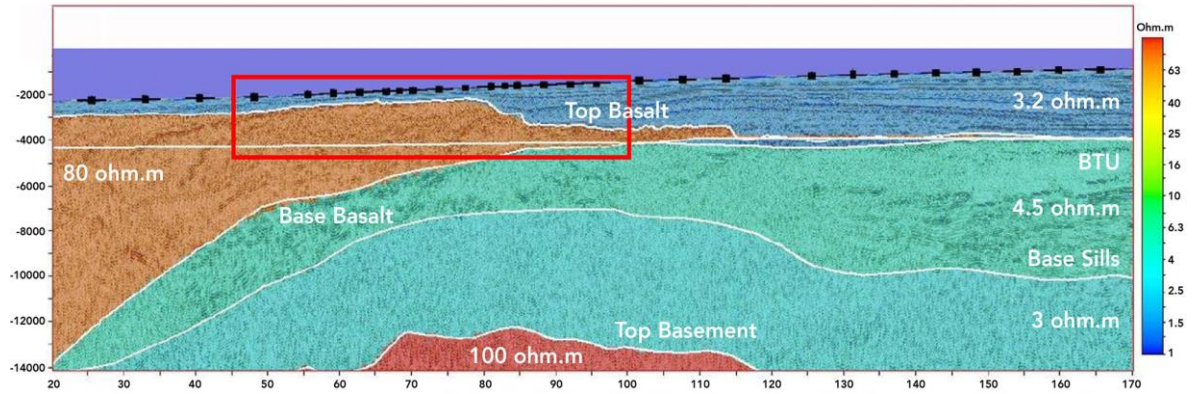

(a)

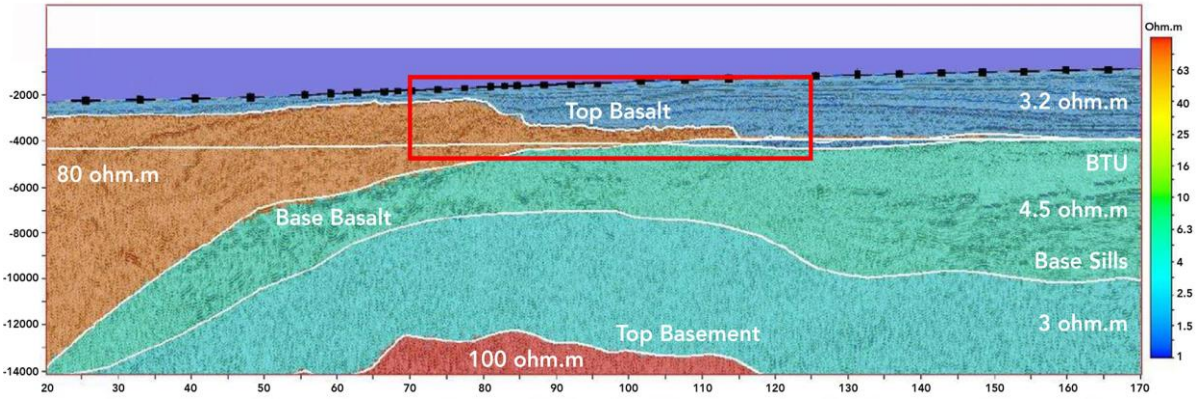

(b)

FIGURE 5.4: *Cross section of experiment field with migration domains for (a) portion I and (b) portion II indicated by red rectangulars*

When conventional imaging condition, where real part of migrated field is concerned (4.12), resulting images would look like ones given in figures 5.4 and 5.5 for all harmonics used. Here, notice that as frequency increases, resolution also increases. On the other hand, it is clear that basalt interface fits the transition region between positive and negative valued resulting migrated fields perfectly for both domains. Another point to note is that, expectedly, basalt structure (which is thought to exist) after 85th km is barely visible. This is either its relatively low transverse resistance or greater depth.

As far as combination of two migration domain results are concerned in a single plot for summation over all harmonics, figure 5.7 provides resulting image where existance of anomaly is clear and it follows the interface trend of interface. However, it concentrates between 60-85th km, because resistive anomaly is thought to be closer to the ocean floor around these distances. Moreover, basicly as can also be noticed from figure 5.3, receiver density is higher between 60-85th km. In this conventional migration scheme, it is also noticed that anomalous images does not provide satisfying qualitative results as far as locating certainty is concerned and in figure 5.7, resolution is seen to be around 500m.

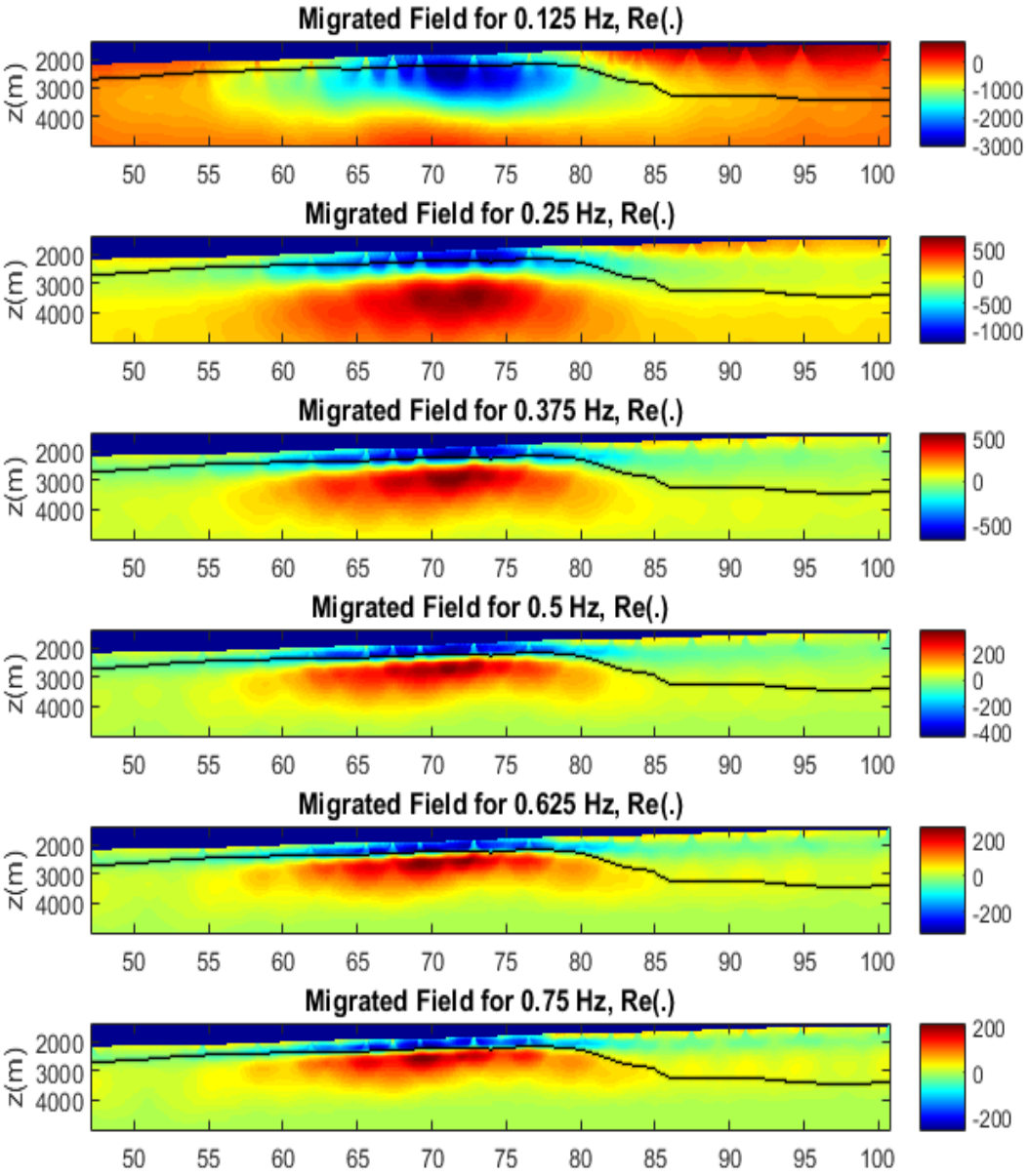

FIGURE 5.5: *Migrated field for all frequencies on portion I for conventional IC: Re(.) (4.12)*

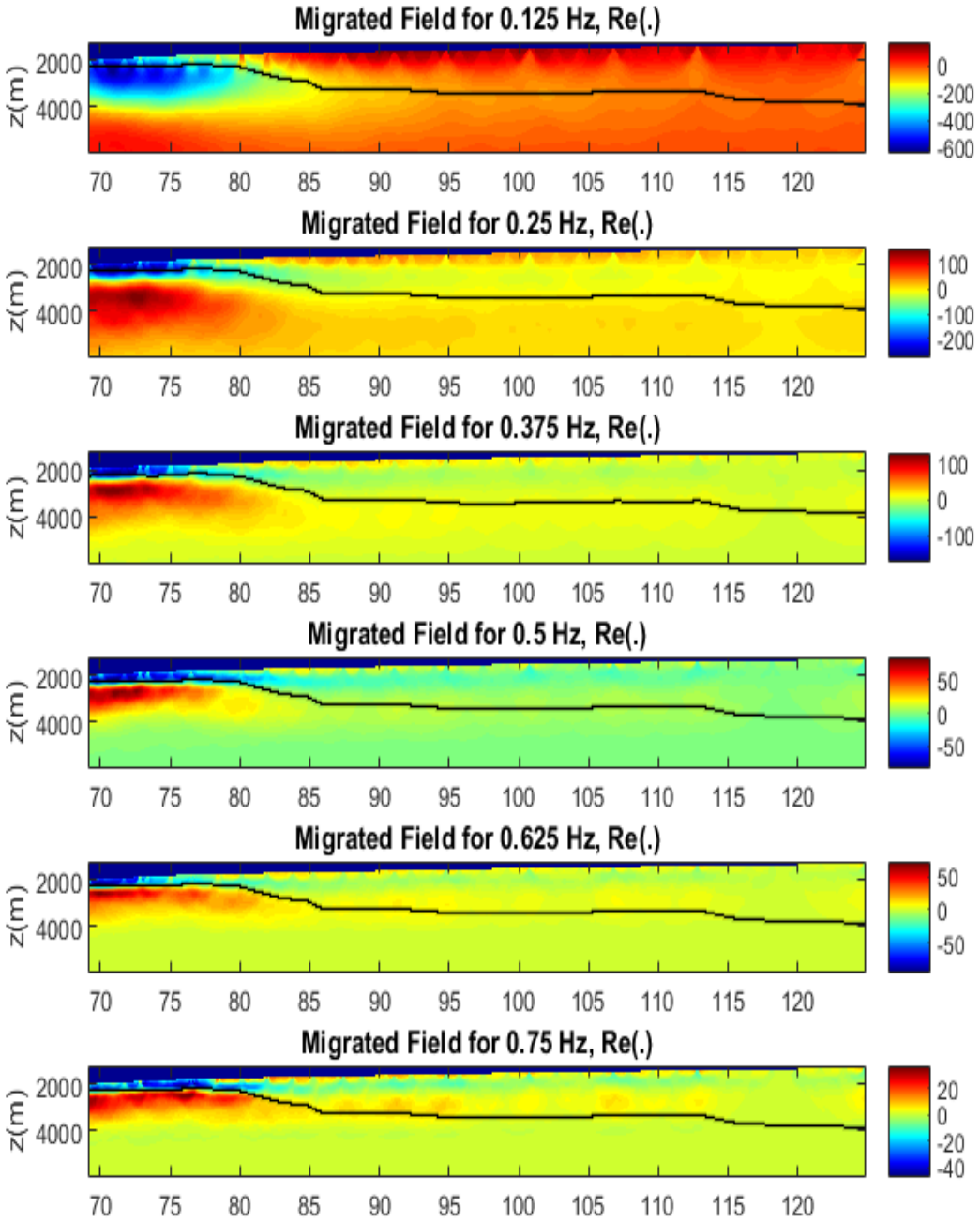

FIGURE 5.6: *Migrated field for all frequencies on portion II for conventional IC: Re(.) (4.12)*

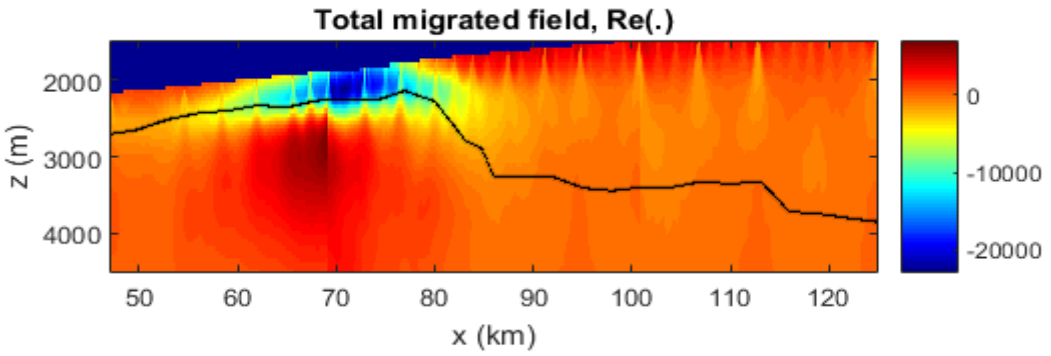

FIGURE 5.7: Total m*igrated field sum over all harmonics and unified portions for conventional IC: Re(.)*

Now i consider suggested imaging condition into the migration concept. As far as (4.16) is implemented, response for first 3 frequencies are given in figure 5.8. It is seen that particularly for frequencies 0.25 Hz and 0.375 Hz, interface is followed by anomalous image region with small deviations. However, as higher frequencies are concerned, impact is event greater.

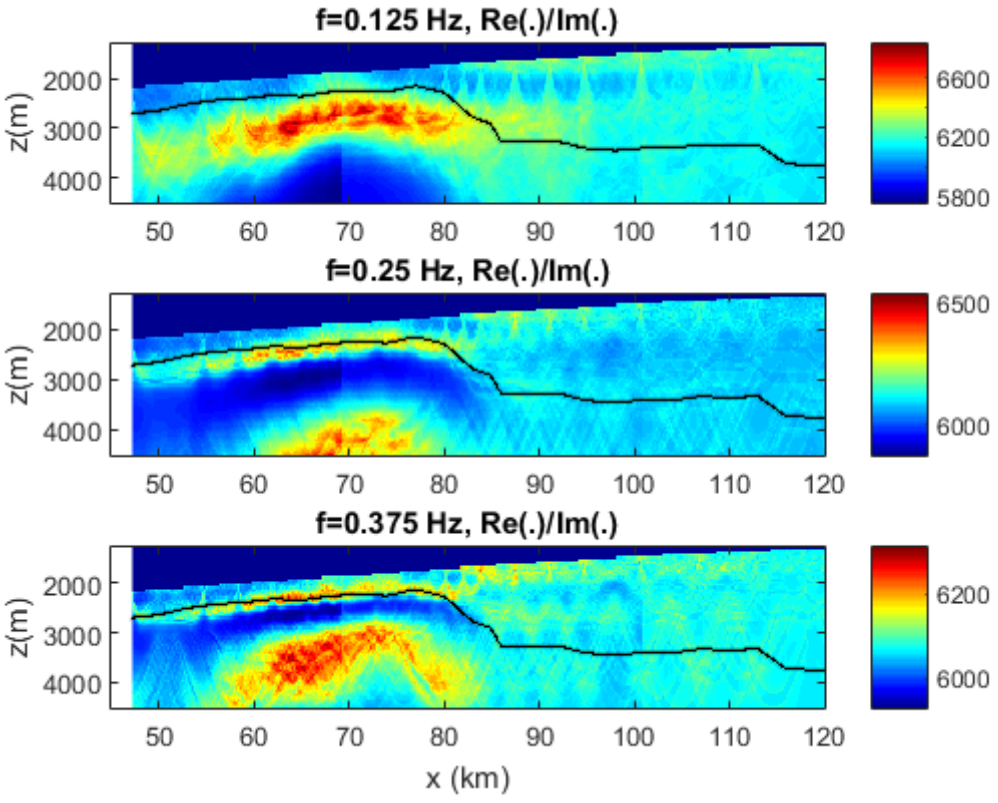

FIGURE 5.8: *Migrated results for unified domains (portion I & portion II) for new IC (4.16)*

For higher frequencies (0.5Hz, 0.625Hz, 0.75Hz), high resolution around 150m is gathered, indeed, therefore it's been a necessity to organize the plots in greater z direction scale to provide a better appearance of the anomaly as indicated in figure 5.9

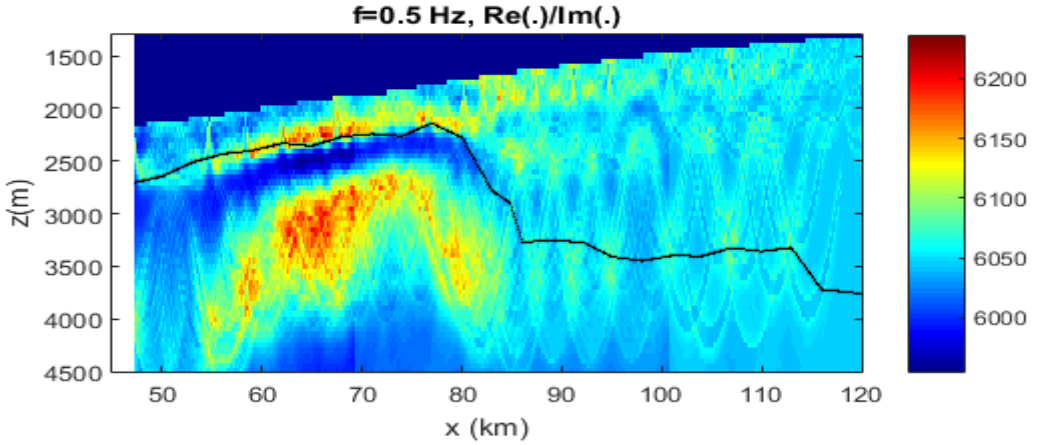

(a)

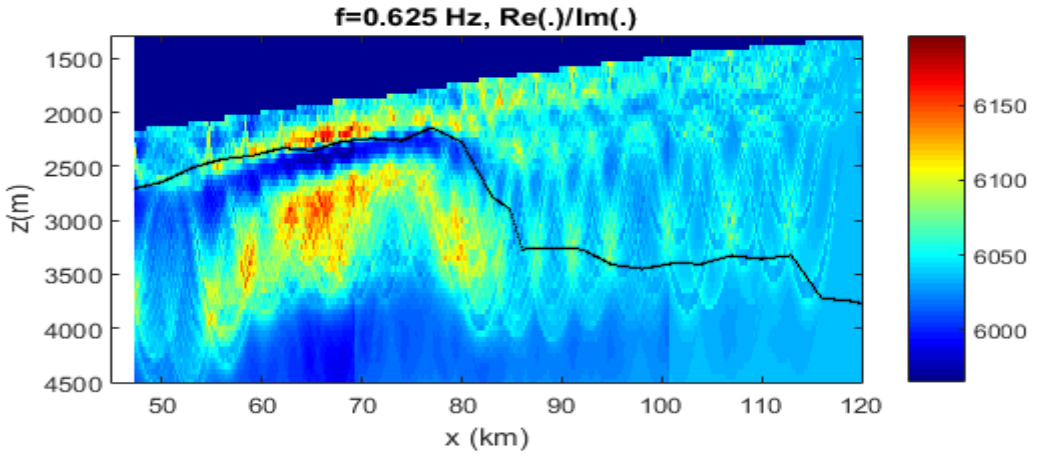

(b)

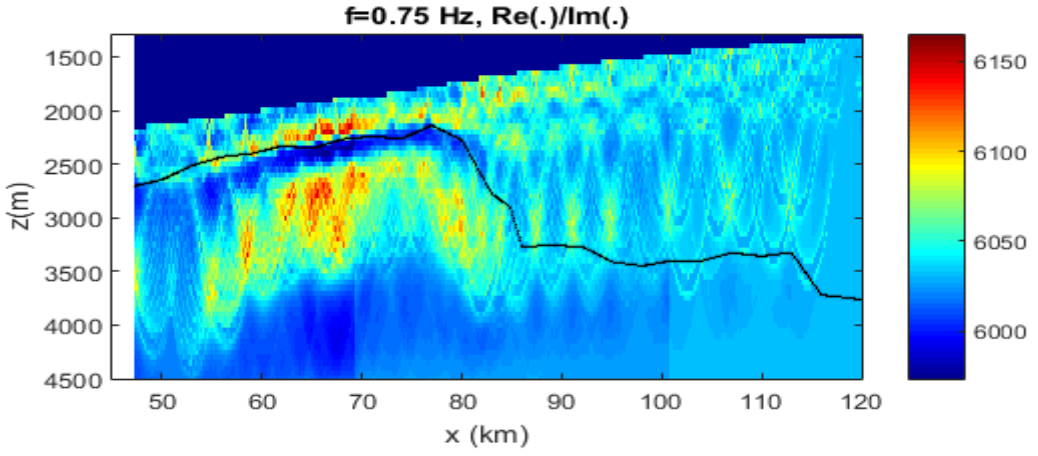

(c)

FIGURE 5.9: Total m*igrated field sum over all harmonics and unified portions for conventional IC: Re(.)*

It is clear that when (4.16) is implemented, anomalous region appeared as a result of migration, follows the basalt interface with a small uncertainty (150m) between 55-85th km where the real anomaly is thought to be closest to the ocean floor.

Bibliography

[1] D. V. Shantsev, F. Roth, C. Twarz, A. Frisvoll, A. K. Nguyen, *Shallow water CSEM using a Surface-towed Source*, EAGE (June 2010)

[2] S. Constable, *Mapping shallow geological structure with towed marine CSEM receivers*, SEG (2012)

[3] L. MacGregor and J. Tomlinson, *Marine controlled-source electromagnetic methods in the hydrocarbon industry: A tutorial on method and practice*, Interpretation, Vol. 2, No. 3 (August 2014)

[4] E. S. Um and D. L. Alumbaugh, *On the physics of the marine controlled-source electromagnetic method*, GEOPHYSICS, Vol. 72, No. 2 (March-April 2007)

[5] S. Constable, *Ten years of marine CSEM for hydrocarbon exploration*, GEOPHSICS, Vol. 75, No. 5 (September-October 2010)

[6] M. S. Zhdanov, *Electromagnetic geophysics: Note from the past and the road ahead*, GEOPHYSICS Vol.75, No.5 (September-October 2010)

[7] Schlumberger web site, *Oilfield Rewiev, Spring 2009.* Online at http://www.slb.com/resources/oilfield_review/en/2009/or2009_spr.aspx

[8] PGS website, https://www.pgs.com/marine-acquisition/services/towed-streamer-em/

[9] J. Yuan and R. N. Edwards, *The assessment of marine gas hydrates through electrical remote sounding:* Hydrate *without a BSR ?*, GEOPHYSICAL RESEARCH LETTERS, Vol.27, No.16, (August 2000)

[10] R. Mittet, Frank Maaø, Odd M. Aakervik and Svein Ellingsrud, *A two-step approach to depth migration of low frequency electromagnetic data*, SEG (November 2005)

[11] D. Peace, D. Meaux, M. Johnson, A. Taylor, *Controlled Source Electro-Magnetics for hydrocarbon Exploration*, HGS Bulletin (November 2004)

[12] G. P. Hersir, K Árnason, *Resistivity of Rocks* (November 2010)

[13] N. Yahya, N. Nasir, M. N. Akhtar, M. Kashif, T. Hussain, H. M. Zaid, A. Shafie, *Electromagnetic Response Studies of the Antenna for deep Water Deep Target CSEM Environment*, JEMAA (December 2012)

[14] A. A. Valenciano, B. Biondi, *2-D deconvolution imaging condition for shot-profile migration*, Online at: http://sepwww.stanford.edu/data/media/public/oldsep/oldsep/valencia/Research/SEP/SEG2003/seg2003.pdf

[15] A. Gola, *Physical aspects of marine Controlled Source Electromagnetic Method Data Processing and Imaging*, Politecnico di Milano, Department of Electronics, Information and Bioengineering, February 2016.

[16] L. O. Løseth, *Modelling of Controlled Source Electromagnetic Data*, PhD thesis, Norwegian University of Science and Technology, Department of Pyhsics, March 2007.

[17] E.C. Morris, *Fast imaging techniques of MCSEM data*, PhD thesis, University of Southampton, Facult of Engineering, Science and Mathematics – Shool of Ocean and Earth Sciences, February 2008.

[18] R. R. Syms and J. R. Cozens, *Optical Guided waves and Devices*, June 1992

[19] J. F. Clearbout, *Imaging the Earth's interior*, January 31 1996

[20] S. J. Orfanidis, *Electromagnetic Waves and Antennas*, November 2004

[21] M. N. Nabighian, *Electromagnetic Methods in Applied Geophysics*, volume 2, application, parts A and B, 1988. ISBN 15608008224, 9781560800224.

[22] http://www.wikipedia.org/

[23] http://www.digitalearthlab.com/

[24] Acquisition report included in the Faer Øer dataset.

[25] M. S. Zhdanov, P. Traynin, J. R. Booker, *Underground imaging by frequency-domain electromagnetic migration*, GEOPHYSICS, Vol. 61, No.3 (May-June 1996)

[26] K. Hokstad and T. Røsten, *On the relationships between depth migration of controlled-source electromagnetic and seismic data*, March 2007

[27] J. Mattson, P. Lindqvist, R. Juhasz and E. Bjornemo, *Noise reduction and error analysis for towed EM system*, SEG (September 2012)

[28] T. Holten, E. G. Flekkoy, B. Singer, E. M. Blixt, A. Hanssen, K. J. Maloy, *Vertical source, vertical receiver electromagnetic technique for offshore hydrocarbon exploration* (2009)

[29] E. Onajite, *Seismic Data Analysis Techniques in Hydrocarbon Exploration, 1st Edition*, November 2013

[30] http://www.geotech.org/

[31] J. M. Reynolds, *An ıntroduction to Applied and Environmental Geophysics*, *2nd Edition*, April 2011

[32] D. Gubbins, E. Herrero-Bervera, *Encyclopedia of Geomagnetism and Paleomagnetism*, 2007

[33] R. N. Edwards, H. Lee, M. N. Nabighian, *On the theory of magnetometric resistivity (MMR) method*. GEOPHYSICS 1978

[34] R. N. Edwards, L. K. Law, M. DeLaurier, *On measuring the Electrical-Conductivity of the Oceanic-Crust by a Modified Magnetometric Resistivity Method*, JGR, 1981

[35] K. Vozoff, *Magnetotellurics: Basic Theoretical Concepts*, 1972

[36] www.eoas.ubc.ca

[37] L. MacGregor and M. *Sinha, Use of marine controlled-souce electromagnetic sounding for sub-basalt exploration*, GEOPHYSICAL PROSPECTING, 2000

[38] R. Mittet, *Normalized amplitude ratios for frequency-domain CSEM in very shallow water*, November 2008

[39] C. Ramananjaona, L. MacGregor, D. Andreis, *Inversion of marine electromagnetic data in a uniaxial anisotropic strafied earth*, GEOPHYSICAL PROSPECTING, 2011

[40] S. H. Gray, *Speed and accuracy of seismic migration methods*

[41] I. F. Jones, *Tutorial: migration imaging conditions*, December 2014